Master thesis

Dynamic Contactless Power Transfer On Go-karts

Vincent de Leeuw - 4114671
Department of Mechanical Engineering
Delft University of Technology

[http://www.crgrentalkart.com]

TUDelft

Acronyms

AC Alternating Current. 7, 20, 41, 69

BEV Battery Electric Vehicle. vii, 70–72, 75–78

BMS Battery Management System. 33

DC Direct Current. 20, 33

EMF Electromagnetic Field. iii, 3, 21, 28, 33, 52–55, 57–63, 69, 75, 78

EV Electric Vehicle. vii, 33

FEM Finite Element Method. 21, 23, 30, 33, 41, 45, 51, 52

ICE Internal Combustion Engine. vi, vii, 2, 3, 64, 72, 75–77

ICNIRP International Commission on Non-Ionizing Radiation Protection. 20, 21, 30, 37, 52, 53, 57, 60–63, 78

IM Induction Motor. 33

IPTS Induction Power Transfer System. iii, iv, vi, vii, 2–9, 17, 20, 23–25, 27, 29–32, 34, 38, 39, 45, 51, 52, 63, 64, 66, 68–73, 75–78

MEEDC Mountain Energy Expensive Driving Cycle. vii

PLD Power Loss Detection. 21

PM Permanent Magnet. 33

PWM Pulse Width Modulation. 19, 20

RM Reluctance Motor. 33

SBM Synchronous Brushed Motor. 33

SOC State of Charge. vii, 33, 51, 64, 67, 68, 70, 71

TAT Turn Around Time. 2

Contents

Acknowledgements

Before starting, I wish to express my gratitude to the people who made this feasibility study possible. As I am an mechanical engineering student at 3ME who needed counseling from EWI, there were some obstacles before I could start. This didn't make the process any easier, but I am glad that it all worked out. The required extra courses, needed for this arrangement, helped me to develop the knowledge required to complete this study and were very valuable.

First of all, I wish to express my deepest gratitude to Dr. Jianning Dong, who was the first to believe in the added value of this study. He has taken the time -and risk- of supervising a student from another faculty, that had a knowledge gap about parts of the subject. Among other things, he has helped me to zoom out and see the bigger picture on many occasions. His guidance in this process was essential and very much appreciated, for which I want to thank him very much.

Furthermore, I would like to thank Harm Schuurman from Barnman Holding B.V. for enabling me to conduct this research for his company. Harm and I met through a friend and came up with the research assignment together. Even-though it took quite a while before I could get started, he remained supportive and hopeful. I very much enjoyed the meetings that we had; that were suppose to be only about the research, but usually ended up in debates and stories. Many thanks for this opportunity and the stories along the way.

I would also like to thank Dr.ir. Riender Happee and Prof.dr.ir. Pavol Bauer for the opportunity to conduct my research at EWI. The construction was nothing like the standard, but I believe the result was worth the extra effort required.

Thank you all very much!

Introduction

Wireless power transfer is getting more attention than ever before. Most high-line mobile devices are standard equipped with a receiver for wireless charging. Furniture makers are implementing transmitters in their furniture, resulting in less wires across tables and cabinets. Furthermore, the car industry is making head way in this department. Besides having wireless charger options for phones inside vehicles, wireless charging pads for the vehicles battery-pack itself are being developed and sold commercially.

Even though this technique is becoming more common in a variety of fields, it seems to be lagging in the go-kart industry. As more manufacturers seem to be designing electric powered go-karts, there still are no proper solutions for most of the major drawbacks. All electric karts are currently composed out of the same components; these are shown in Figure 1.
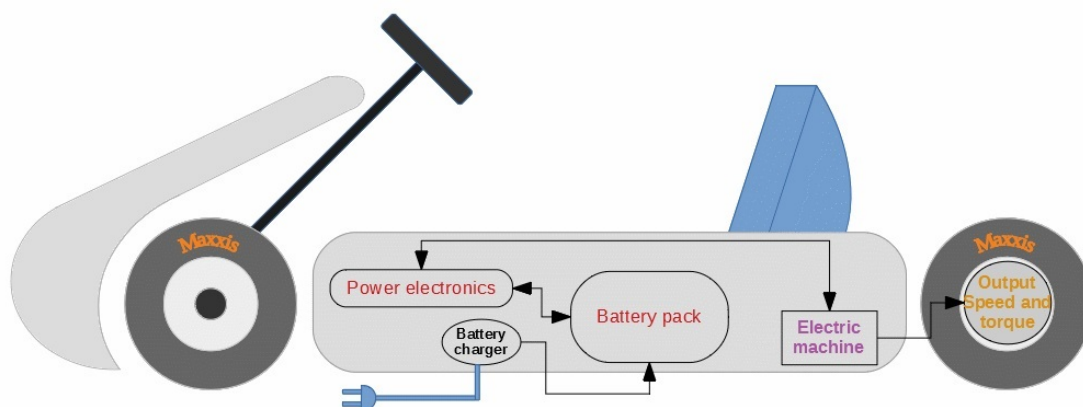
Figure 1: Current setup of an electric go-kart.

The added weight from the battery-pack, combined with the required amount of time for charging, are tremendous drawbacks. This is especially true in the rental industry where continues drive-ability is required to ensure that profit is maximized. This is one of the reasons why electric go-karts are having a hard time taking over the rental industry.

Charging battery-packs takes a long time, which means that either double the number of battery-packs or go-karts is required. This introduces a huge economical drawback to using the electric option, as electric go-karts are expensive and swapping of battery-packs requires charging stations and extra labour costs due to the required swapping of batteries. The Internal Combustion Engine (ICE) is still the preferred option for most tracks, as it is cheaper and can be refuelled within minutes.

The downsides to using an ICE are discussed in a wide variety of platforms in recent years. However, the most important downside to using an ICE on go-karts is pollution. An Induction Power Transfer System (IPTS) could assist an electrical go-kart in such a way that its main drawbacks -the added weight and charging time- are greatly reduced or even eliminated. These qualities would make an electric go-kart a better option and could even drive the ICE out of the industry. A comparison of different aspects of the techniques is shown in Table 1.

Table 1: Comparison of power sources.

Power source	ICE	BEV	IPTS
Required refilling time	2 minutes[1]	30 minutes[2]/2 minutes(swap)[3]	5 minutes[4]
Dual capacity requirement	no	yes	no
Maintenance	low	very low	very low
Continues driving	yes	only on multiple capacity	yes
Weight of engine	25 kg	12 kg	12 kg
Weight of charger	0 kg	0 kg	unknown
Weight of battery	2 kg	43 kg	unknown

There are some conductive solutions to this problem that are able to charge the batteries of the go-kart quickly. In these systems the go-karts are guided over a conducting rail in the pit-lane, with which the go-karts make contact trough wipers underneath the bottom. However, these are subjected to a lot of wear and must be properly shielded as they can be dangerous. This also still doesn't reduce the required battery-pack size and thus the weight of the go-kart, as the go-kart can only be charged during standstill.

Wireless power transfer could be done either statically; where both coils do not move in reference to each-other, or dynamically; where the primary coil is at a fixed point on the ground and the secondary coil is travelling over this primary coil. The charging of the battery in go-karts with an IPTS will be done statically in the pit-lane, but also dynamically on the track. Both of which are shown to extend the range of an Electric Vehicle (EV), if properly sized. Figure 2, shows how a 30kW IPTS system would influence the State of Charge (SOC) of an EV when added to a Mountain Energy Expensive Driving Cycle (MEEDC). It clearly shows that such a system could reduce the battery size of an EV.
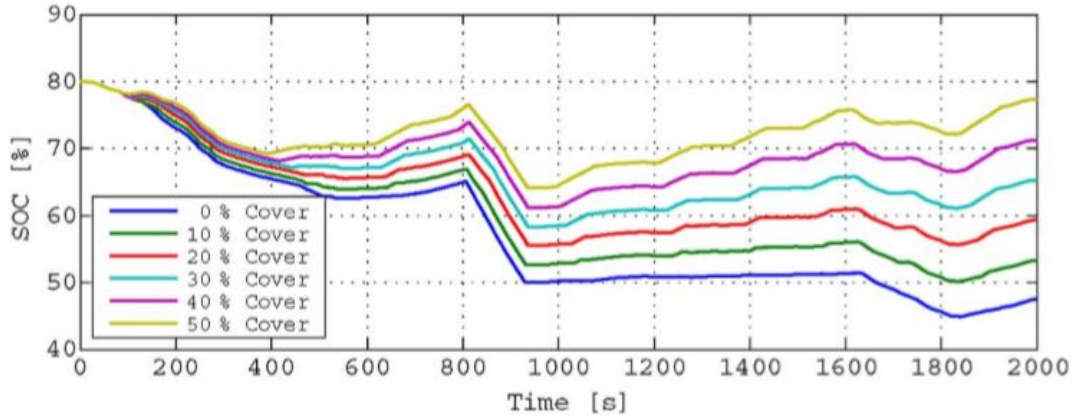
Figure 2: 30 kW charger in MEEDC with transmitters installed in various percentages of road-surface [1].

The goal of this study was to determine the feasibility of an IPTS on a go-kart. First, the required setup for this study was determined through literature study, in which performance and simplicity were key factors. Second, optimization of the coil parameters was preformed using COMSOL and Matlab. Third, a safety analysis of the design was done using COMSOL and required safety precautions were determined. Finally, we investigated if the final design can be used on a go-kart to reduce the required battery-pack size, by modelling the entire system in Simulink. This simulation also provided the information that was required to evaluated if this system represent a financially viable option and how the weight of the go-kart is effected by the IPTS.

---

[1]Estimate based on 5.3L petrol tank
[2]Assumed C/2 charging
[3]Estimate based on removing a single cover for quick swapping
[4]Time set by researcher

Chapter 1

Component selection for feasibility testing of go-kart ipts

1.1   Introduction

The component selection in both static and dynamical charging is crucial to the performance. Figure 1.1 shows the important aspects for both static and dynamic charging; it also shows that there are many similarities between them. In this chapter we will provide some background information on wireless charging, to help define the requirements for such a system. These requirements, combined with the current state of art, will be used to select the most suitable system setup. For several important components a comparison will be made, to help understand why these components were chosen.

The need for both static and dynamic charging required literature study on both topics. The main difference between the static and the dynamic charging is that the coupling factor in dynamic charging changes over time, whereas it remains constant in stationary charging. This makes it harder to keep transferring power as the capability to do so is influenced by this coupling factor, which will be explained in Chapter 2. On a component level, the difference between these charging methods lies in the transmitter, as this should be designed for charging with almost constant varying misalignment.
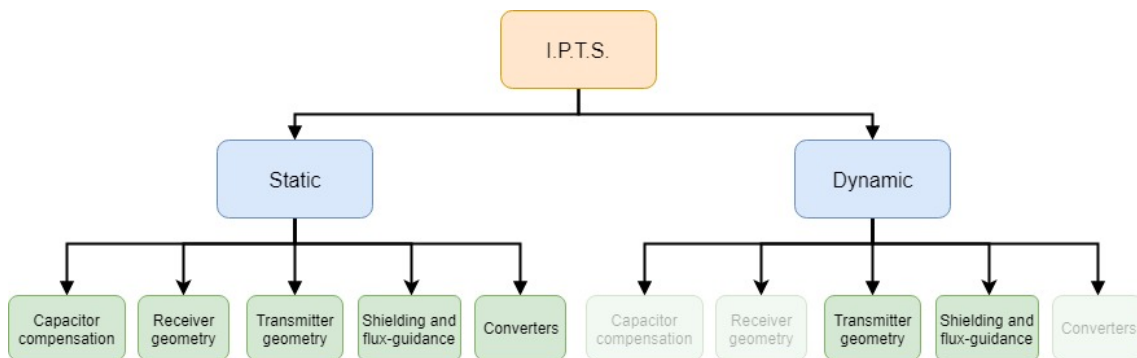
Figure 1.1: Flowchart indicating overlap in component selection.

The static charging will be discussed first, as this will lay the foundation of knowledge on component selection. The dynamic section will then explain which additional measures need to be taken to ensure that the same receiver system can be used on the track while in motion. Various design possibilities are reviewed and the most suitable are selected for use in the determination of the feasibility.

1.2 Go-kart requirements

The requirements of the go-kart are predominant in defining the optimal system configuration of the system, as no compromises are allowed in performance. The industry standard for rental go-karts is used to define these requirements. A commonly used Internal Combustion Engine (ICE) in rental go-karting, is a Honda GX270 4-stroke engine. This engine is relatively low in maintenance and cost, and provides the rental go-kart with enough power to entertain the drivers. The specifications and performance curves of this engine are given in Table 1.1 and Figure 1.3. All these specifications should be matched or out-performed by the electric motor of the Induction Power Transfer System (IPTS) go-kart, to ensure that performance is maintained.

Table 1.1: Specification of Honda GX270 ICE [2].

Engine type	Air-cooled 4-stroke OHV
Peak Power Output[1]	6.3 kW @ 3600 rpm
Peak Torque	19.1 Nm @ 2500 rpm
Dry weight	25 kg
Fuel	Unleaded 86 octance or higher
Length(min)	380 mm
Width(min)	429 mm
Height(min)	442 mm
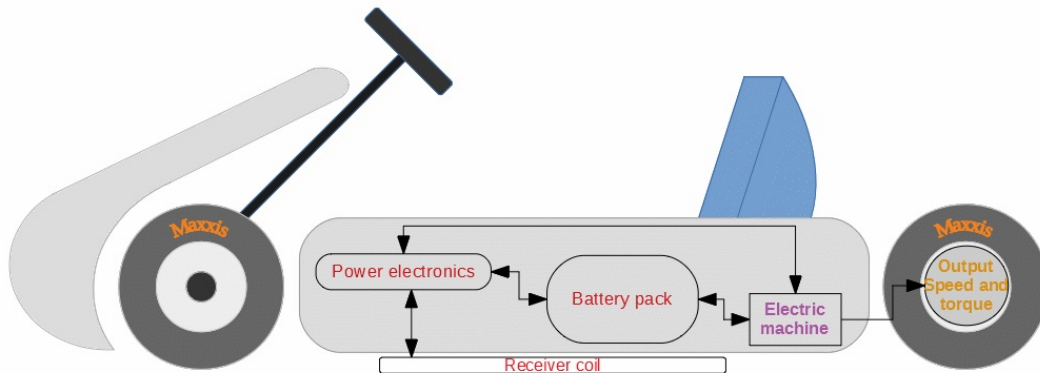
Figure 1.2: Go-kart fitted with a receiver coil.

An overview of the system components of the IPTS go-kart is shown in Figure 1.2. The mechanical components are similar to that of a traditional go-kart with a ICE. The power-drive components are the same as many electric go-karts; except for the required additional power electronics of the coil. The go-kart frame and ground clearance will be assumed to be identical to that of regular go-karts, that has 6 cm clearance. About half of this distance is usable for the installation of the pickup coil, the other half is required as ride height. The pit-lane is assumed to have a guiding system, which ensures that the go-karts are properly aligned with the charging pads to within 5 cm in all directions. Turn Around Time (TAT) is assumed to be 5 minute in normal operating conditions; drivers often have to be exchanged between races.

---

[1]SAE J1349 standard
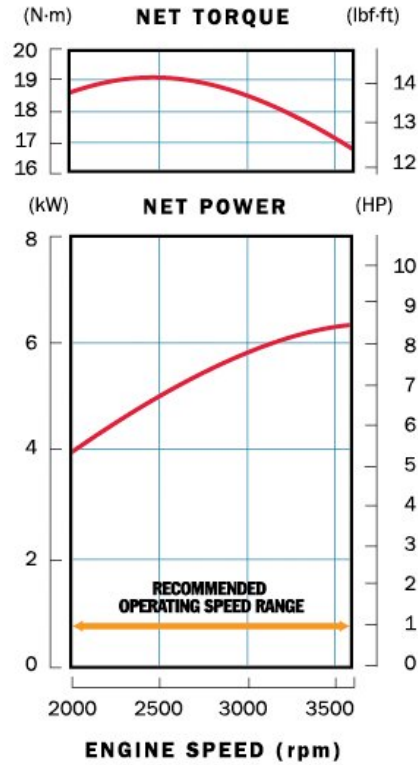
Figure 1.3: Honda GX270 ICE performance curve [2].

1.3 General working principle of an IPTS

An inductive power transfer system is a contactless or wireless power transfer system, that uses magnetic induction to transfer power between two galvanic isolated circuits [3]. The principle of power transfer is the same as that of a transformer, but it has an air-core instead of ferrite-core. In Figure 1.4 a transformer with a ferrite-core is shown in which a varying current in the primary coil produces a magnetic flux. This flux is guided by the ferrite-core through the secondary coil, where it induces a current in the secondary coil. The working of this principle is explained by the Maxwell-Faraday law, shown in equation (1.1); that states that the induced Electromagnetic Field (EMF) around a closed path is negatively equivalent to the change of magnetic flux enclosed by this path over the change of time.

$$\oint_C \vec{E} \cdot d\vec{l} = -\frac{d}{dt} \int_S B_n \cdot dA \tag{1.1}$$

The comparison between a transformer and an IPTS is shown in Figure 1.5. The permeability of air –the amount of magnetization of a material when subjected to a magnetic field– is much lower than that of ferrite. One of the main challenges of an IPTS is to transfer power despite of this low permeability of the core material.

$$M = k\sqrt{L_1 L_2} \tag{1.2}$$

The amount of flux that is guided through the receiver coil determines the coupling of the two coils. The mutual inductance between two coils is determined by equation (1.2), it is determined by the self inductance(L_{coil}) of each coil and the coupling factor k.

$$L_{coil} = \frac{\mu_0 \mu_r N_{coil}^2 A_{coil}}{l_{coil}} \tag{1.3}$$

3
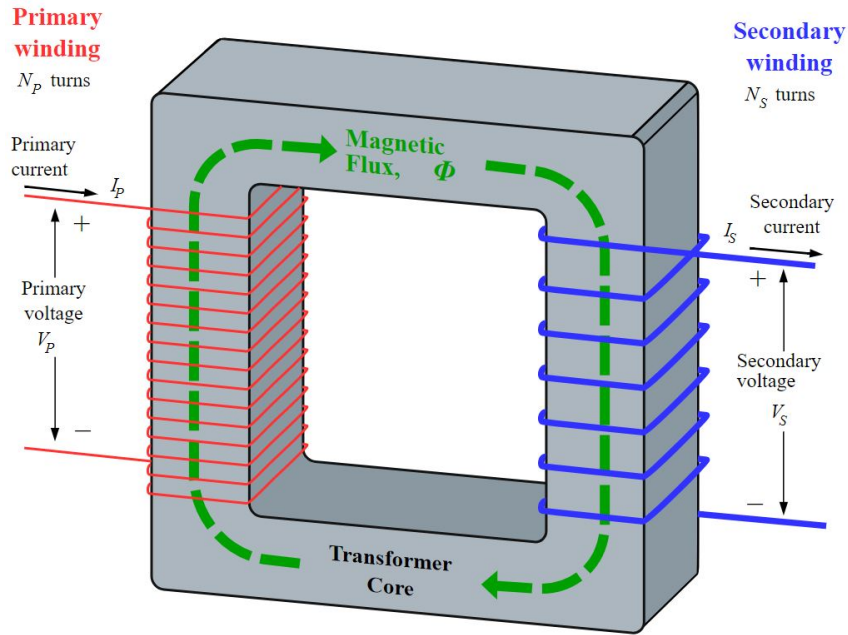
Figure 1.4: Transformer [4].

The self inductance for the coils is determined by equation (1.3). In this equation, A_{coil} is defined as the area of the magnetic core, N_{coil} as the number of turns in series, l_{coil} as the total length, μ_0 the permeability of free space, and μ_r the core materials permeability.

The coupling factor is determined by many variables, like the geometrical positioning relative to each-other and the permeability of the material between them. In ferrite-core transformers this coupling k is often assumed to be 1, as almost all power is transferred. In air-core transformers k is much lower, as less field-lines reach the second coil.
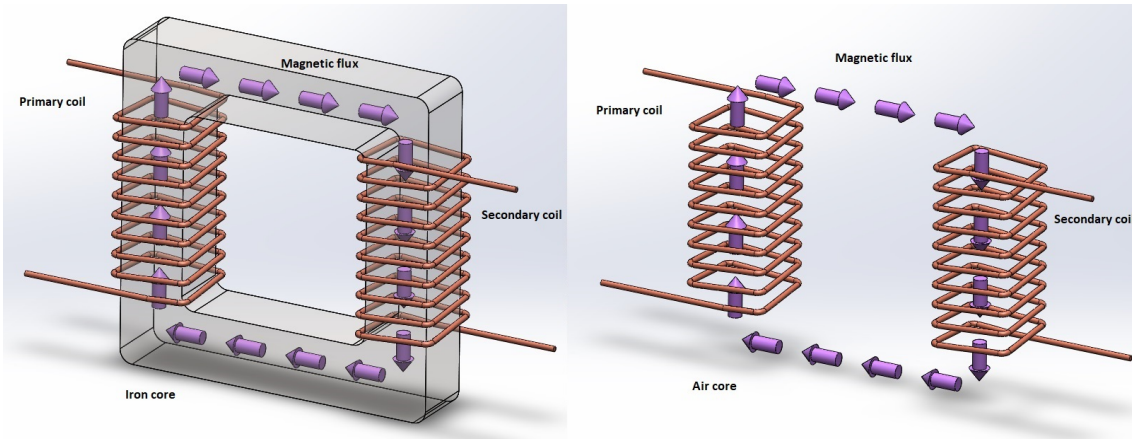
Figure 1.5: Iron-core and Air-core transformers.

The power transferred to the load(P_{su}) of the secondary circuit is shown in equation (1.4), that is comprised by the short circuit current(I_{sc}) (1.5) and the open circuit voltage(V_{oc}) (1.6) [5]. This shows that the power output of an uncompensated IPTS is depended on the frequency, primary current, self inductance of the receiver coil, and the mutual inductance. Increasing these parameters will, therefore, result in more uncompensated power transfer. However, increasing current and frequency provokes undesirable frequency effects and can cause coil heating; these limiting factors are discussed further on. Improving mutual inductance and reducing self inductance is hard to achieve, but is less influenced by undesirable side-effects.

$$P_{su} = V_{oc} * I_{sc} = \omega I_1^2 \frac{M^2}{L_2} \tag{1.4}$$

$$V_{oc} = j\omega M I_1 \tag{1.5}$$

$$I_{sc} = \frac{V_{oc}}{j\omega L_2} \tag{1.6}$$
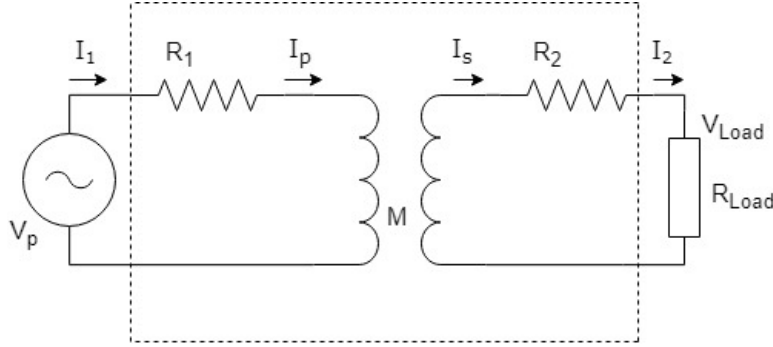
Figure 1.6: Induction Power Transfer System.

Figure 1.6 is a basic circuit representation of an air-core transformer. The voltage source is connected to a coil, that is schematically presented as a resistance and an inductor in series. The receiving coil is represented in the same manner; a resistance and an inductor in series. The load on the secondary side is represented as a resistor: R_L. This configuration is known as a uncompensated IPTS, because no capacitor compensation is applied in the circuit.
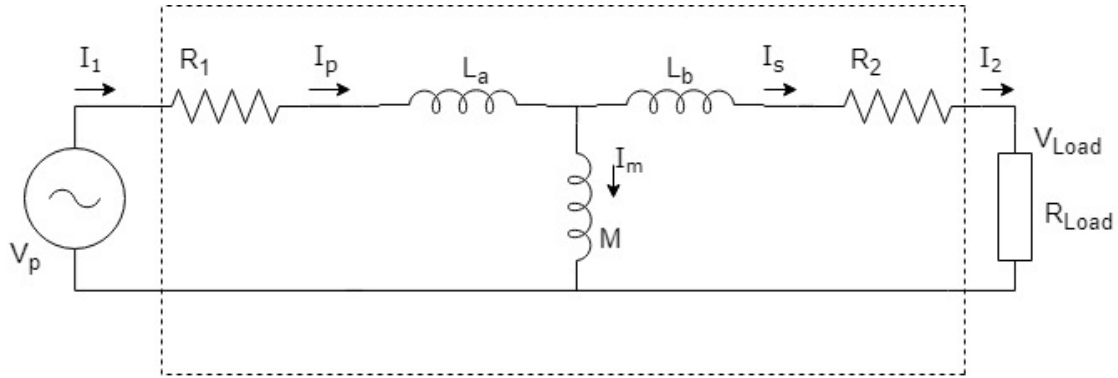
Figure 1.7: IPTS equivalent circuit.

When both coils have the same number of windings/turns, this can also be represented as in Figure 1.7. In this figure both systems are connected and the mutual inductance M is represented as a branch in the circuit parallel to the secondary circuit. Here La and Lb represent the leakage inductance's of the system. For this basic configuration the impedance -complex resistance- as seen by the source is given by equation (1.7). In this equation the coil-resistance of the primary and secondary coil are represented as R_1 and R_2, respectively.

$$Z = \frac{\omega^2 M^2 + (R_1 + j\omega(L_a + M))(R_l + R_2 + j\omega(L_b + M))}{R_L + R_2 + j\omega(L_b + M)} \tag{1.7}$$

The efficiency of the system is defined by the power consumed by the load divided by the sum of all the power consumed by the system. This can be rewritten for the uncompensated circuit to equation (1.8) [3], that shows that increasing the frequency also increases the efficiency. However, this would also increases the impedance of the circuit, which has a negative effect on the power factor. The power factor is the ratio of real power drawn by the load to the apparent power that

flows into the circuit. A small power factor results in the need of over-designed converters, as the converter would need to be able to transfer not only the real power, but also the reactive power. This reactive power circulates in the system, but does not contribute to the power absorbed by the load.

$$\eta = \frac{R_l}{(R_l + R_2)(1 + \frac{R_1(R_2+R_l)}{\omega^2 M^2}) + R_1(\frac{L_b+M}{M})^2} \qquad (1.8)$$

Capacitors can be used in parallel or series to compensate the inductive behaviour of the circuit, which enables the use of higher frequencies; as impedance of the circuit can be reduced by adding capacitors. Chapter 2 will present an overview of several methods of compensation and chooses the most suitable according to the design requirements.

1.3.1 Misalignment

In a ferrite iron core transformer, like the one in Figure 1.4, the magnetic field lines are guided by the ferrite-core. All the field-lines produced in the primary coil are led through the secondary; therefore, coupling can be assumed ideal -k=1- for most calculations as almost no leakage occurs. In static IPTS, the alignment of the coils is fixed and thus k remain the same. In dynamic charging this values changes and thus has a lot of influence on the amount of coupling between the coils.

In an air-core transformer these field lines diverge quickly and therefore the secondary coil should be close to the primary coil to achieve the same power transfer. The horizontal misalignment of the two coils reduces the coupling and increases the leakage inductance [6]. Figure 1.8 shows a secondary coil aligned with the primary, and the magnetic field lines going through them produced by the primary circuit. It also shows how a misalignment can reduce the number of field lines enclosed by the secondary coil. This is of course a problem that occurs in both stationary and dynamic charging; therefore, it is imperative to comprise a system that can cope with this misalignment.
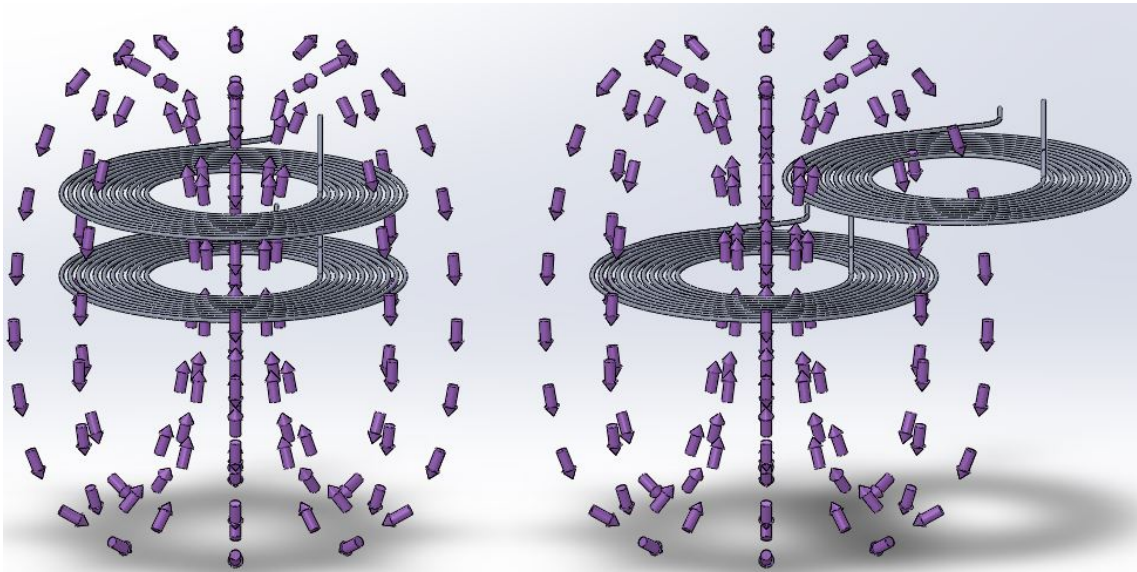
Figure 1.8: Visualization of how misalignment influences the coupling between coil.

For the stationary, wireless charging of go-karts tolerance to misalignment can be minimized by the use of lower-able guide rails with stop-blocks, as the complexity of human caused misalignment on the stationary charger would go beyond the scope of the study. This will therefore be assumed as a given for the rest of this study. For dynamic charging this can not be realized and the dynamic charger should be able to charge in all positions on the track. The minimum amount of power transferred will be used to determine the feasibility in dynamic charging.

1.3.2 Frequency effects

Frequency has an important role in IPTS, as the efficiency of the system (1.8) and the behaviour of many electronic components depends on it. Frequency even has a profound effect on the current density itself in the conduction coils. It is therefore important to understand how these effects influence the system.

Effect in wires

Alternating Current (AC) creates opposing eddy currents in the wires, that are induced by the changing magnetic field around the wire. The resistance of the coils is influenced by both the frequency and the current density [6].

The skin-effect is a important contributor to this increased resistance and understanding this effect can help find methods to reduce this resistance. In the centre of the wire eddy currents oppose the current, while enforcing the current at the edge of the wire as shown in Figure 1.9. As the frequency gets higher, the skin-effect becomes greater. This reduces the effective cross-sectional area of the wire used by the current to flow through. Rendering one part of the wire useless and the other part overloaded with current, as current-density in this area is increased. The reduction of effective area increases the resistance of the wire.
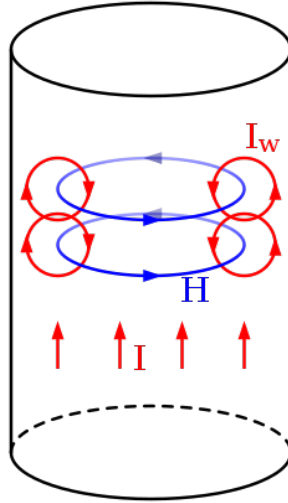
Figure 1.9: Skin-effect [7].

The proximity effect occurs when two conductors are close together with alternating current passing through them. The magnetic flux through the conductor can be reinforced or counteracted by conductors nearby. This results in the current being forced to one side of the wire, depending on the direction of current in the conductors. The resistance of the wire is hereby increased because the current density increases in some parts, while decreasing in others. The strength of this effect depends on the proximity of the conductors and thus the geometry of the coils and wires. This can be analyzed in a design phase with a FEM analysis program. Figure 1.10 shows how two opposing current directions, in wires closely spaced, force the current to the outer edges of the wires.
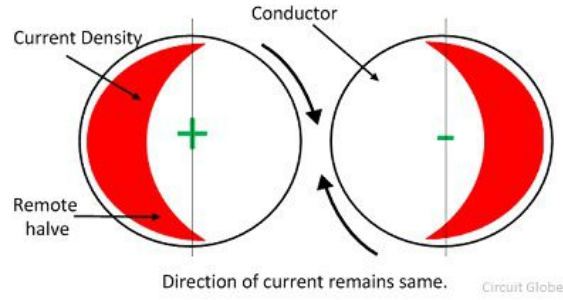
Figure 1.10: Proximity effect [8].

A solution to these problems is the use of Litz-wire; this wire is made out of several thin, isolated wires that reduce the skin-effect. The skin- and proximity effect have effect on both strand- and bundle level. At bundle level both effects can be brought to negligible losses by twisting and weaving the Litz-wire, here the skin-effect requires the most complex pattern [9]. The strand level losses are predominant caused by the proximity effect, as the skin effect is mitigated by the uses of strand with a much smaller diameter than the skin-depth. The skin-depth is calculated by equation (1.9), with μ being the magnetic permeability and σ the conductivity of the material. ω is the frequency of the alternating current in the wire section and it can be seen to determine the diameter of the strands in the equation. The thickness of the strands and the number of strands required have to be calculated to determine the efficiency of the system.

$$\delta = \sqrt{\frac{2}{\omega * \sigma * \mu}} \tag{1.9}$$

Effect in Ferrite-cores

The use of ferrite-cores is common in transformers as they help guide the flux from one coil to another. For an IPTS this same principle can be used in the areas where ferrite can be fitted. The choice of ferrite is based on reduction of the hysteresis- and eddy current-losses.

The eddy current losses are induced by the alternating magnetic field around the ferrite. However, the ferrite is used to guide flux and should not function as a conductor. Eddy current losses can therefore be minimized by constructing the core out of a material with a high electrical resistance.

Hysteresis losses are due to the rotation of magnetized domains in the material, that try to line up with the external magnetic field. The harder a material, the more energy that is required to rotate the domains, as shown in Figure 1.11. Therefore, the core is constructed from a soft ferrite, which has a small hysteresis due to the soft composition, but a very high electrical resistance.
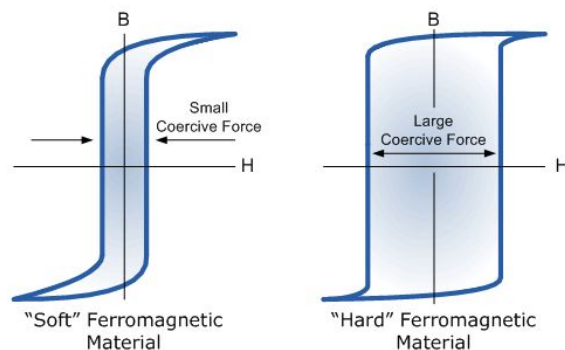
Figure 1.11: Hysteresis in soft and hard ferromagnetic materials [10].

1.4 Static wireless inductive charging

1.4.1 Topology of coils

As the topology of the coils is of influence to the power transfer capabilities, it is an important consideration in the design of both static and dynamic inductive charging. In literature a vast amount of different topologies of coils is investigated, with simple spirals –like circular and rectangular– being the most common ones. However, new topologies with higher efficiency, better tolerance to misalignment, and higher power-transfer capability –like DDQ coils– are getting more attention as the need for efficiency increases. Figure 1.12 shows an overview of several different coil topologies that can be considered for various applications of IPTS.

Figure 1.12: Overview of several common topologies [11].

The coils from Figure 1.12 were evenly sized and compared by the weighted evaluation criteria from Figure 1.13; the resulting overall score is shown in Figure 1.14. The six highest scoring topologies were:

- Square
- Circular
- Rectangular

- DD
- DD overlapped
- DDQ

TABLE IV.	Overview of Summarized Evaluation Criteria	
Coupling factor absolute	(1)	
Gradient of coupling with variation of air gap	(2)	
Gradient of coupling with lateral misalignment	(3)	
Magnetic flux density at vehicle body up to a nominal lateral misalignment	(4)	
Magnetic flux density at vehicle body with a large lateral misalignment and specific air gap	(5A-5D)	
Decrease of magnetic flux density transverse to the direction of travel	(6)	
Transferred power up to a nominal lateral misalignment	(7A)	
Transferred power with a large lateral misalignment	(7B)	
Mass of copper	(8)	

Figure 1.13: Evaluation criteria for topologies [11]
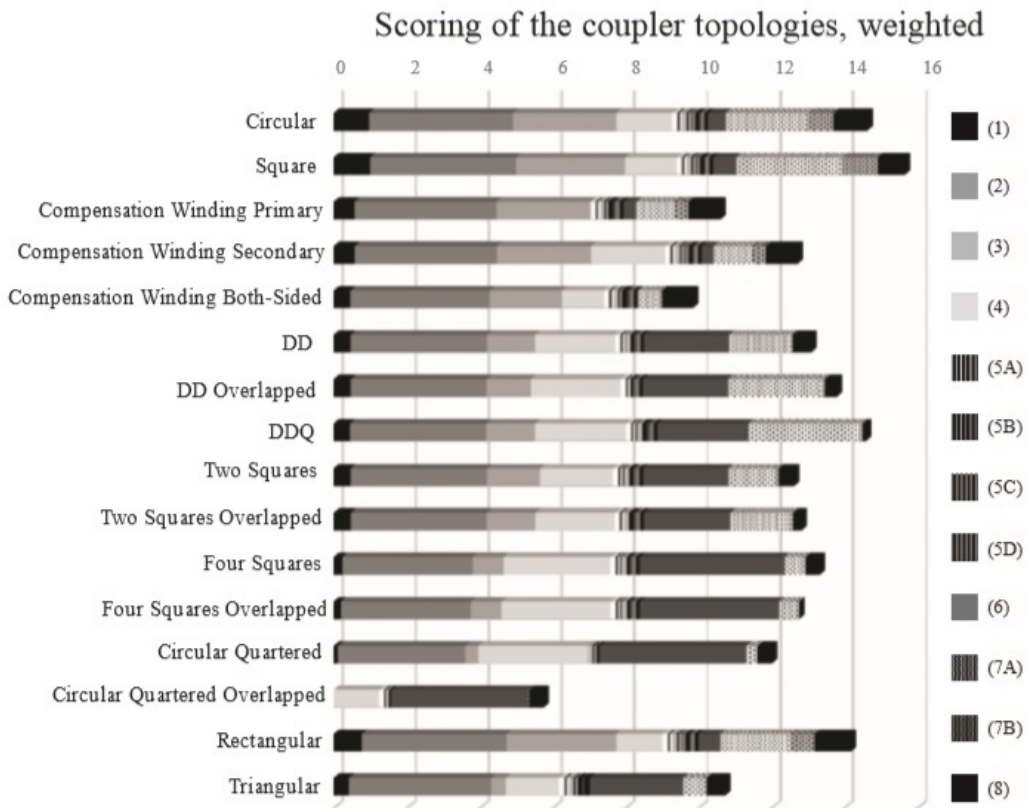
Figure 1.14: Scoring of topologies [11]

Sizing effect on coils

The scores are grouped in four different clusters based on similarities in strengths and weaknesses, shown in Figure 1.15. This also shows how an increase in size relates to the increase in coupling; as the coil-diameter is increased from 500mm to 950mm, but the coupling factor is not increased the same for all topologies. It shows that the more complex configurations have a larger increase in coupling factor, whereas the simple geometries are less effected by the enlargement of the coils. As these complex topologies had a much lower score to begin with, it can be concluded that they will need to have sufficient space to function properly. Due to the installation space in a go-kart and added complexity, the forms from cluster 2 are unsuitable for the application of this research.
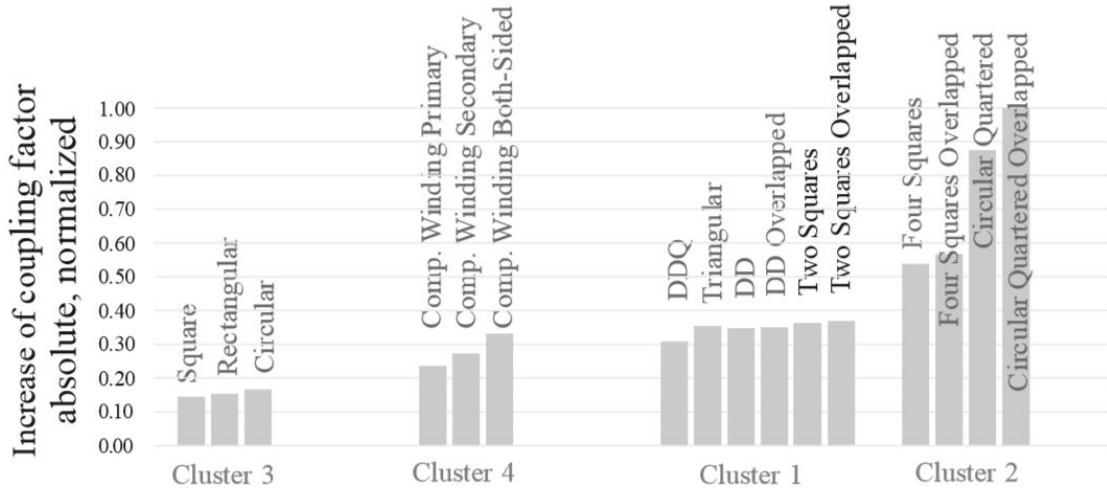
Figure 1.15: Increase of coupling factor due to increase of coil size [11]

Decoupling of coils

It is important to prevent undesired coupling between coils, when using multiple coils in a single receiver. This coupling of coils is seen when misalignment is introduced. If perfectly aligned, coils have the same induced voltage and do not affect each other. When a misalignment occurs, one coil receives more magnetic flux than the other and coils can induce a coupling current in the other coil. To prevent this, the decoupling of coils is required [12]. For decoupling of the two DD coils there are two options; The first is frequency control, which is possible in static charging but undesirable in dynamic charging as multiple pickup can prevent frequency tuning from being possible. The second option is to overlap both coils in such a way, that the induced magnetic flux from one coil in the other is canceled by the overlap. This will thus be the preferred option in the design for go-karts. The decoupled DD coils are represented in previous figures as the DD overlapped. However, this decoupling should be done in the product detailing, not in the feasibility study as it is part of the optimization of the charger.

Compensation windings

The purpose of the compensation winding in cluster 4 was to reduce the magnetic field and leakage field outside the coils. This is achieved by running the current in the outer winding in opposite direction of the current in the inner windings. However, the power supply required to create this active shield adds weight, size, and complexity to the system as magnitude and phase need to be determined [6]. All these requirements are undesired for the go-kart application, as the goal is to reduce the weight. For this reason, the topologies of cluster 4 are also undesirable for this application.

Flux guidance and shielding

The performance of the coils can be enhanced by the guidance of flux, using ferrite. Analysis of the effect of flux guidance and shielding in coil topology shows that the scores are improved, but

no significant change in their mutual inductance ratios is detected [13]. Shielding, flux guidance and safety requirements will be further discussed in Section 1.4.4.

Stationary transmitter coil

The design chosen for the stationary transmitter is the DD coil. As previously determined, the coils from clusters 2 and 4 unsuitable and the power profiles from Figure 1.16 [14] show that the use of a DD transmitter can drastically improve the power transmitted, when compared with a circular transmitter. As circular coils are clustered with rectangular and square coils, similar results can be expected from these types of coils.
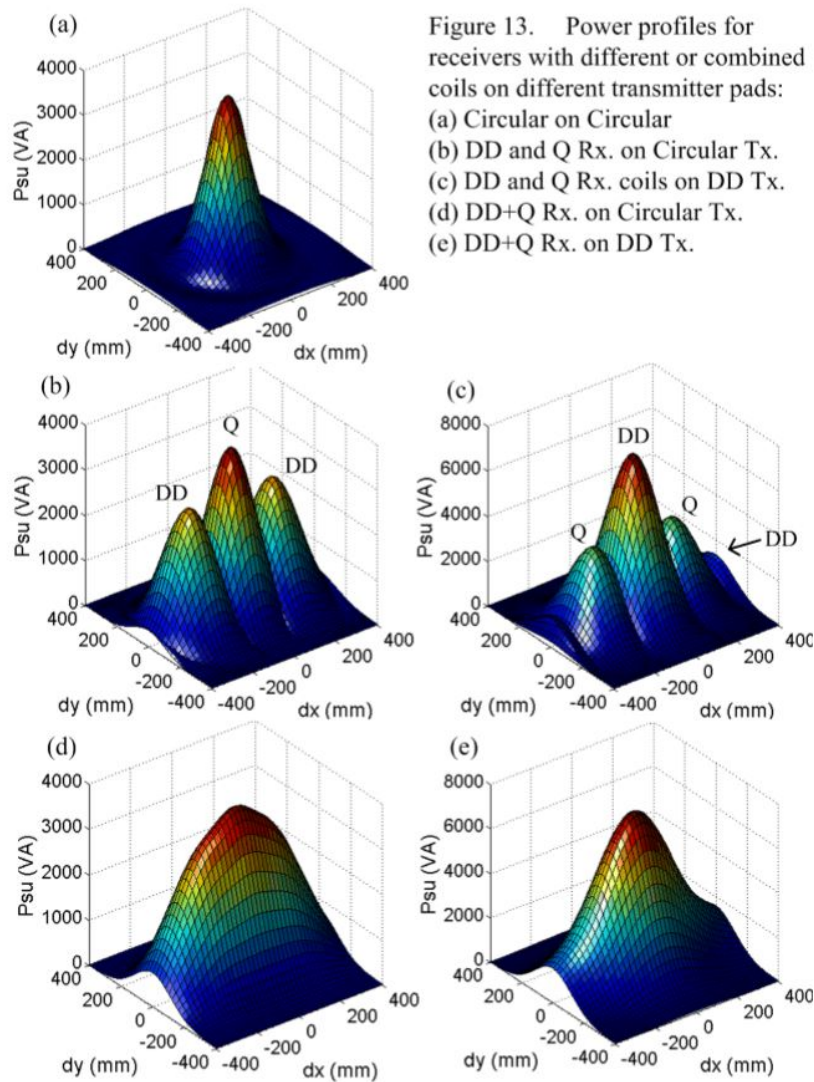
Figure 13.   Power profiles for receivers with different or combined coils on different transmitter pads:
(a) Circular on Circular
(b) DD and Q Rx. on Circular Tx.
(c) DD and Q Rx. coils on DD Tx.
(d) DD+Q Rx. on Circular Tx.
(e) DD+Q Rx. on DD Tx.

Figure 1.16: Power profiles of receivers and transmitters [14]

Receiver coil

Regarding the previously stated and the fact that misalignment is fairly small, the topologies from cluster 3 would be preferable due to their simple design and thus low construction cost. However, as the receiver coils will have to be used in both static and dynamic charging, and will thus encounter misalignment in the dynamic case, the DD coil receiver would be more suitable. Considering this dynamic case is important and Section 1.5 will elaborate further on this receiver coil.

1.4.2 Compensation methods

For circuits driven by alternating currents the impedance –complex resistance– of a circuit depends on the frequency of the current. The equation for the complex resistance –impedance– for resistors, inductors, and capacitors are given by equations (1.10), (1.11), and (1.12), respectively.

$$Z_R = R \tag{1.10}$$

$$Z_L = j\omega L \tag{1.11}$$

$$Z_C = \frac{1}{j\omega C} \tag{1.12}$$

The real part of this complex resistance represents the real power used in the circuit, this is the part which can actually be used to do work. The imaginary part represents the reactive power, which is in the circuit but not usable.

Figure 1.17 shows how apparent, reactive and active power relate to each-other. The comparison with a mug of beer simplifies the principle of complex resistance in a circuit. The apparent power is the mug, the reactive power is the foam, and the active power is the beer. The usable energy –beer in this case– is only a portion of the whole mug, and the only way to get more beer in the same mug is by getting rid of some of the foam. For electrical circuits this works in the same manner, where a smaller portion of reactive power allows for more active power without overloading the system components.

(a) Vector representation of power [15].

(b) Beer mug metaphor for power [16].
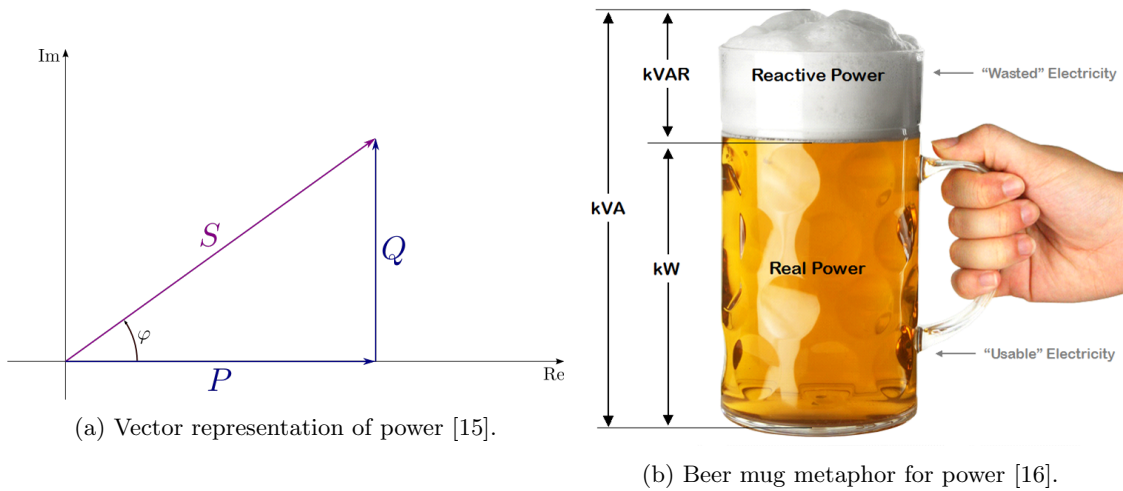
Figure 1.17: Apparent, reactive and active power.

As the the frequency of the system is increased to maximized the efficiency of the circuit (1.13), the impedance of the circuit is increased by the inductors. This increases the amount of reactive power in the circuit; due to the coils dependency on frequency (1.11). Capacitor compensation can be used to compensate for the inductive nature of the coils and keep the apparent power as close to the active power as possible. Hereby, the reactive power is minimized and the load is seen as purely resistive by the source. If an equilibrium between inductors and capacitors is achieved, the system is said to be in resonance.

$$\eta_{uncompensated} = \frac{R_l}{(R_l + R_2)(1 + \frac{R_1(R_2 + R_l)}{\omega^2 M^2}) + R_1(\frac{L_b + M}{M})^2} \tag{1.13}$$

Several topologies can be used to achieve this minimization, but four are most widely studied. These four compensation topologies, shown in Figure 1.18, are the following:

- Series-Series topology
- Series-Parallel topology
- Parallel-Series topology
- Parallel-Parallel topology
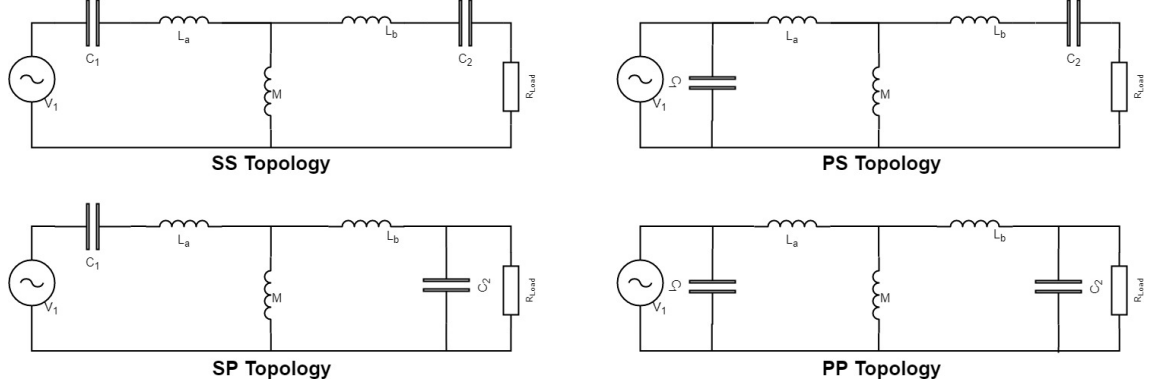
Figure 1.18: Capacitor compensation topologies.

For the calculation of the secondary side capacitor, equation (1.14) is used. This is the same for all topologies and is derived from the required impedance of the secondary circuit. The compensation on this side is used to enhance the power transfer capability [3] [11] [17] [18].

$$C_2 = \frac{1}{\omega_0^2 (L_b + M)} \tag{1.14}$$

On the primary side the compensation depends on the desired topology, that are shown in Table 1.2. On this side, the capacitor is used to minimize the VA-rating on the source side of the system [3] [11] [17] [18].

Table 1.2: Primary capacitor compensation formulas.

Compensation topology	Primary capacitance
SS	$\frac{C_2(L_b+M)}{L_a+M}$
SP	$\frac{C_2(L_b+M)^2}{(L_a+M)(L_b+M)-M^2}$
PS	$\frac{(L_a+M)(L_b+M)^2 C_2^2 R_L^2}{(L_a+M)(L_b+M)R_L^2 + M^4}$
PP	$\frac{C_2((L_a+M)(L_b+M)-M^2)(L_b+M)^2}{((L_a+M)(L_b+M)-M^2)^2 + M^4 R_L^2 (L_b+M)C_2}$

All compensation methods have their strengths and weaknesses, that can be tuned for optimal use in the system. However, some capacitor compensation methods requires good alignment or a very precise frequency control to ensure that the system remains in resonance. The requirement to allow misalignment of the charger and the go-kart, implies that misalignment becomes part of the consideration when choosing the compensation method.

Bifurcation

When in resonance, the phase difference between the supply voltage and supply current is zero. A shift in alignment or even temperature, influencing the capacitors, could case the system to no longer operate in resonance. Here, the phase angle between the voltage and current will not be zero. This causes higher switching losses due to the hard switching of the inverter. The phase angle between the voltage and current can be reduced by adjusting the frequency, which is called variable frequency control.

A drawback to the use of variable frequency control is that it creates the possibility of multiple zero phase angle frequencies. The existence of a multiple of frequencies, at which there is a zero phase angle, is called bifurcation. Of these multiple frequencies, only one is the resonant frequency at which the system operates as intended. It is therefore important to prevent bifurcation from happening, as it can cause the system to not operate at the optimal point for power transfer.

As multiple pickups will have to use the same transmitter, the design requires fixed frequency control. Bifurcation will therefore not be an issue for the studied setup. It is, however, important to keep in mind when designing a system, as new methods of approach could result in a system which does use variable frequency control.
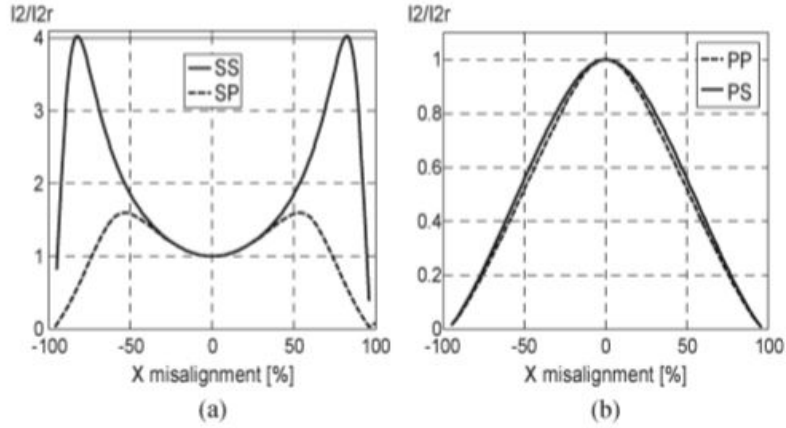
Fig. 4. I_2/I_{2r}. (a) SS and SP topologies. (b) PS and PP topologies.
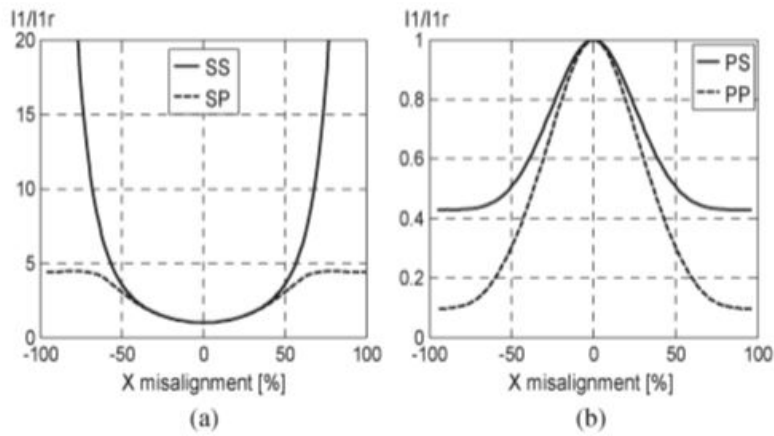
Figure 1.19: Normalized current ratings for a wide range of misalignments [19].

Misalignment in capacitor compensation

When using aligned coils, all compensation topologies can transfer power at their rated power. However, when a misalignment is introduced, the mutual inductance of the coils changes. This shift in mutual inductance pushes the system out of resonance as the capacitor values, inductor values, and operating frequency are fixed. Figure 1.19 shows how misalignment can change the ratio of current to the designed current ratings if the aforementioned parameters are fixed.

For parallel compensation on the primary side, the source current(that is on the primary side) drops off steeply; the load current(that is on the secondary side) also drops off in the same manner. This means that the amount of power that can be transferred by the system is reduced, but both currents in the system will not exceed their ratings because of a misalignment of the coils. Consequently compensation with a parallel capacitor on primary side is safe in the absence or great misalignment of a secondary coil, but is unable to transfer the rated power if not perfectly aligned.

For series compensation on the primary side, a different effect takes place. Here the current on both sides becomes far greater than their ratings. This compensation is thus able to transfer power even beyond its rating if misalignment occurs, but in a manner that is unsafe for its source. For a small misalignment, an over sized power source could be used to transfer the required amount of power. However, this would of course bring into question the efficiency of the system and its safety. Another possibility would be to control the system in such a manner that it cuts of if certain current values are exceeded.

SPS compensation

There is an alternative to the 4 most common topologies, namely the SPS topology that consists of both a series and parallel capacitor on the primary side. This topology is shown in Figure 1.20 and offers significant improvement in power transfer when the coils are misaligned in static testing. Experiments were conducted with a 2 kW SPS-compensated and SS-compensated system over a 15cm gap, using a fixed frequency control and a square voltage waveform. The results of these experiments show much higher misalignment without power loss in the SPS-compensated system, when compared to the SS-compensated system [19].
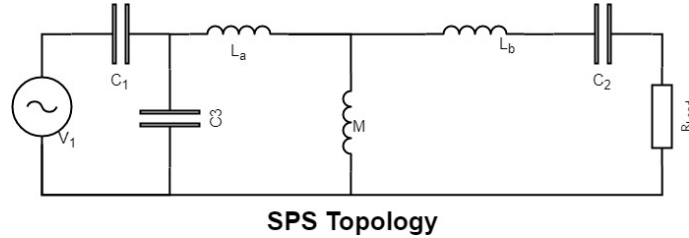
Figure 1.20: SPS compensation topology

The results of the currents in the SPS-sytem with respect to their rated values in the primary side(a) and secondary side(b) are shown in Figure 1.21. To prevent current peaks a $700\mu H$ inductor was connected in series to prevent current peaks. This could also be avoided by using a current source. As can be seen for the figure, a great misalignment can be compensated without over-sizing the power source. For the static charging this would thus be the preferred option, as SPS topology eliminates the need of high precision alignment or frequency control in static charging. However, as this systems characteristics are unknown for dynamic charging, it should be further investigated before considering it as an alternative of the well-known SS topology for battery charging.
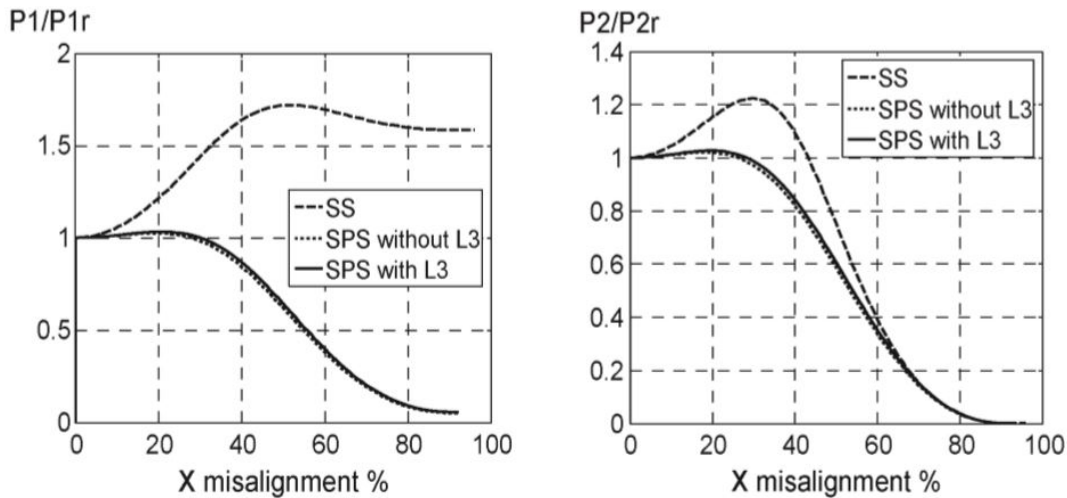
(a) Primary current over primary rated current in SPS-compensation.

(b) Secondary current over secondary rated current in SPS-compensation.

Figure 1.21: Normalized current ratios for a wide range of misalignments [19]

Go-kart compensation

For the charging of batteries, an SS topology is recommended as it is able to function as both a constant current-source and a constant voltage-source, which is desirable in the charging of lithium ion batteries [3]. The use of lithium-ion batteries is advised in go-karts, due to their high specific energy.

Other reasons to choose this topology over others, is the fact that it will only draw active power and is independent of mutual induction and load. The capacitance is determined by the self-inductance of both coils as well as the frequency of the system.

1.4.3 Converters types

For the conversion of electrical energy from source to load converters are required. They are used to alter the voltage, frequency, or a combination of both of an input signal. The most commonly used will be briefly explained, after which the required converters are selected for the use in the IPTS. In all cases the steady-state operation is assumed, as transient state is beyond the scope of this research.

Buck converter

A buck converter, shown in Figure 1.22, is used to scale down the voltage. When the switch is turned on the inductor and load are supplied with energy from the source, at this stage the diode is reversed biased. When the switch is turned off the diode becomes forward biased and the energy stored in the inductor is transferred to the load. A large capacitor is used to smooth the voltage at the output.

The portion of the time that the switch is connected(t_{on}) determines the output voltage(V_o). Equation (1.15) shows that the ratio between the output voltage and the the source voltage(V_s) is equal to the ratio between the time that the switch is connected and the total time of a switching period, the latter is known as the the duty ratio(D). This duty ratio always has to be larger than zero, as otherwise no energy transfer would take place. If the duty ratio would equal one, the source voltage and output voltage would be equal in this setup. The smaller the duty ratio gets, the lower the output voltage becomes.

$$\frac{V_o}{V_s} = \frac{t_{on}}{T_s} = D \qquad (1.15)$$
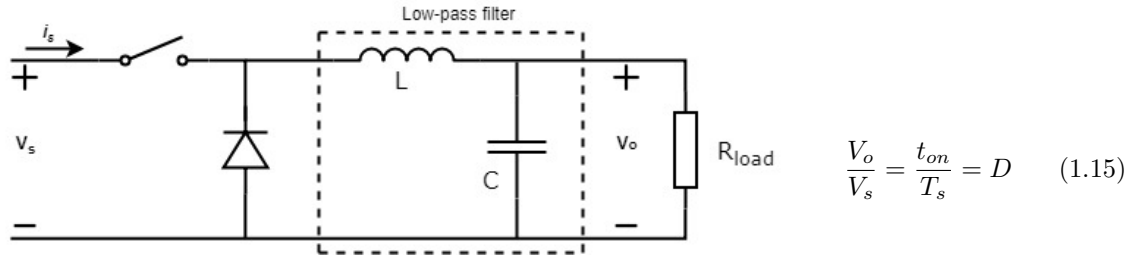
Figure 1.22: Electrical schematics of a Buck converter.

Boost converter

A boost converter, shown in Figure 1.23, is used to scale up the voltage. When the switch is turned on energy is stored in the inductor, at this stage the diode is reversed biased. When the switch is turned off the diode becomes forward biased and energy from the source and the inductor are delivered to the load. A large capacitor is used to smooth the voltage at the output, just like in the buck converter.

The duty ratio is defined as the time a switch is on over the total switching time, as previously stated. The ratio between the output voltage and the the source voltage(V_s) is equal to the ratio between the total time of a switching period and the time that the switch is disconnected. Equation (1.16) shows that the portion of the time that the switch is disconnected(t_{off}) determines the output voltage(V_o). The output voltage is increased as the duty ratio gets higher.

$$\frac{V_o}{V_s} = \frac{T_s}{t_{off}} = \frac{1}{1-D} \qquad (1.16)$$
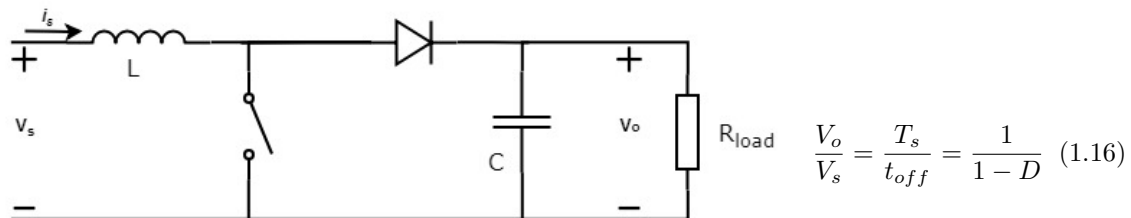
Figure 1.23: Electrical schematics of a Boost converter.

Buck-Boost converter

A buck-boost converter, shown in Figure 1.24, can be used to either scale up or down the voltage. However, the output voltage equals the negative of the input. When the switch is turned on energy is stored in the inductor, at this stage the diode is reversed biased. When the switch is turned off the diode becomes forward biased and energy from the source and the inductor are delivered to the load. Again, a large capacitor is used to smooth the voltage at the output.

$$\frac{V_o}{V_s} = D\frac{1}{1-D} \qquad (1.17)$$
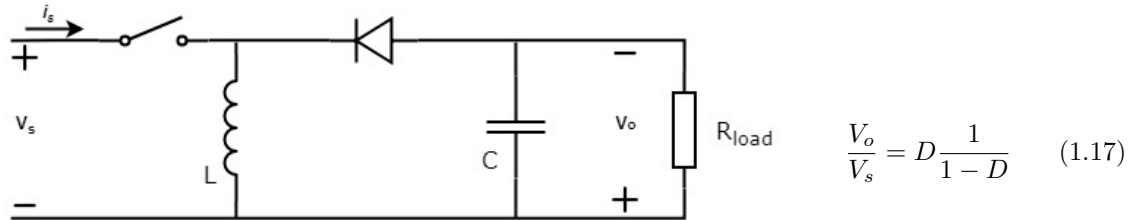
Figure 1.24: Electrical schematics of a Buck-Boost converter.

Half bridge inverter

A half bridge inverter, shown in Figure 1.25, can be used to convert a DC input in a scaled down AC output. The voltage between the upper leg of the the voltage output(V_o) and the ground can be either $+V_s/2$ or $-V_s/2$ depending on which switch is activated. Equal capacitors should be used to keep the potential difference between the negative terminal and the ground constant.
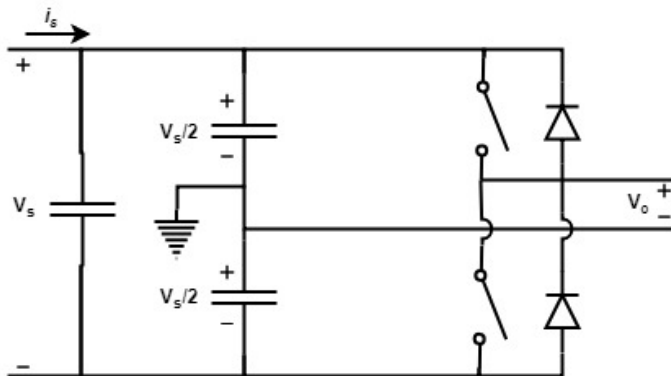
Figure 1.25: Electrical schematics of a Half bridge inverter.

Full bridge inverter

A full bridge inverter, shown in Figure 1.26, can be used to convert a DC input to an AC output. If the same switching is used as in the half bridge inverter, the voltage between the upper leg of the the voltage output(V_o) and the lower leg can be either $+V_s$ or $-V_s$, as switches are paired. The averaged value again is used as output voltage.
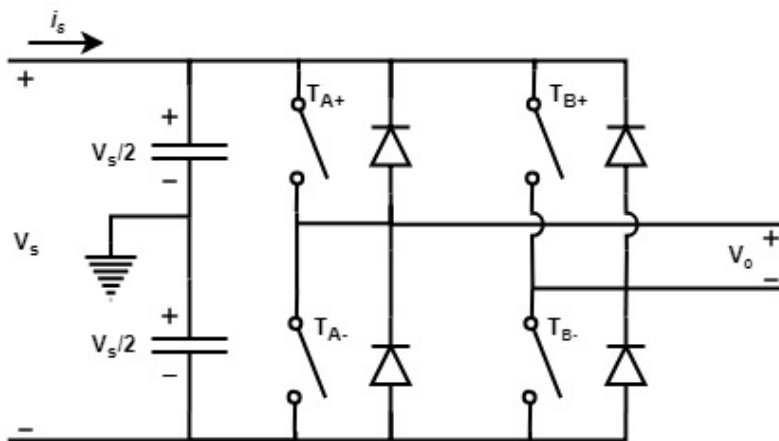
Figure 1.26: Electrical schematics of a Full bridge inverter.

Pulse width modulation

A commonly used technique to control the switches in both half-bridge and full-bridge inverters is Pulse Width Modulation (PWM). A triangular signal is compared to a sinusoidal control signal of the desired frequency. When the triangular signal exceeds the control signal a comparitor activates the switch connected to the positive terminal, while using a not function to deactivate the switch connected to the negative terminal. When the triangular signal is exceeded by the control signal the switches are reversed. This creates a series of peaks and valley that, when averaged, are equal to the desired sinusoidal signal. In full-bridge inverters the amplitude of the output voltage would be equal to the DC input voltage, in half-bridge inverters this output voltage would be half the DC input voltage. In Figure 1.27 this technique is represented in the first two graphs for a full-bridge inverter; in which case it is know as bi-polar switching.

In a full bridge inverter another technique could also be implemented. This allows the potential difference between the legs to become zero, by switching either both positive or negative switches at the same time. Here a inverse control voltage is used to activate the second set of switches. This cuts the voltage jumps in half at the output and also greatly reduces the harmonics of the output signal. This is shown in Figure 1.27 as uni-polar switching; where the potential differences of the individual legs and the summed output voltage are shown in the lower three graphs.
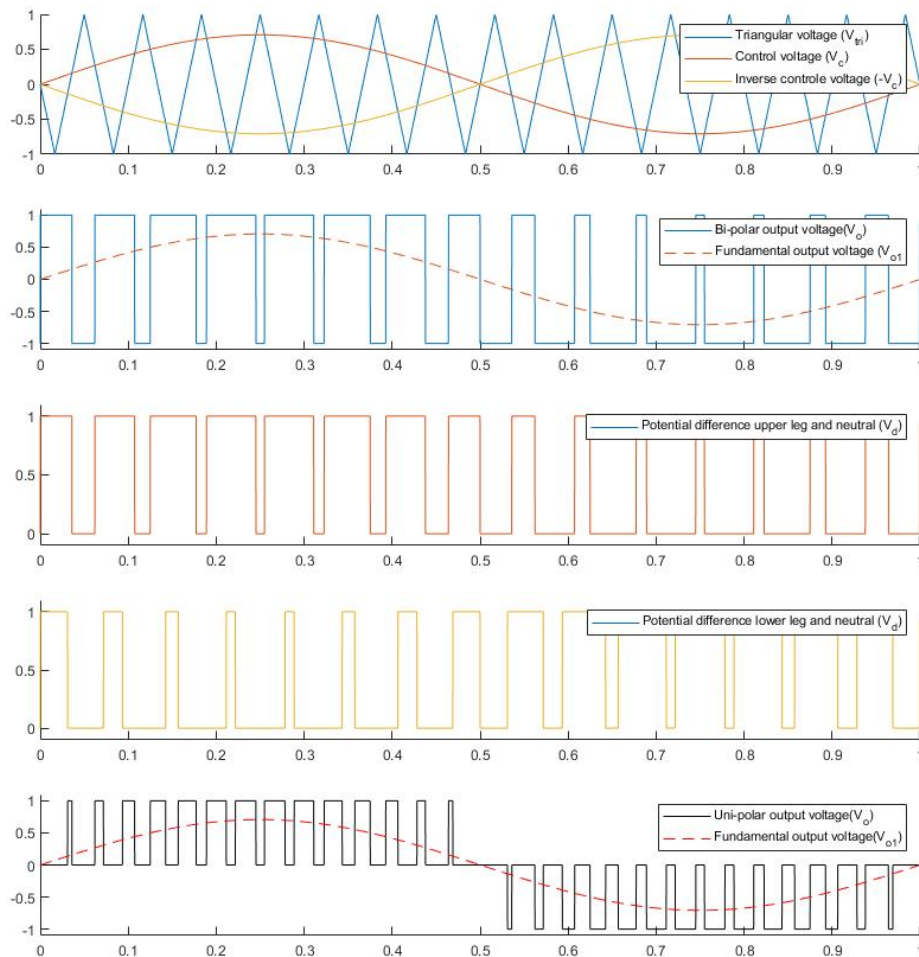
Figure 1.27: Uni-polar and Bi-polar switching methods.

Converters in IPTS

An overview of the stages of conversion of electrical energy in an IPTS is given in Figure 1.28. In this overview, each step of the conversion of power between the power source and the load is given. The dashed box indicates where the power transfer –with compensation– from Figure 1.18 takes place.
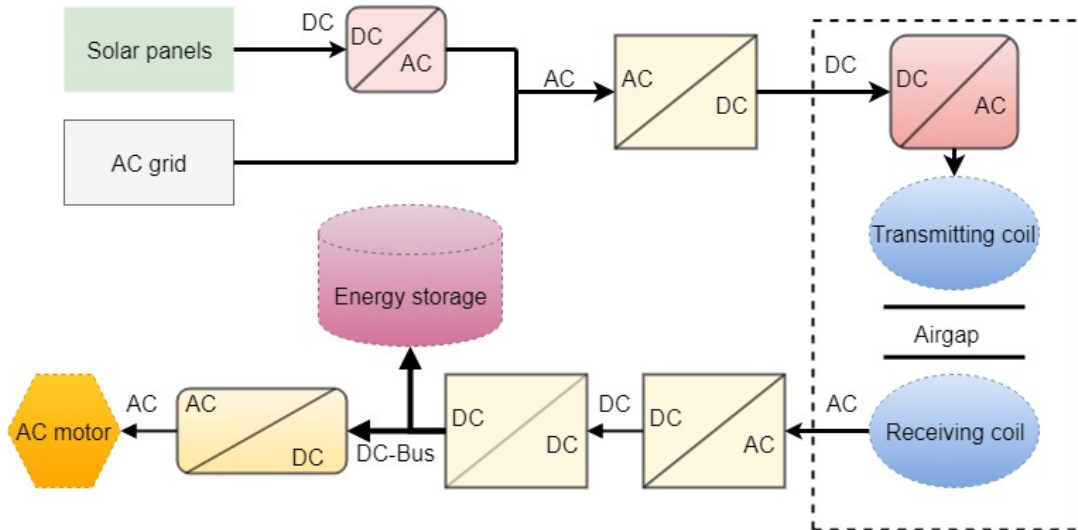
Figure 1.28: From source to load conversion steps in an IPTS.

The first step in constructing a converter for an IPTS is the identification of the power source, as it is important to understand what converter is needed. Usually this is the 3 phase network, but solar panels could also be used and this would require a different converter. The following steps show what converter-steps are needed from this initial step in an IPTS:

- rectification/sizing of voltage to desired Direct Current (DC)
- inverting to a high frequency AC
- rectification of induced high frequency AC
- adaptation to load requirements

For the connection to the AC grid, a full bridge three phase rectifier will be needed to create a DC and have a stable input for the creation of the high frequency AC. For the solar-panel buck-boost converter should be used. In most cases this will act as a step down converter, as solar panels can be arrange in series to create a high DC voltage. However, as common practice is to install an inverter behind solar-panels to be able to deliver power back to the grid when not used, this will probably be a more standardized option. This choice depends on the difference in costs between an inverter and a step down converter, as the power delivered back to the grid should eventually make up for the extra expenses.

After the rectification a high frequency full bridge inverter is used, controlled by PWM to create a high frequency AC. After the transmission via the coils the received power should be converted to be put into the battery pack, or used to power the motor. Here, a full bridge rectifier is used to create a stable DC which can be used for both applications. A Buck converter will be used to scale the voltage back to battery levels, as the voltage level will be kept high after rectification to enable the use of smaller cables.

1.4.4 Shielding and Safety

As the IPTS will be applied to rental go-karts, public and staff will be close to these systems; therefore, their safety should be examined during all stages of development. The International Commission on Non-Ionizing Radiation Protection (ICNIRP) has developed several guidelines in recent years regarding magnetic field limits for different frequency domains. [20] There is a clear distinction made in the under and above 100kHz domain, as heating plays a role in domains above

100kHz. Figure 1.29 shows the allowed electric and magnetic field levels for a wide frequency range. The shield design should be able to keep magnetic field levels around the go-kart within these limits. All designs should be verified with FEM analysis and measurements on the finalized product need to be conducted; to ensure that magnetic field levels are within limits. The effects of flux guidance and shielding will first be explained, after which required precautions for shielding will be discussed.

Table 4. Reference levels for general public exposure to time-varying electric and magnetic fields (unperturbed rms values).

Frequency range	E-field strength E (kV m^{-1})	Magnetic field strength H (A m^{-1})	Magnetic flux density B (T)
1 Hz–8 Hz	5	$3.2 \times 10^4/f^2$	$4 \times 10^{-2}/f^2$
8 Hz–25 Hz	5	$4 \times 10^3/f$	$5 \times 10^{-3}/f$
25 Hz–50 Hz	5	1.6×10^2	2×10^{-4}
50 Hz–400 Hz	$2.5 \times 10^2/f$	1.6×10^2	2×10^{-4}
400 Hz–3 kHz	$2.5 \times 10^2/f$	$6.4 \times 10^4/f$	$8 \times 10^{-2}/f$
3 kHz–10 MHz	8.3×10^{-2}	21	2.7×10^{-5}

Notes:
- f in Hz.
- See separate sections below for advice on non sinusoidal and multiple frequency exposure.
- In the frequency range above 100 kHz, RF specific reference levels need to be considered additionally.

Figure 1.29: Table with reference levels of magnetic and electric fields [20]

Effects of shielding and flux guidance

An important aspect in all topologies is flux guidance and flux shielding, as it leads to a substantially higher power transfer capability and ensures that the EMF in specific areas around the coils does not exceed the set limits by the ICNIRP [20] [21]. How this shielding and guidance can be used on DD- and circular coils is shown in Figure 1.30, in which aluminum is used as a shield for the magnetic field and ferrite is added to guide the flux around the coils. Other materials –like copper– can be used to shield magnetic fields as well, but aluminum is often chosen because it is cheap and provides a rigid framework to which the ferrite and coils can be attached.

In Figure 1.31 a comparison is shown that indicates how the addition of aluminum and ferrite influence the self-inductance, mutual inductance, coupling factor and EMF. As can be seen from this figure both cases alone come with undesired side-effects like a low coupling factor or high EMF. However, combined they enhance coupling and reduce EMF. As stated before, no significant change in their mutual inductance ratios was detected between coil topologies with and without shielding and flux guidance [13]; that means that the conclusions on the desired coil topology still holds. Finite Element Method (FEM) analysis in the final design is required to ensure that the right dimensions of the guidance and shielding is chosen, as this can greatly influence the cost and weight of the system.

Shielding precautions

For the shielding to work a FEM analysis will have to be performed of all possible charging scenarios and these should later be verified. Also, a shut-down procedure needs to be in place that ensures the safety of all people in the vicinity of the system. As well as foreign object detection, which prevents the heating foreign objects and can be achieved by using a Power Loss Detection (PLD) method [22].

For static charging in pit lanes, sensors or camera's could be used to ensure coils are only active when a receiver –go-kart– is positioned above it. Thus, excluding the option of a primary coil transmitting without a receiver. The fact that a go-kart has so little ground clearance does not only provide better coupling than in normal road cars, it also helps prevent animals and humans from getting (parts of) their bodies between two transmitting coils. Plastic bumpers and warnings
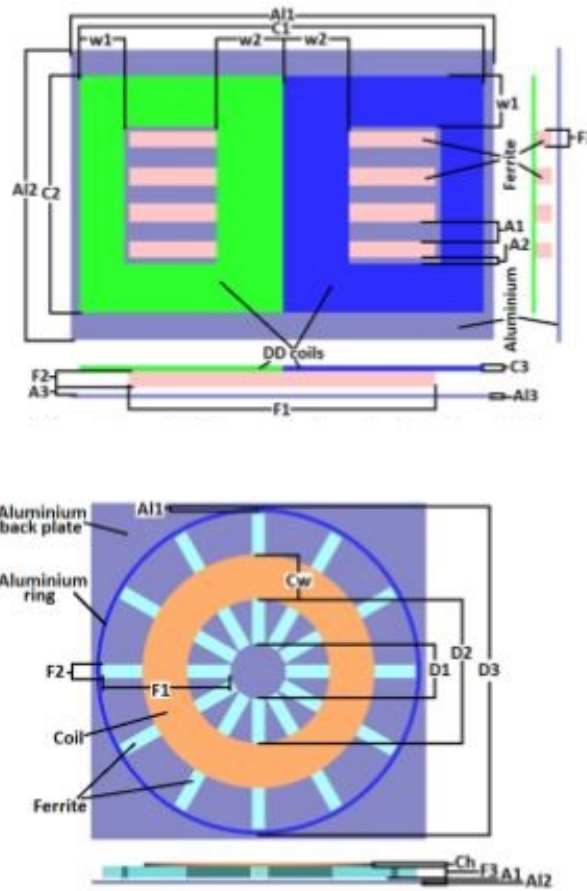
Figure 1.30: Shielding and flux guidance in DD en Circular coils [12].
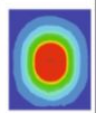
	Air core coil	With ferrite	With aluminum	With ferrite & aluminum
Self-inductance [uH]	13.59	25.39	2.54	22.91
Mutual inductance [uH]	3.58	9.94	0.06	7.55
Coupling factor	0.26	0.39	0.02	0.33
Magnetic flux density at vehicle body [uT]	10.74	12.04	0.09	1.74

Figure 1.31: Table showing the influence of ferrite and aluminum on coil performance [13].

22

should reduce this risk even further, if necessary. FEM simulation can be used to get a sense of the magnetic field strength around the go-kart in all misalignment positions, before developing a system.

For dynamic charging there are two commonly known and used transmitter:

- Long-wire systems

- Lumped systems

The Long-wire –distributed– system consists of a large primary coil, that is able to transfer power to several secondary coils at the same time. The lumped system consists of multiple small primary coils transferring power when closely aligned [23]. In lumped systems similar detection systems as used in the static situation would be applied. Knowing the exact location of the go-kart can ensure that a transmitter is shielded by a go-kart when transferring power. Long-wire system used to be very ineffective and unsafe, as it is impossible to shield off the entire transmitter. However, track segmentation method could be applied to turn on and off different segments of the wire. This would make it a more viable candidate for the use in go-karts, as the system would behave like a lumped system and could therefore be fitted with the same detection systems; this will be further discussed in Section 1.5.

1.4.5 Possible future standards

Standards are of great importance for overall acceptance and the success of a product. Take conductive phone chargers for example; people can get so annoyed with being the only one with a specific charger, that they might change to a model with a standardized charger for their next phone. In the charging of electric vehicles, it is of importance that all vehicles equipped with a receiver are able to charge on parking spots or in front of traffic lights. A standard is this scenario would be useful to ensure that go-karts from different manufactures can be used on the same track, increasing the chances of large manufactures investing in the development of these go-karts. A few standard were examined to determine the possibility of a adopting an excising standard, which would simplify the standardization of the system.

In static wireless power transfer there are a few standards currently used [24]. One of these standards is the Qi standard, that is mainly used for mobile devices like phones [25]. This was initially designed for up to 5W of power, but is of course continuously improving. The standard A4WP, that is is more flexible in its misalignment but also has a lower power rating 10-22W [24], has merged with the Power Matter Alliance to form the Airfuel Alliance. Both of these standards, although broadly applied in wireless power transfer, do not satisfy the requirements for vehicle charging.

In wireless vehicle charging a new standard has been developed by SAE(Society of Automotive Engineers), namely the J2954 [26]. This standard has four different power rating classes, ranging form 3.7kVA to 22kVA, with 3 different ground clearance divisions. This regulates the required amount of distance that the ground unit should be able to transfer power across. Although it is always unknown which standard becomes a success in the market, the fact that this standard has been set by SAE makes it very likely to succeed. Moreover, this is the follow up standard from the conductive standard for electric vehicles; the J1772 standard, that is now widely used. Table 1.3 gives an overview of these different wireless charging standard. For the go-kart standard very different ground clearance and power levels are required compared to the J2954 standard, which means that a new standard would be required.

Table 1.3: Standards in wireless charging and their characteristics.

Standard	WPC QI	Airfuel Alliance	SAE J2954
Power-rating	15 W - 120 W	10 W - 23 W	3.7 kVA - 22 kVA
Power Frequency Band	87 to 205 kHz	6.78 MHz	81.38 kHz - 90 kHz
Maximum airgap	5 mm	50 mm	250 mm
Foreign Object Detection	yes	yes	yes

One could also argue that no standard is required as go-kart tracks are always bought with the receiver –go-karts–; which is the main difference between IPTS applied to public roads and go-kart tracks. However, as mentioned before the use of a standard could allow different manufactures

to produces their own go-karts for the system, providing the customer more freedom of choice and thereby make competition racing possible. Although a standard is not yet required in the feasibility study, it is important to consider as it plays a role in the applicability of go-karts with IPTS.

1.5 Dynamic wireless inductive charging

Using an IPTS to statically charge a go-kart has a lot of advantages compared to conductive charging. However, it does not reduce the required battery-pack size. In order to reduce the required battery-pack the go-karts will have to be charged on the road; dynamically. The sizing of the battery-pack will have a considerable impact in the total weight and thus power requirements [1], as it is a large contributor to the total weight of the go-kart. Even-though the initial investment of the roadbed coils is quite substantial, the reduction in battery-packs and the extended lifetime of these packs due to shallower discharging makes this system worth considering [27].

There are some differences between dynamic and static charging, but most statements done in Section 1.4 about the system are still valid. This section will therefore be focused on additional features required for dynamic charging.

1.5.1 Receiver coil

The pickup side of the system will be equal for both static and dynamic charging as this is fixed in the go-kart. As shown previously, the coil topologies that has the greatest allowance to misalignment are the DD-type coils. It shows significantly better tolerance to horizontal offset when compared to the circular topology from cluster 3 [28] [14] [23]. Considering that there is little difference between the scoring of the topologies in cluster 3, the significant tolerance improvement of DD topologies can be expected for the other topologies from cluster 3 as well. Like stated in the section on static charging, the required installation space and complexity of the topologies from cluster 2 make them less desirable in a go-kart application. And the topologies of cluster 4 are again rejected due to their added complexity and weight.

A DD topology from cluster 1 would thus be the most suitable choice. For these topologies enough installation space is present –twice the area used in the comparison of Figure 1.15– and they are least sensitive to misalignment. Within this cluster, the DDQ coils are the least sensitive to misalignment and would thus be preferred. However, the higher complexity of the DDQ and DD overlapped coils combined with the marginal improvement with respect to the DD coil, makes the DD coils the more suitable option for this feasibility study. For the final product a DDQ coil or a DD overlapped coil would be more suitable. As the topology performs well on a wide variety of transmitters [29] [28] [14], no distinction has to be made when selecting the transmitter coils or tracks.

1.5.2 Transmitter Tracks

The difference between the two most common types of transmitter tracks –lumped and long-wire– were briefly discussed in the precious section. In this section all tracks types are compared and discussed more thoroughly.

Long-wire tracks

Over the year several prototypes of long-wire loop tracks have been made and investigated. Figure 1.32 shows how the long-wire loop has developed over the years. The first types of track were just simple straight-line long-wire loops. As can be seen in Figure 1.32, two or four wires would span the total length of the track, embedded in concrete. Here a U-shaped or W-shaped core would guide the magnetic flux in all configurations, that were applied to decrease the magnetic resistance of the transmitter and thus increase the power transfer. These are shown in Figure 1.33 [30], where a cross section of both configurations is shown.

	1 G (Car)	2 G (Bus)	3 G (SUV)	3⁺ G (Bus)	3⁺G (Train)	4 G (Bus)
Date	Feb. 27, 2009	July 14, 2009	Aug. 14, 2009	Jan. 31, 2010	Mar. 9, 2010	2010~ (under development)
Vehicle						
System Spec.	air-gap= 1cm efficiency= 80%	air-gap= 17cm efficiency= 72%	air-gap= 17cm efficiency= 71%	air-gap= 20cm Efficiency=83%	air-gap= 12cm efficiency= 74%	air-gap= 20cm, efficiency= 80%
	All the efficiencies are measured by AC grid voltage to on-board battery terminals					
EMF	10mG	51mG	50mG	50mG	50mG	<10mG
Power Rail (width)	20cm	140cm	80cm	80cm	80cm	10cm
Pick-up						
Power	3kW / pick-up	6kW / pick-up	15kW / pick-up	15kW / pick-up	15kW / pick-up	25kW / pick-up
Weight (Pick-up)	20kg	80kg	110kg	110kg	110kg	80kg
Size	55x18x4 cm³	160x60x11 cm³	170x80x8 cm³	170x80x8 cm³	170x80x8 cm³	80x100x8 cm³

Figure 1.32: Overview of several IPTS on vehicles.

(a) U-shaped core for flux guidance.

(b) W-shaped core for flux guidance.
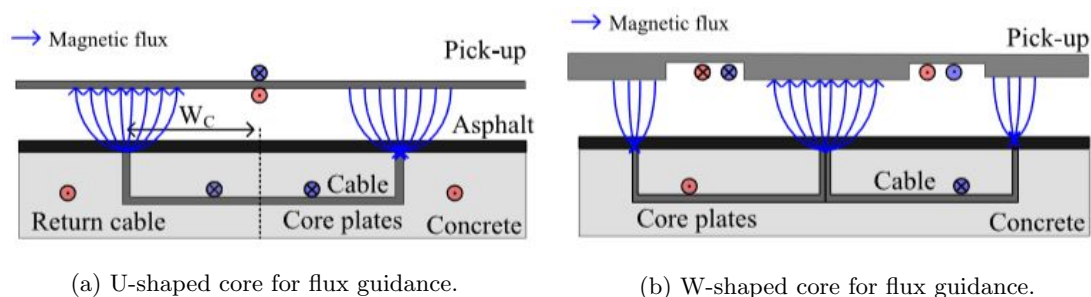
Figure 1.33: Cross-section of cores used in long-wire loops [30].

25

I-type tracks

The radiation in the vicinity of these tracks was still a problem due to the track-width and configuration. It was also very expensive to install due to its size, and due to these problems a more narrow-width track was required. The narrow-width single phase track design, that is shown in Figure 1.34, has a track-width of just 10cm. The wires create opposing magnetic poles in the I-shaped cores as the wires switch sides between poles. This reduces the radiation for pedestrians near the track significantly [29], as EMF cancellation occurs. It also increased the air-gap to 20cm, which is useful in car charging due to minimum road-clearance requirements set by governments.
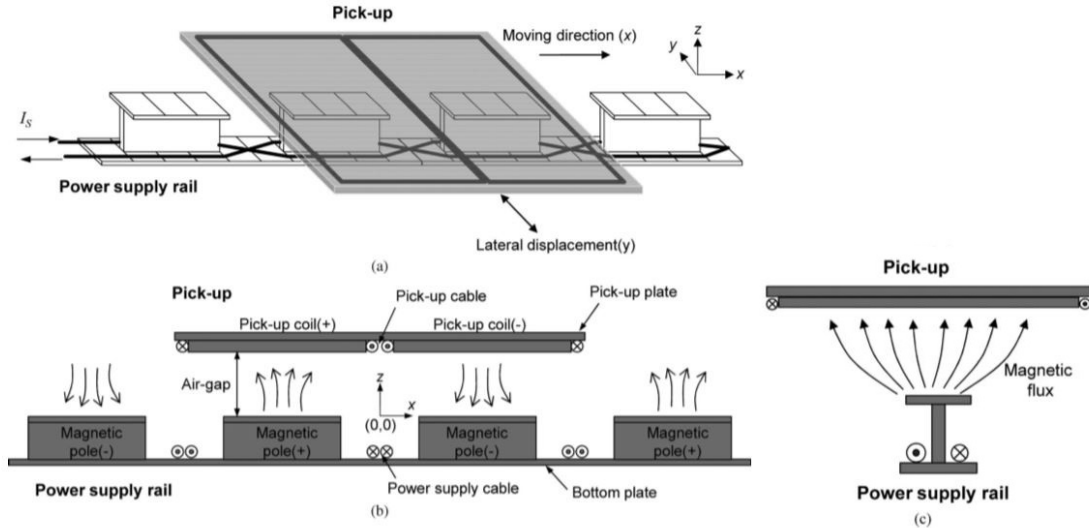
Figure 1.34: I-type single phase track [29].

I-type tracks with DQ-switching

The most significant drawback of this design, was that it had gaps in the power supply; the vehicle would move from one pole to the other, where the power would drop to 0 exactly between the two different poles due to EMF cancellation. To overcome this problem a new type of track was introduced: The I-shaped DQ wound track, were an extra set of poles and wires was added. The primary wires and secondary wires, respectively d-winding and q-winding, would be energized 90°out of phase. The difference in power supply for both types of track is shown in Figure 1.35. This methods resulted in a power-drop of merely 11% [31] between to poles, whereas the power used to drop 100%. This means that the power delivered to the pickup is much higher as it transfers power continuously instead of sinusoidal. The design of this transmitter is shown in figure 1.36.
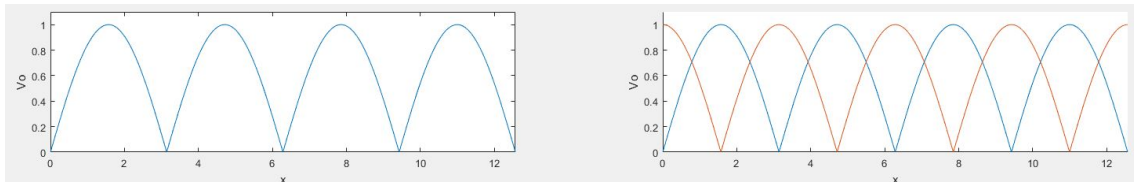
Figure 1.35: Induced Voltage in pick-up when moving over magnetic poles(single and dual phase).
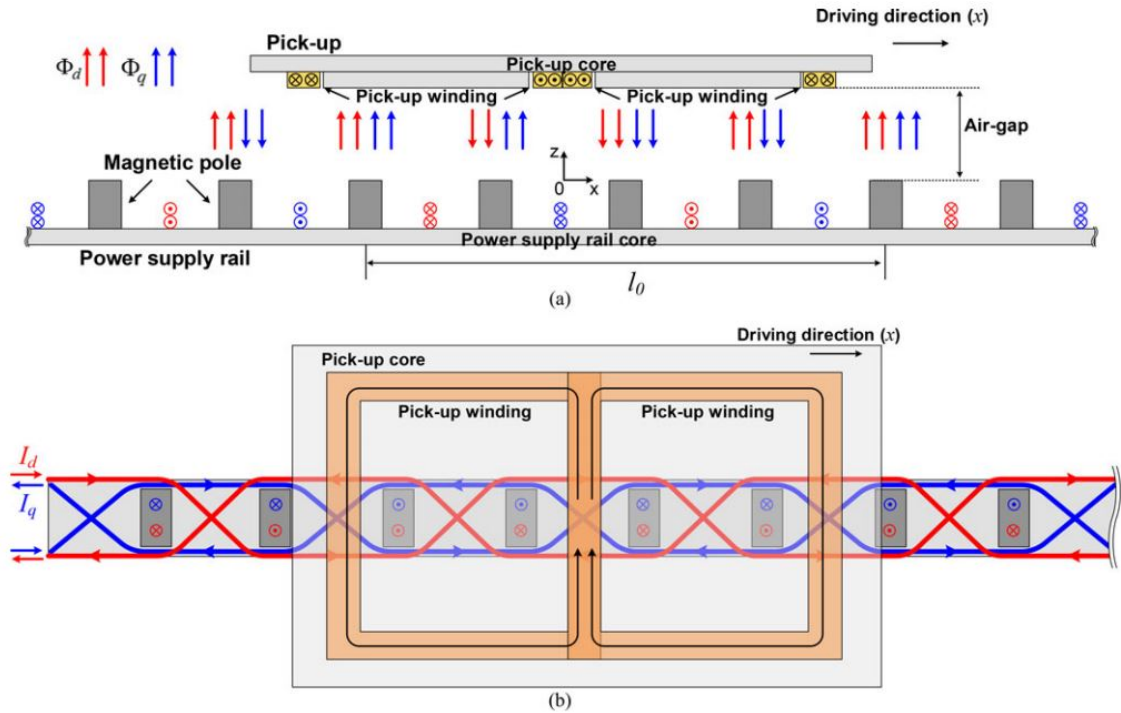
Figure 1.36: I-type dual phase track [31].

S-type tracks

To decrease the construction costs even further, an S-shaped and ultra slim power rail was constructed, that is shown in Figure 1.37. This track has a width of just 4cm, which is 6cm more narrow than the I-type track. This not only helps to reduce EMF in the surroundings, but also enhances the lateral tolerance for misalignment. Even though the efficiency of this track is slightly lower than the I-type dual phase, the reduced construction costs as well as the larger tolerance are advantages that are very important to ensure the success of IPTS.
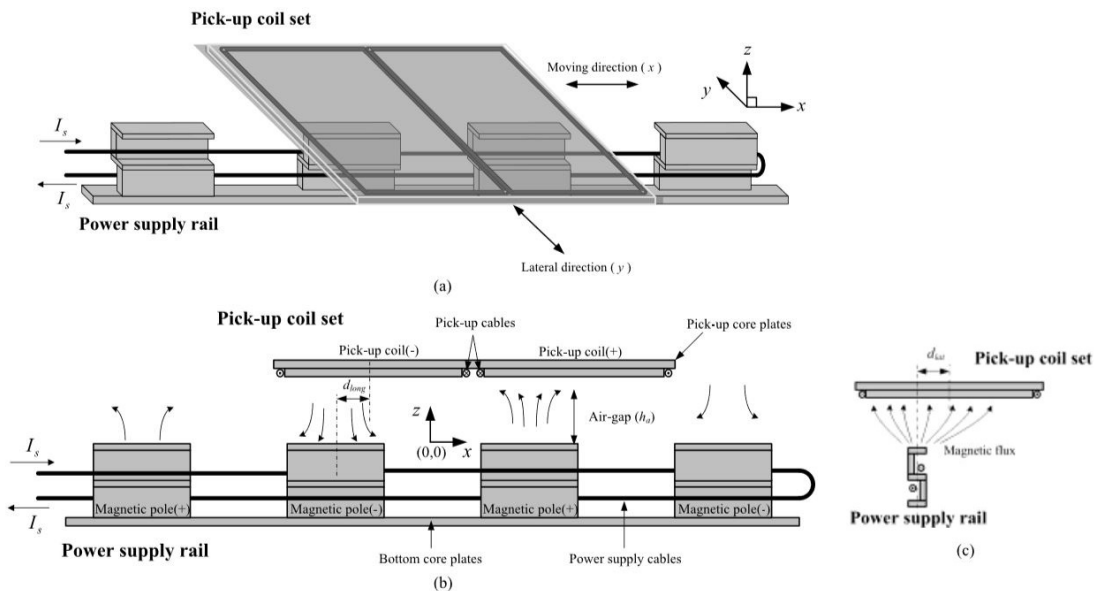
Figure 1.37: S-shape single phase track [32].

Lumped tracks

Another possibility in dynamic charging is a lumped system track, which are static charging coils placed after each other to provide power to the pick-up. The advantage of such system is that only the transmitter that is closed to the receiver has to be switched on. This reduces EMF in the vicinity and reduces losses in the transmitter. A prototype that was able to transfer 2.2 kW at an efficiency of 71% [33] is shown in Figure 1.38. Due to the lack of misalignment testing, the lateral tolerance of the ORNL system is unknown. However, as discussed in the previous section, circular coils have a smaller misalignment tolerance than the narrow-width tracks when using the same DD receiver.

Figure 1.38: ORNL spaced circular coils test setup [33].

Track segmentation

Track segmentation could ensure that the advantages of both systems can be utilized. A comparative study has shown that of the overall system, the efficiency of spaced loops is larger than long-wire loops [5], which is logical as only required sections are energized and no losses occur. However, using track segmentation this could be achieved in long-wire system as well. EMF near the track will be reduced when no receiver is covering the system and the system will be less subjected to power-line losses, due to the fact that the system is not continuously energized [34].

The possibility of charging several receivers on the same track will remain possible by switching on the required sections. This switching can be done in several ways, also shown in Figure 1.39 [35]:

- Centralized switching
- Distributed switching
- X-segmented switching

The fact that only one high frequency inverter is required in the use of long-wire loop systems is an advantage that has to be preserved. For both the centralized- and distributed switching, only one sub-rail can be activated at a time as the lines are simply connected or disconnected from the main via switches. This would be useless in go-kart systems as different parts of the track need to be energized at the same time. However, a solution to this problem is the X-segmented rail type, that enables multiple sub-rails to be energized at the same time [35]. Here auto-compensation boxes are used to switch current directions sets of cables, hereby mitigating its inductive capacity. This X-segmented switching also diminished the amount of wiring, creating a more economical system. It also meets the requirements from Section1.4.4, where it was concluded that segmentation is

(a) Centralized switching segmentation consists of a bundle of supply cables and a centralized switch box

(b) Distributed switching segmentation consists of a common supply cable and multiple switch boxes
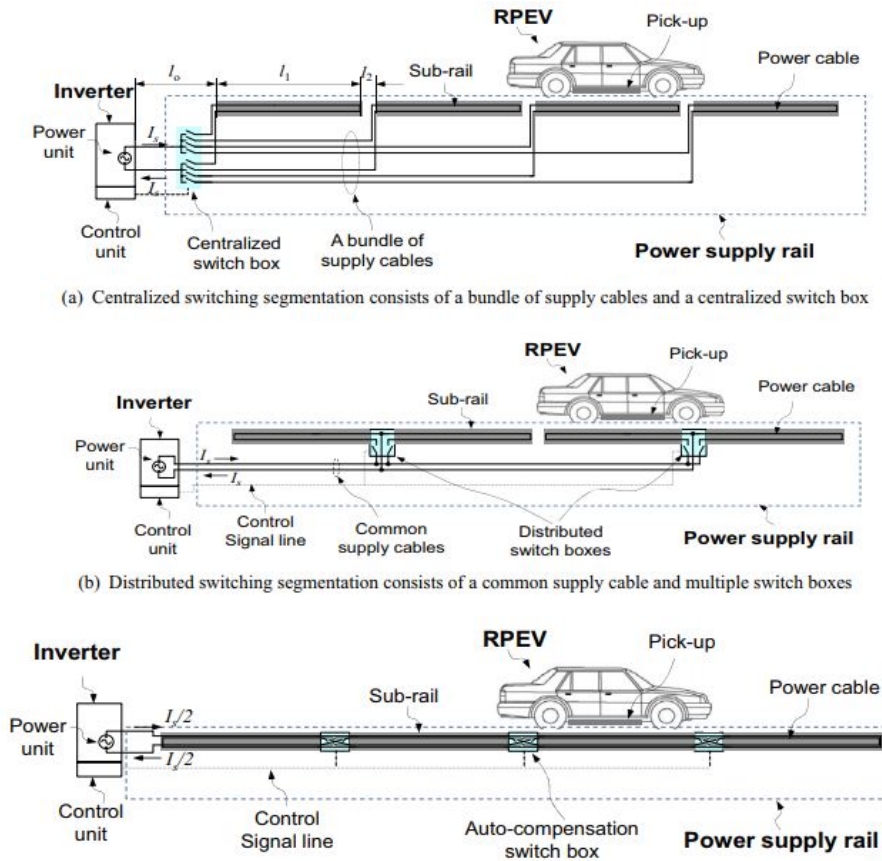
Figure 1.39: Different track segmentation possibilities [35].

required to keep the track safe. The extra components required to make this possible should be considered in the cost analysis.

Table 1.4 shows an overview with some important characteristics of the previously discussed tracks.

Table 1.4: Comparison of different transmitter tracks.

Track type	I-type [29] [31]	S-type [32]	ORNL spaced coils [33]
Airgap	20 cm	20 cm	15 cm
Lateral tolerance	24 cm	30 cm	unknown
Efficiency	74% at 27 kW	71% at 22 kW	71% at 2.2 kW
Rail width	10 cm	4 cm	40 cm

For the use in go-karting the most important aspects are a low EMF, high lateral tolerance and low construction costs. The S-type track is the best considering all these requirements. Moreover, it is simple and has a high efficiency which makes it a fair representation of what is possible with an IPTS; therefore, it is the optimal track for the use in a feasibility study for go-karting. The conclusions from Section 1.4 are still valid and should be considered together with this conclusion; as this section is merely an addition to the previously stated.

1.6 Conclusion

In this chapter the component selection for the feasibility testing of both static and dynamical charging was conducted. By first determining the different parameters that can be adjusted when designing an IPTS, and then comparing their functionality in a go-kart design, a selection of components was made that can be used to determine the feasibility of an IPTS on go-karts. Based on the literature that is reviewed, it can be concluded that he most practical approach in testing the feasibility is use topologies that are already well-documented and studied. These topologies provide the theoretical and practical framework that establishes the possibilities within current technology. For this purpose the design of the system will be as followed:

- **DD receiver coil**

- **DD stationary transmitter coil**

- **Ultra slim S-shaped power track**

- **Series-Series capacitor compensation topology**

- **Fixed frequency**

The DD coil transmitter and receiver provide a tolerance to misalignment, that will be very useful in both static- and dynamic charging. The chosen compensation method of Series-Series capacitors is recommended by literature for lithium-ion charging capacities. Several types of converters were discussed and the most suitable selected. The adding of shielding and flux guidance will have to be determined in a FEM program, as this will drastically improve the amount of power transferred by the system while keeping the magnetic field levels within the limits set by the ICNIRP. Sensors or camera's will have to ensure that power is only transferred from the primary coils, if a go-kart is covering the transmitting coil; in both static and dynamic conditions. A standard can be useful in development of this system, but is not of importance to the feasibility study. As current standards would not suffice, a new standard would have to be developed.

In further studies the system could be optimized, for which several suggestions have been made in this section, such as; the use of a DDQ coils, the decoupling of coils, and the optimization of the compensation topology by investigation of SPS topology. However, this does not fit within the scope of this research, that is merely to determine the theoretical feasibility of the system, and should therefore be left for future studies.

The proposed system is a solid foundation for all simulation purposes, without spending too much time in detailing the system. If the system is not feasible in this manner, the margins brought on by the detailing are small enough to assume that the system is not feasible. The feasibility study will thus not be focused on one of the many low level aspects of the system, but on the high level aspects of the system.

Chapter 2

Design of transmitter coils for go-kart ipts

2.1 Introduction

In order to determine the feasibility of the system, it must be determined what the power transfer capability of the system is within the boundaries of the system. It is known that tremendous amount of power can be transferred by Induction Power Transfer System (IPTS), but the system also has to be compact and light enough to be fitted in a go-kart. This should be done without radically redesigning the go-kart, as this makes the system less likely to be successful in the industry. Therefore, it is important to determine how much power an IPTS can transfer, while the size of the transmitter coils are restricted. In this chapter the boundaries for the coil design will be defined, and calculation methods explained. Then a method for optimizing the coil parameters is presented. In subsequent Chapters 3 and 4, safety, system performance, and cost will be analyzed.

In the previous chapter literature study has shown that for this study the most suitable setup would be a DD receiver coil combined with a S-shaped power track. Series-Series capacitor compensation will be used at a fixed frequency. All choices made for the setup were driven by the motivation to show what is possible with an IPTS, without needlessly making the system complex. Coil design is an iterative process in which the optimal setup depends on a great many of different factors. Therefore, it is needed to stress that this optimization does not produce the single most optimal setup for go-karts. As changes in design -such as track layout, size- or winding-ratio between receiver and transmitter- could enhance the suitability for certain tracks. It does however, provide a optimized solution for the feasibility testing of the system, within the set boundaries of this research.

As Chapter 1 has provided the most suitable setup for the feasibility study, the system design will be according to the conclusions of this chapter. Coil designs will then be compared and evaluated on the aspects weight, amount of copper used, and power output. The final section of this chapter will determine the performance of the final design when a misalignment is introduced.

2.2 System design

Design is an important part of the process of determining the feasibility of the system. The design for a go-kart IPTS is determined by the design of the IPTS, the electric motor, and the battery pack. To chose an optimal design first the requirements of the system have to be known; for a standard rental go-kart these are listed in Table 2.1.

Table 2.1: Design requirements of an IPTS for a go-kart.

Design requirements	Values
Output Power	6.3 kW
Nominal Input Voltage Engine	48 V
Outer Diameter of Receiving Coil	500 mm
Air-gap	60 mm

Designing an IPTS is a complex task as there are many parameters to establish. The iterative process can become complex, and long without the proper boundaries as most of these parameters influence each-other; therefore, it is important to gather all the limitations of the system and thus define as many parameters as possible.

Having established the requirements and assumptions of the system, the flowchart for Figure 2.1 guides the study. The first step in design process is to determine all the possible geometries of the coils. In this case the available space beneath a go-kart acts as a limit on the designs outer dimensions. The inner dimension of the coil are determined from the required misalignment tolerance [32] [36]. The number of turns can be used to determine the mutual inductance.
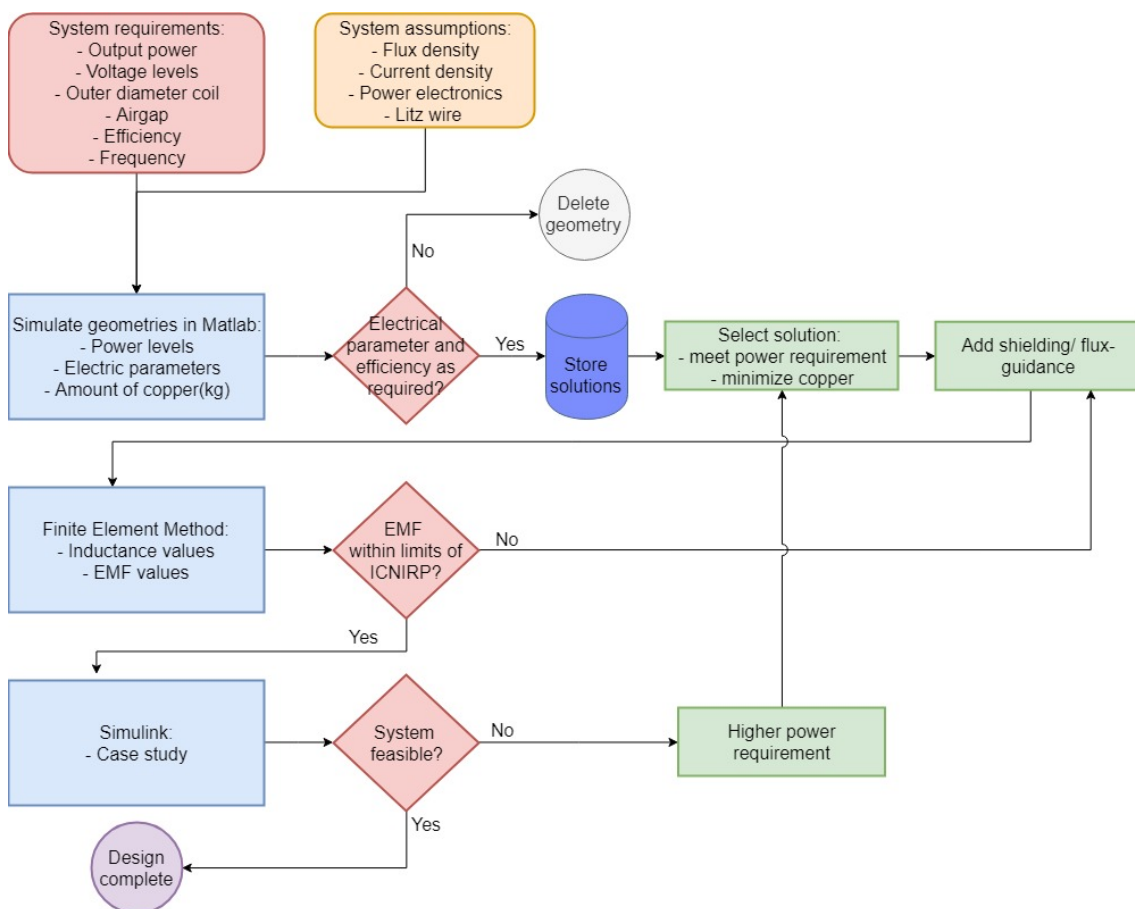

Figure 2.1: Design flowchart for the IPTS.

Once the possible geometries have been calculated, a comparison should be done that compares all solutions to determine that can transfer the required power levels. Shielding and flux guidance

is assumed to be equal in all these solutions. Shielding and guidance will then be added in a Finite Element Method (FEM) program until the required Electromagnetic Field (EMF) levels are met, to determine how the system can be implemented safely.

Finally, a case-study should determine whether the system is able to transfer the required power. A simple circuit with charging areas in the track will be simulated. The State of Charge (SOC) of the battery then indicates the feasibility of the system. If not, a higher power requirement should be set and the FEM and case study should be repeated.

Electric motor design

An important part of the design is the electric motor that will drive the go-kart, as this will determine the required battery voltage and the needed motor controller. The first step is to determine what type of motor to use. In current EVs manufacturers are quite conservative in their choice of motor as most of them are either Permanent Magnet (PM), Induction Motor (IM) or Direct Current (DC) motors. However, there are more suitable options like Reluctance Motor (RM), Synchronous Brushed Motor (SBM) and Permanent Magnet (PM) motors. Figure 2.2 [37] gives a rough indication of efficiency ranging from 1 to 5 of several electric motors. This is such a simple figure as it is to be used to get an indication of efficiency only. For more detailed analysis every electric motor should be studied individually.

However, as this would drive our research into the detailing of low-level systems, for now an AC motor(IM) was selected. As AC is the most widely available option, that performs almost as well as RM, this was selected for the further analysis. For future research, however, it would be worth considering the RM option as it seems to provide some additional benefits.

	Motor	Electronics	System
SPM	5	4	4
SBM	4	4	4
RM	4	3.5	3
IM	3.5	4	3
DC	2	5	2

Figure 2.2: Efficiency comparison of several motors for use in EVs [37].

Battery design

As it is important to keep losses as low as possible and wires thin, a high voltage will be selected in correspondence with the electric motor. This can be achieved by connecting several batteries in series, hereby adding their voltages as shown in Figure 2.3. To ensure a long lifetime of these batteries a Battery Management System (BMS) should be implemented to ensure that all batteries remain equally charged.

The battery pack will be comprised of lithium-ion batteries due to their low weight. This does require the system to be able to acts as both a voltage-source and current-source; this will have to be considered when the compensation method is chosen.

Figure 2.3: Batteries connected in series to enhance the voltage level [38].
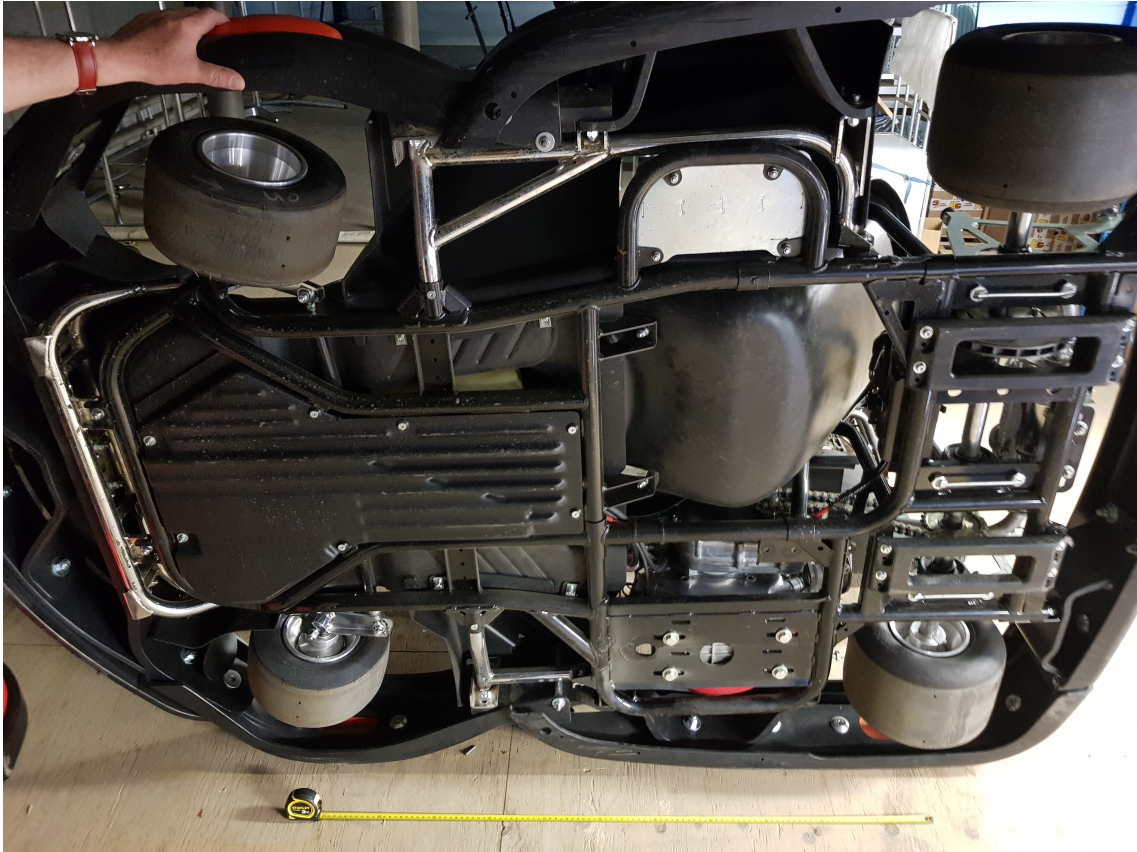
Figure 2.4: Bottom of rental go-kart.

2.3 Boundaries in transmitter coils design

Setting the boundaries of the system is of crucial importance in designing the system. Without these boundaries the amount of possibilities is tremendous and the determination of the feasibility would become a long process, as there are so many possible ways to setup a IPTS. In this section boundaries of the system are set, and supportive argumentation is given.

2.3.1 Geometrical boundaries

The first boundaries that need to be determined are the geometrical sizes of the receiving coil. These boundaries are mostly determined by the sizing of current go-karts and are ,therefore, relatively easy to establish. From these boundaries the primary receiver boundaries will be determined.

Receiver boundaries

The restrictive factors for the design are the following:

- Height of the receiver-pack
- Outer receiver-pack dimensions
- Coil width

Firstly, the maximum installation area of the receiver on a rental go-kart is determined. Figure 2.4 shows the outer installation dimensions of the receiver is defined by the frame of the go-kart. The width of the receiver needs to fit between the wheels and is set at 600 mm. The length of the receiver can be up to 1200 mm. The receiver should be fitted within these dimensions and the coils themselves will ,therefore, be marginally smaller.

Secondly, the maximum height of the receiver is determined. Due to the lack of suspension in go-karts, the height between the bottom of the go-kart and the track can be assumed fixed. The only variations in this distance are due to the deflection of the frame, deflection of the tires, and

Figure 2.5: Height of rental go-kart and plastic buffers.

the curvature of the road. As can be seen from Figure 2.5, the normal height is around 60 mm. However, plastic buffers are already installed on the bottom to prevent damaging the frame; that can be seen in Figure 2.4. These are 30 mm in height and this will be used as a limit on the height of the receiver; as this will not influence the riding height and plastic buffers can be used to protect the system from impacts. The total receiver pack is made up out of an aluminum shield, ferrite bars, the coils themselves, and a plastic cover. The total allowable height of the receiver -30 mm- needs to be divided over these components; therefore, the maximum thickness of the coils is set at 10 mm.

The last parameter that needs to be determined is the maximum coil width; that is set at 50 mm. If the coil is set to span the maximum 600 mm width of the shield, this width would have a lateral tolerance of 250 mm. The wider the coils are the smaller this lateral tolerance becomes, as can be seen from equation (2.1).

$$d_{lateral} \cong \frac{W_{receiver}}{2} - \frac{W_{coil}}{2} \tag{2.1}$$

Another reason to keep this width below 50 mm is that the area of both sending and transmitting coils is a determining factor in the mutual coupling; as shown in equations (1.2) and (1.3). The area enclosed by both coil is assumed to be remain equal to simplify calculations and should not be altered greatly for the assumption to hold, as explained in the mutual coupling calculation of the previous chapter. Because both coil are determined to have the same number of turns, it must be concluded that the maximum width should be similar as well.

Transmitter boundaries

The are two important restrictive factors in the transmitters:

- Transmitter width
- Installation cost

35
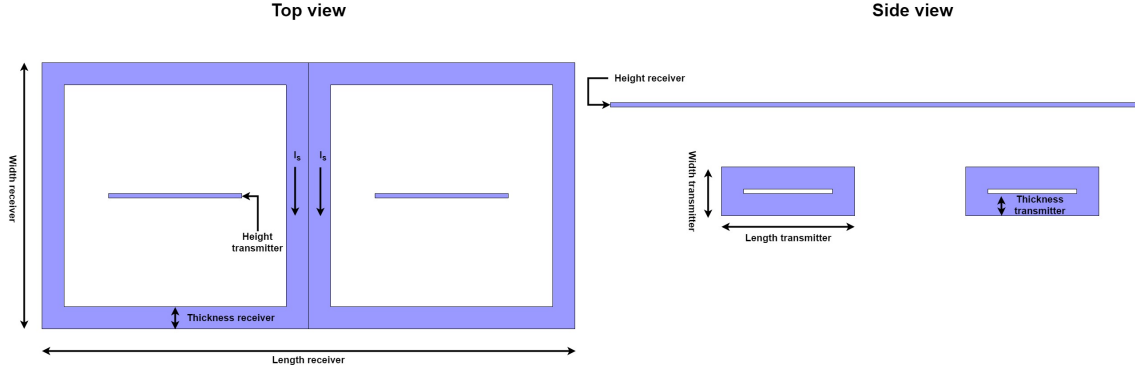
Figure 2.6: Maximum geometry of coils.

The transmitter width needs to be as small as possible, as this leads to a better tolerance to lateral misalignment. If a transmitter is too wide the coupling might be good in perfect alignment but will soon drop –compared to a narrow receiver– as a greater percentage of the flux will leak beyond the coverage of the receiver in similar cases of misalignment. However, the effective area should remain large enough as power transfer will decrease if this is minimized too much. Known systems can transfer up to 22 kW [32] ,therefore, the dimensions of this system will be taken as boundaries of the transmitter-pack. A S-shape design is used as it has provides a good coupling [39] and allows for the transmitter-coils to be placed sideways; making the charger as narrow as possible.

The requirement of a narrow transmitter also positively influences the second boundary: installation cost. Installation cost determines the feasibility of the system in the way that it can make the system non-competitive with respect to other systems. To keep cost low, installation should possible in excising tracks without having to redo the complete road surface [29]. In optimizing the system the required amount of ferrite will be re-examined and adjusted accordingly; hereby, further reducing the width and cost while making installation easier.

Table 2.2: Geometrical dimensions of transmitters.

Geometrical maximum	DD receiver	Transmitter
Length coil	1200 mm	300 mm
Width coil	600 mm	110 mm
Height coil	10 mm	10 mm
Thickness coil	50 mm	50 mm

The maximum geometrical dimensions of coils are documented in Table 2.2 and shown in Figure 2.6. These dimensions are based on the maximum installation size of the receiver and the known optimal distance between the transmitters [32]. The chosen DD topology requires two equally sized coils to be placed in the available space. For the receiver a 10 mm strip is left empty on all outer-sides of the coil, to be able to install a shielding rim. This will be further discussed in Chapter 3. The receiver also constraints the transmitter as the center of the poles are required to line up with the centers of the transmitter for good coupling.

2.3.2 Electrical boundaries

Boundaries in the electrical domain are based on the materials and components that are used in the system. The two most important electrical boundaries, both limited by the converters, are the following:

- Frequency
- Current

Frequency

There are three reason for using the 20 kHz as set frequency of the system. The first and most prominent reason is that it is used in the study that was the inspiration of the transmitter design.

This might seem arbitrary, but as it is a proven system it can be assumed that all components work in practice; this is an important assumption made in this study.

The second reason is that it is just above the hearing range of most people; therefore, no noticeable noise is produced by the system.

The third reason is that the skin-depth is reduced as the frequency gets higher. A higher frequency would require smaller Litz-wire, that is more expensive; therefore, it would make the system more expensive.

The final reason would be to reduce the losses in the ferrite. Figure 2.7 shows that frequencies in similar magnetic fields have a substantially higher power loss. Increasing the frequency further beyond what is necessary will increase the losses in the system. Keeping all these requirements in mind, the frequency was set at 20 kHz.
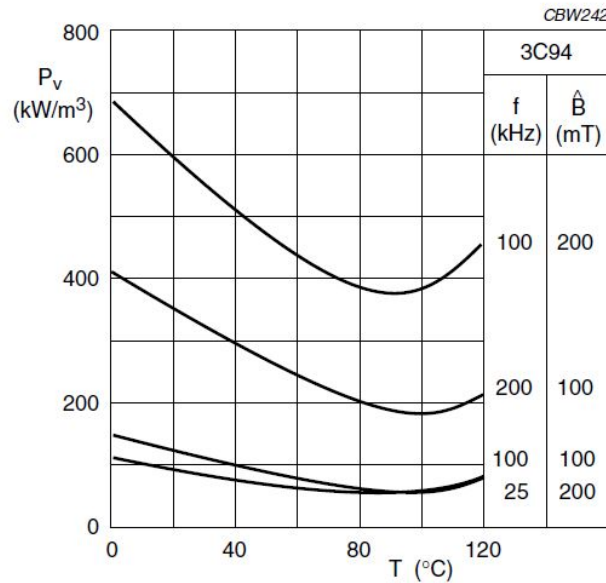

Figure 2.7: Specific Power loss in 3C94 as a function of temperature at several frequencies [40].

Current

The current is limited indirectly by the geometry of the coils and rating of the converters as both need to be capable of handling the currents running in the system. The current determines the current density and thereby the minimal wire-radius of the Litz-wire. For this study a current density of 5 $\frac{A}{m^2}$ was chosen as this will not require addition cooling of the coils; as the energy can be dissipated by the coils themselves.

The current setting at the input was required to be able to send around 25 kW to the receiver. The losses in the power-lines are required to remain small and therefore a high voltage of 500 V was chosen. This high voltage also ensures that the wires remain flexible, which is necessary for the placement of the transmitters. However, as will be shown later in this study 50 A saturated the ferrite and thus the current was lowered to 40 A, which is just below saturation level in perfect alignment. This is also in line with the setup on which the transmitters were based.

2.3.3 Magnetic boundaries

The boundaries of the magnetic field are determined by the materials used and the International Commission on Non-Ionizing Radiation Protection (ICNIRP) guidelines. Saturation in ferrite occurs beyond peak flux density levels of around 0.3 T, as shown in Figure 2.8; therefore, this is the maximum value in the ferrite. Public exposure limitations at this frequency are set by the ICNIRP at 2.7×10^{-5} T in air. Both will be discussed further in chapter 3.
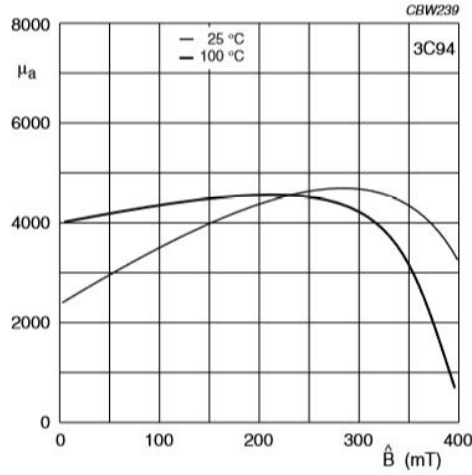
Figure 2.8: H-B graph of 3C94 ferrite.

2.4 Power transfer calculation for aligned coils

In order to calculate the power transferred between coils several parameters need to be determined, for which the appropriate formulas needs to be derived. The required formulas depend on the type of compensation topology that is used. In Chapter 1 an overview of several compensation topologies was provided and the most suitable compensation topology for this feasibility test was determined to be a Series-Series compensation topology.
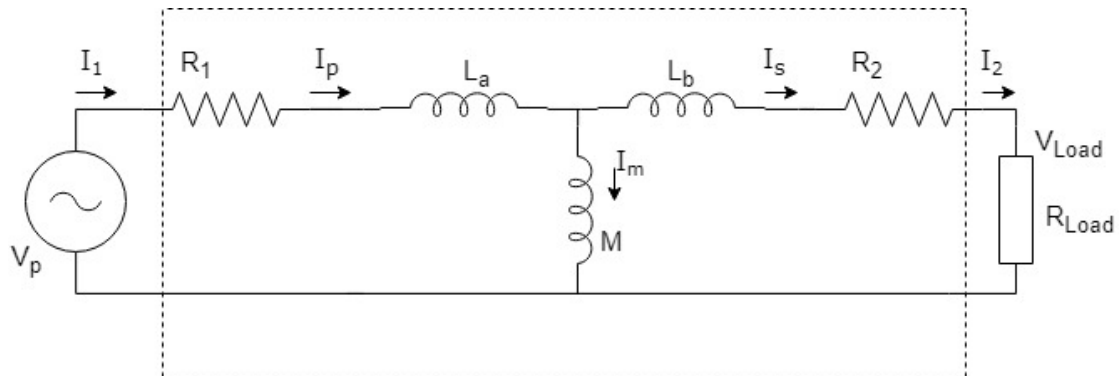
Figure 2.9: Series-Series compensated IPTS.

The simplified electrical schematics of a Series-Series compensated circuit is given in Figure 2.9. This simplified circuit requires the number of receiver- and transmitter-windings to be equal [3]. This was therefore assumed in all further calculations.
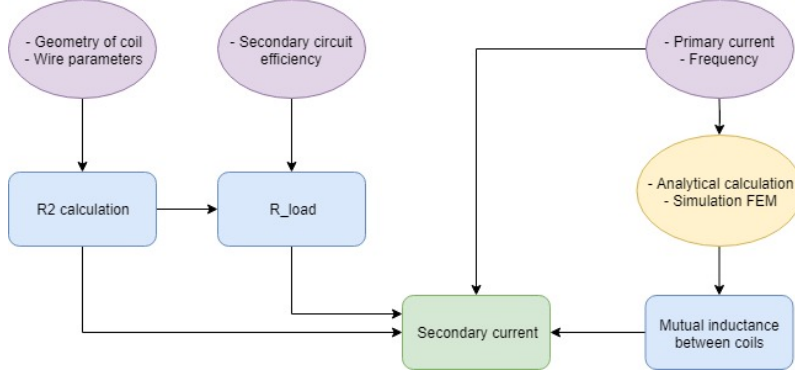
Figure 2.10: Flowchart current calculation fully compensated IPTS.

In order to calculate the power levels in the different parts of the system, all current levels need to be known. The primary current(I_p) is already known as it is set by the converter at the primary side. However, the secondary current(I_s) or induced current still needs to be calculated. Following sections will derive the required formulas and show how to simplify these calculations. The flowchart of figure 2.10 can be used to clarify the different steps in the calculation of this aligned case.

2.4.1 Secondary current calculation

The general expression for the current induced in the secondary coil –at fixed operating frequency– is dependent on primary current, the mutual coupling, and the impedance of the secondary circuit; as shown in equation (2.2) [17].

$$I_s = \frac{j\omega M I_p}{Z_s} \tag{2.2}$$

The secondary circuit impedance(Z_s) is the complex resistance of the secondary circuit. In the case of series-compensation all components of the secondary circuit are in series and their complex resistance can thus simply be added, as shown in equation (2.3).

$$Z_s = j\omega L_1 + \frac{1}{j\omega C_s} + R_2 + R_{load} \tag{2.3}$$

Rewriting equation (2.2) with Z_s from equation (2.3), gives equation (2.4).

$$I_s = \frac{j\omega M I_p}{j\omega L_1 + \frac{1}{j\omega C_s} + R_2 + R_{load}} \tag{2.4}$$

Assuming resonance –the design goal for an aligned IPTS– the equation for calculating the secondary current from the primary current can be simplified to equation (2.5). This is due to the fact that in this tuned setting the capacitor and inductor(the coil) cancel each-other out in this equation, as was intended in the design process.

$$I_{s-aligned} = \frac{j\omega M I_p}{R_2 + R_{load}} \tag{2.5}$$

I_p and ω are set by the converter and can thus be adjusted were necessary. In order to calculate the secondary current(I_s) the secondary resistance(R_s), the load resistance(R_{load}), and the mutual coupling between primary and secondary coils(M) needs to be determined.

Resistances in the circuit
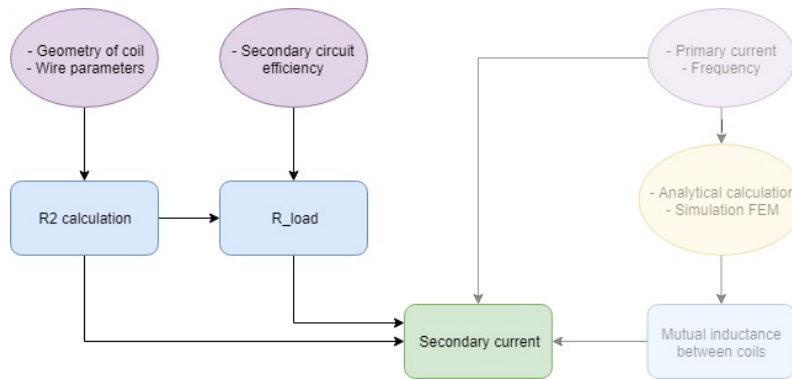
Figure 2.11: Flowchart resistance calculation.

In order to determine the resistance of a coil the cross-sectional area of copper is required, along with the total length of the coil, and several parameters. These parameters are determined by the type of copper that is used to construct the coils and given in Table 2.3.

Table 2.3: Parameters of coil.

Parameter	Value	Unit
Electrical resistivity copper (ρ)	$1.68 * 10^{-8}$	$[\Omega * m]$
Magnetic permeability of free space (μ_0)	$4\pi * 10^{-7}$	$[H * m^{-1}]$
Relative magnetic permeability copper (μ_r)	0.999994	$[-]$
Filling factor (K_f)	0.4	$[-]$

Figure 2.12 shows the schematic cross-section of a coil. In this figure the filling factor K_f becomes tangible, as the insulation between all strands and windings are shown to require a substantial amount of spacing. The copper area, number of windings, and number of strands can be determined from the predefined geometrical constraints and the filling factor. The length of the coils is determined by the average length of the coil multiplied by the number of turns, which is accurate enough for the feasibility study.
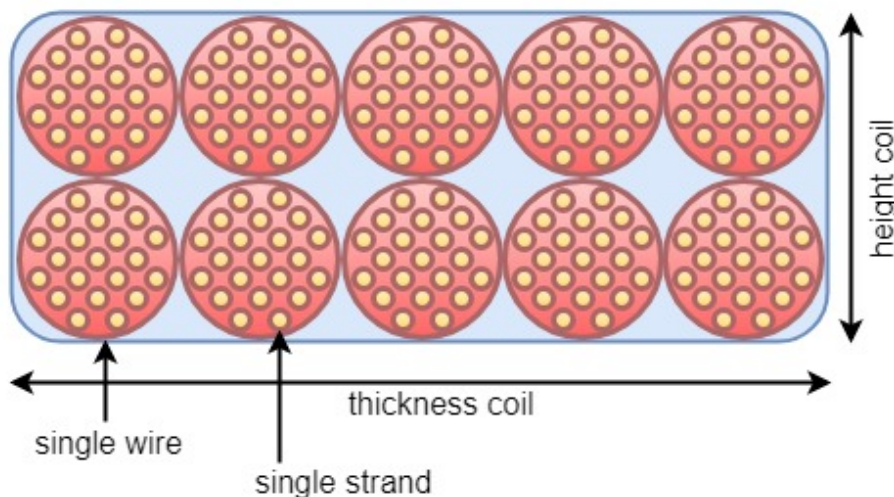

Figure 2.12: Cross-section of coil with Litz-wire.

The alternating current causes the skin-effect and the proximity-effect to occur; which were discussed in chapter 1. These effects occur at winding-, bundle-, and strand-level and should be minimized in all situations. At bundle level the proximity effect can be mitigated by simply

twisting the windings, whereas for skin-effect a more complex winding pattern has to be applied to minimize its effects [9]. For strand level several different approaches to dealing with these effects with the use of Litz-wire are shown [41] [42], but the most used methods is to chose a strand-radius which is much smaller than the skin-depth. The skin-depth(δ) is calculated by equation (2.6) and in further calculations a strand-radius of 1/3 of the skin-depth was assumed.

$$\delta = \sqrt{\frac{\rho}{\pi * \mu * \mu_0 * f}} \tag{2.6}$$

The resistance of a round conductor can be calculated by equations (2.7) [43]. This equation is constructed by determining the inner radius of a annulus with the same outer radius as the round conductor. This annulus would hold the same total current density, but this would be distributed equally over the entire surface. By setting the strand-radius very small and applying the requirement of complex windings, this formula can be used to determine the resistance of each individual strand.

$$R_{ac-round} = \frac{\rho * l}{\pi * \delta * (1 - e^{\frac{-r}{\delta}})) * (2 * r - \delta * (1 - e^{\frac{-r}{\delta}})} \tag{2.7}$$

The Alternating Current (AC) resistance of both coils is calculated by equation (2.8). Where r represents the radius of the individual strands within the winding and δ represents the skin-depth. It is important to notice that the strands within a single turn/winding are connected in parallel, whereas the turns/windings themselves are connected in series. The total resistance of the secondary coil also depends on the amount of coils, which for this design is two –both D's–. If the design would be expanded with subsequent coils, than these would have to be taken into consideration. Analytic resistance calculations are available as well [44], but these are too complex for a feasibility study.

$$R_{ac-coil} = \frac{N_{turns} * \rho * l}{N_{strands} * (\pi * \delta * (1 - e^{\frac{-r}{\delta}})) * (2 * r - \delta * (1 - e^{\frac{-r}{\delta}}))} \tag{2.8}$$

Once R_2 is known, R_{load} can be determined by setting the required efficiency at a desired value as shown in equation (2.9). This can be determined from the P_{load} as well, but a sweep will be used in this study to determine all possible variations of P_{load}; therefore, the secondary efficiency can be used to determine the secondary current. The resistance of the load can be determined actively with the help of a DC-DC converters, that will be used in the misaligned cases to keep coupling as high as possible.

$$R_{load} = \frac{\eta_{required}}{1 - \eta_{required}} * R_2 \tag{2.9}$$

Mutual coupling analysis
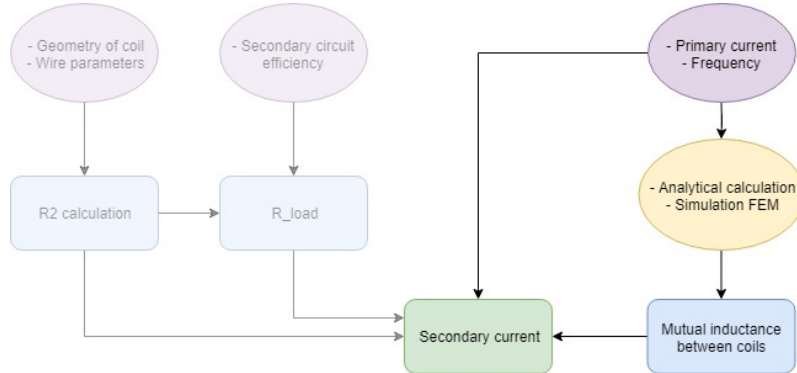
Figure 2.13: Flowchart Mutual inductance calculation

The last parameter required to calculate the induced current(I_s) is the mutual coupling between the coils, that can be acquired through FEM analysis in COMSOL. However, calculating the mutual

inductance for all different possible designs takes a very long time; therefor, three assumptions were made:

- Mutual coupling not effected by geometry differences
- Mutual coupling scales according to quadratic equation (2.10)
- Round Litz-wire

$$\frac{M_{new}}{M_{old}} = (\frac{N_{new}}{N_{old}})^2 \tag{2.10}$$

This allows an average value of the mutual inductance to be determined, that can then be scaled according to the number of turns; and used in calculation of power levels. The average values of the design can be used to calculate this mutual inductance.

2.4.2   Optimizing coil parameters for aligned system

The calculation from the previous section can then be used to determine the optimal coil parameters for this system. The flowchart from Figure 2.1 shows a step-by-step approach for the design of the coils. The Matlab script –found in Appendix A.1– determines all possible solution within the boundaries of the system. In this script boundaries can be adjusted and undesirable solutions will be disregarded. For the calculation of the different power-levels the secondary efficiency is swept from 0.6 up to 0.999. For each power-level the optimal design is chosen. All solutions that meet the requirement of the design are then compared to each-other. First, all input settings are defined, after which the comparison of all solutions is done. The mutual inductance of the system is estimated by scaling the mutual coupling of the average design to the number of windings for the simulation.

Mutual inductance average design determination

To determine the mutual coupling of the average design, it must first be known what the maximum design is. As the number of turns are set to be equal, the primary side can be used to determine the maximum number of windings. Equation (2.11) uses the maximum current density -5 A/mm²- and the maximum geometry of the primary coil to determine the maximum number of turns.

$$N_{max} \leq 5 * 10^6(\frac{w_{coil}h_{coil}K_f}{I_p}) \tag{2.11}$$

The average cross-sectional area of the coil is 250 mm². The assumption of round Litz-wire sets the maximum number of windings in the in the primary coil at 10; therefore, the secondary average is also 10 windings. There are two possible ways to define this area on either side given this assumption; therefore, all four possibilities were simulated. The lowest values is then used to determine the average mutual coupling. The values of the average coil designs are shown in Table 2.4.

Table 2.4: Parameters cross-section averaged coil designs.

Receiver		Transmitter		Mutual coupling [H]
h = 10 mm	w = 25 mm	h = 10 mm	w = 25 mm	3.6936e-5
h = 10 mm	w = 25 mm	h = 5 mm	w = 50 mm	3.7395e-5
h = 5 mm	w = 50 mm	h = 10 mm	w = 25 mm	4.0218e-5
h = 5 mm	w = 50 mm	h = 5 mm	w = 50 mm	4.0680e-5

The smallest mutual inductance for these averaged values is 36.936×10^{-6} H, when excited by 40 A running through two aligned primary coils. As worst-case scenario is assumed, this values is used in the optimization of the coil parameters.

Current settings

The maximum allowable current density in conductor without active cooling is $5 \frac{A}{mm^2}$, as higher current density would lead to heating of those conductors and thereby extra losses. Considering the average geometry and maximum current density, the primary current can be set up to 50 A. However, this results in saturation of the ferrite in the aligned position as can be seen in Figure 2.14. Therefore, the primary current(I_p) was set at 40 A for all calculations.
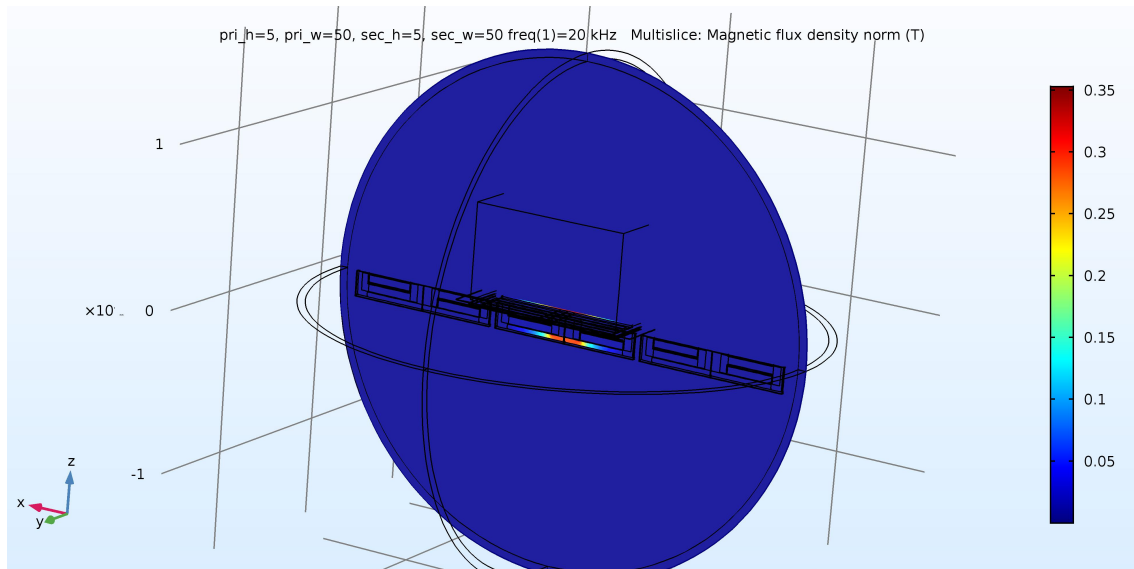
Figure 2.14: Saturation of ferrite I_p=50A.

Figure 2.15 is shown below to clarify how the setup is positioned relative to the go-kart, as the COMSOL model is quite abstract. In this figure a side-view is shown and the driver-box positioning becomes clear, that will be discussed further in Chapter 3. However, it must be kept in mind that this figure is not scaled properly, as its only purpose is to clarify.
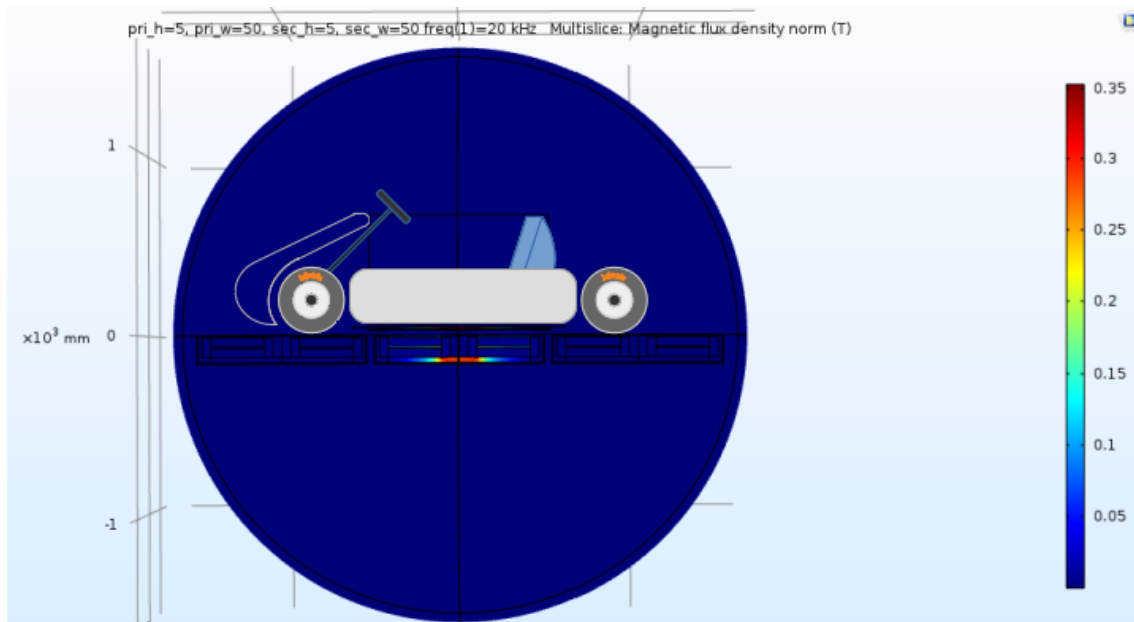
Figure 2.15: Go-kart positioning on COMSOL model.

Possible winding setups

The next step, after setting the initial parameters of the input, is to determine the possible winding setups. For practical purposes the assumption is made that the smallest variation within windings is one millimeter. This is based on the fact that the smallest Litz-wire found –without insulation– is only a quarter of this. Also positioning within the tolerance of a millimeter is already very difficult without special machinery.

The second assumption –already made previously– is the use of round litz-wire. This assumption is made to ensure quick computation and easy cancellation of skin-effect and proximity-effect. As the input current was set at 40 A this would require the windings to be 5 mm in length and width. Figure 2.16 shows how the parameters are used to determined the possible winding geometries.
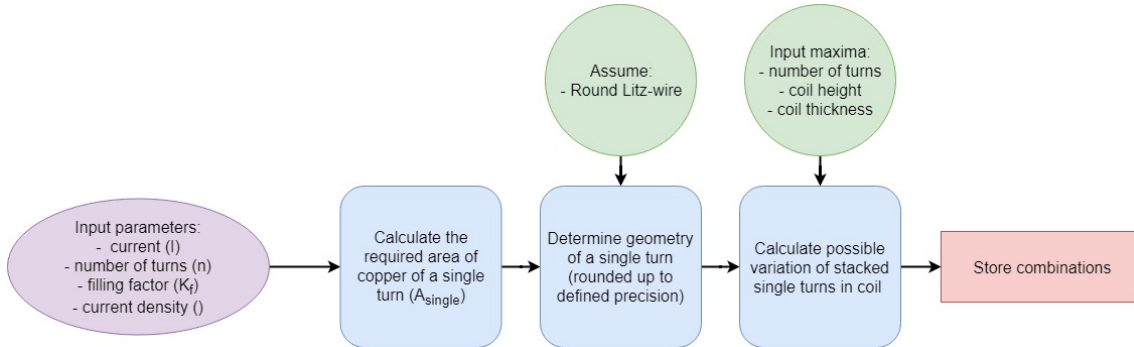

Figure 2.16: Possible coil setup determination.

A Matlab script –Appendix A.2– was used to calculate all possible combinations of width and height for each number of turns of the primary side, that meet the maximum allowable current density restriction. The reduced number of possible setups reduces the computational time drastically.

For the determination of the secondary windings a different approach was chosen; all possible size combinations were selected and tested. However, the assumptions made for the geometry of the Litz-wire are still valid, although several windings may need to be connected in parallel to ensure current density is not exceeded.

Secondary efficiency

The secondary efficiency can be defined in steady state by changing the load resistance(R_{load}), as seen in equation (2.9). However, in dynamic charging this same load resistance is used to control the current in the secondary circuit at the loss of efficiency. Therefore, in the aligned system the efficiency of the secondary circuit is kept as high as possible –between 90 and 99.9%–.

Power calculation of all setups

For the calculation of the final design the total amount of copper was minimized, as this is an important aspect of total cost. The ratio of transmitters and receivers was set to 50:1. The Matlab script incorporates this ratio in the calculations as a smaller track has a smaller ratio than a larger track and could therefore require a different setup.

Table 2.5: Input setting of Matlab optimization.

Parameter	Value
Maximum allowable current density (J)	$5\ [\frac{A}{mm^2}]$
Primary current (I_p)	40 [A]
Range of windings (N)	1:1:20
Range of secondary efficiency (η_s)	0.9:0.001:0.999

All these input settings of the Matlab script are shown in Table 2.5. The script then runs a script –Appendix A.3– for all input values, that returned the power transferred, copper used, and

total efficiency of the system. The solutions which were feasible then were stored for comparison.

The most important criteria are the power transferable and the amount of copper used, as these factors could seriously impact the result of the study. Therefore, the script from Appendix A1.1 was used to determine the minimum required amount of copper for each power level in Figure 2.17.
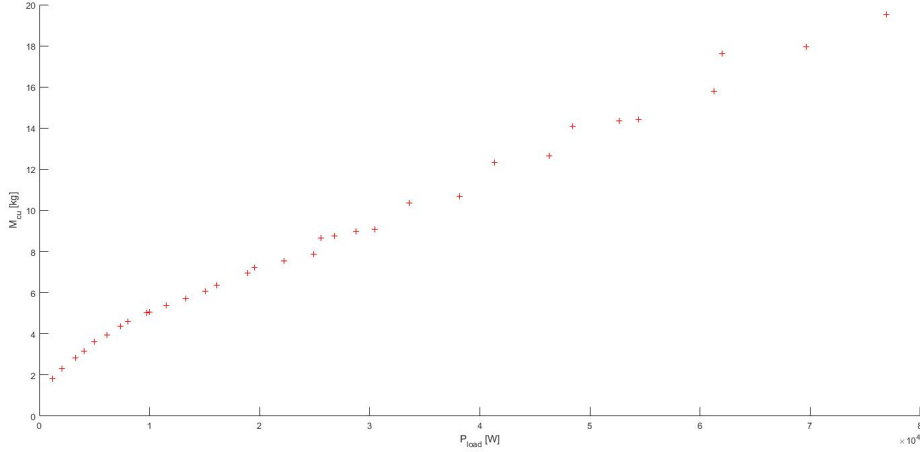

Figure 2.17: Minimal copper required per kW of P_{load}.

The IPTS should provide both the battery and the electric motor with power on the charging sections. On these sections the battery needs to accumulate the power needed for the track sections without a charger. The electric motor can draw up to 11 kW of power, but this will not be done continuously on the track. As the charging sections are relatively short –about 25% of the track for the case-study– a power transfer of 23 kW was selected, that will be used in the case-study of Chapter 4. The parameters of both coils are shown in Table 2.6.

Table 2.6: Final design geometry of transmitter coils.

Dimension	Transmitter	Receiver
Height	10 mm	10 mm
Width	25 mm	50 mm
Number of turns	12	12

2.4.3   Verification of models and assumptions

The calculations from this chapter were based on some assumptions and FEM results. In order to ensure that these result are accurate some verification was performed. The two most important verification are discussed here.

Verification of assumed mutual inductance

For all calculations the mutual coupling was assumed to be a quadratic function of the number of turns(2.10). The mutual coupling of the average sized coils was scaled to determine all mutual coupling values. After optimization the final designs were simulated in COMSOL to validate this assumption. Assumed and simulated values are shown in Figure 2.18 as a function of the number of turns. The difference between the calculated and simulated inductance's are around the same as the variations between the averaged designs; therefore, the assumption is valid within reasonable variance.
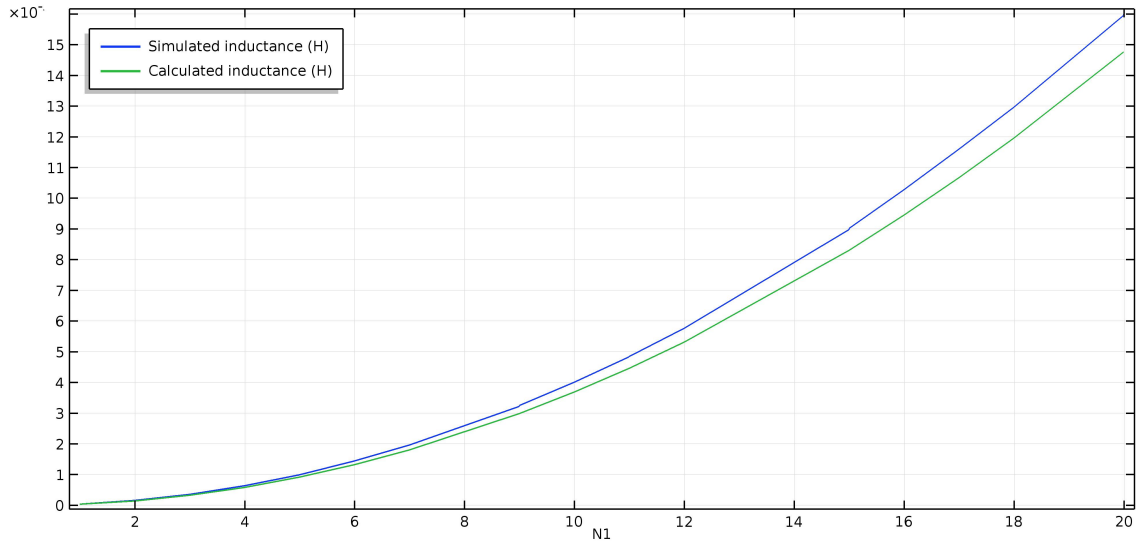
Figure 2.18: Assumed and Simulated Mutual coupling of all power-levels.

Verification of COMSOL model

The setup of COMSOL was verified with literature examples [32] by rebuilding the models and comparing the COMSOL results with the measured values from the study.

2.5 Power transfer calculation for misaligned system

This section will show how the power transfer for various misalignment's was analytically calculated –Appendix B.1–. The misalignment of the coils, that occurs during dynamic charging causes the mutual inductance of the coils to change. As other parameters set in the design stage –I_p, self-inductance of coils, capacitors, etc.– remain the same, they cause the system to go out of resonance. Therefore, the load resistance(R_{load}) on the secondary side is adjusted by a DC-DC converter to keep the power transfer at a maximum. This drop in mutual inductance also causes the efficiency of the system to become lower. At certain point the system should be switched off to prevent the system from wasting energy and heating components. For every variation of the mutual inductance, the load resistance was varied between 10 and 0.001 $\Omega$to determine the maximum power transfer. Only solutions that have a efficiency of at least 75% were stored. All values for the optimal load setting were stored to be used in further calculations.

The data from this simulation is used in Chapter 4 to determine the power transfer of the go-kart on the track. The simulations are for a stationary model. For the same results to be obtained in practice some alterations in the controllers are required. The model thus returns possible power output on various misalignment's, but not a controller design as it is not in the scope of this research.

A Series-Series Simulink model was then used to verify the analytic calculations, that is shown in Appendix B.2. The model was provided by the faculty of EWI from Delft University of Technology and is shown in Figure 2.19. Readouts for current and power were added to provide feedback and ensure current limits are not surpassed.
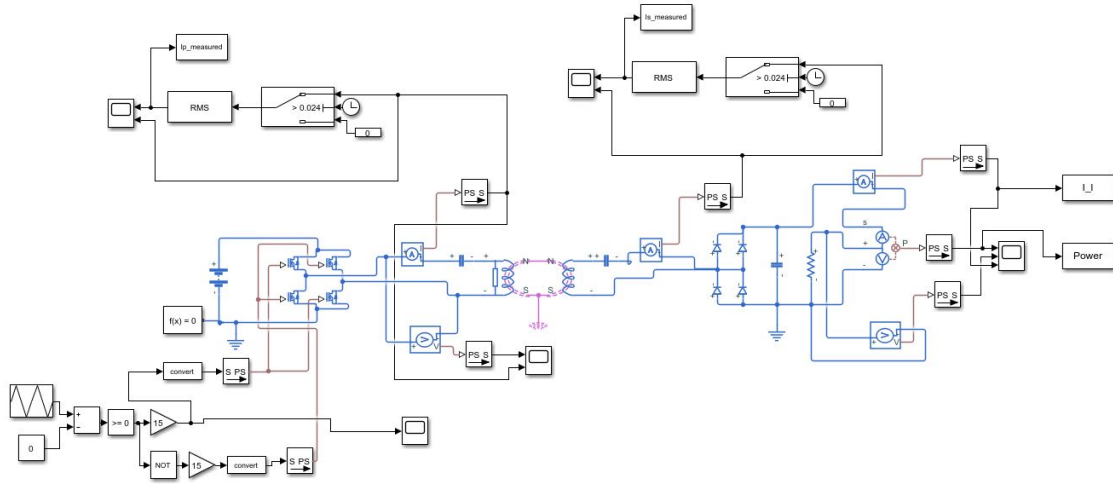
Figure 2.19: Simulink model provided by EWI TU Delft.

2.5.1 Parameter selection

The parameters required to run the Simulink model are the following:

- Frequency (fs)
- Load resistance (R_l)
- Primary coil resistance (R_1)
- Secondary coil resistance (R_2)

- Input voltage (V_{dc})
- Mutual coupling (Lm)
- Self inductance receiver (Ls)
- Self inductance transmitter (Lp)

The frequency and primary current were already determined and fixed in Chapter 2. The model also requires the capacitors of both primary(Cp) and secondary side(Cs) to be determined; these are calculated from the parameters Lp and Ls by equation (2.12) and (2.13), respectively. These are calculated for the aligned position and then fixed, as no change in capacitors is possible during driving without adding complex switching boards.

$$C_p = \frac{1}{4\pi^2 L_1 f_s^2} \tag{2.12}$$

$$C_s = \frac{1}{4\pi^2 L_1 f_s^2} \tag{2.13}$$

2.5.2 Mutual inductance mapping

The mutual inductance was determined by a sweep study of the final design in COMSOL. From these sweeps it was also shown that the difference in Lp and Ls are negligible in misalignment; therefore, these were assumed to be constant for all charging positions. The boundaries of the area that provided the parameters are shown in Table 2.7.

Table 2.7: Boundaries of the Parametric sweep quarter.

Boundaries of quarter sweep study			
Longitudinal displacement	300 mm	Lateral displacement	300 mm
Longitudinal variation	25 mm	Lateral variation	25 mm

A sweep in COMSOL was conducted varying the offset in both lateral and longitudinal direction. All section are based on a quarter of the model to reduce computation-time, as the model is symmetrical in both directions. The longitudinal boundary was set at 300 mm; as the receiver passes just over half primary transmitter-set in this distance; the step-size was set at 25 mm. For the lateral displacement a area just larger than the half the coil width is required to be able to obtain all possible positions in misalignment, again due to symmetry; the lateral displacement was set at 300 mm and for the step-size the same 25 mm increments were taken.
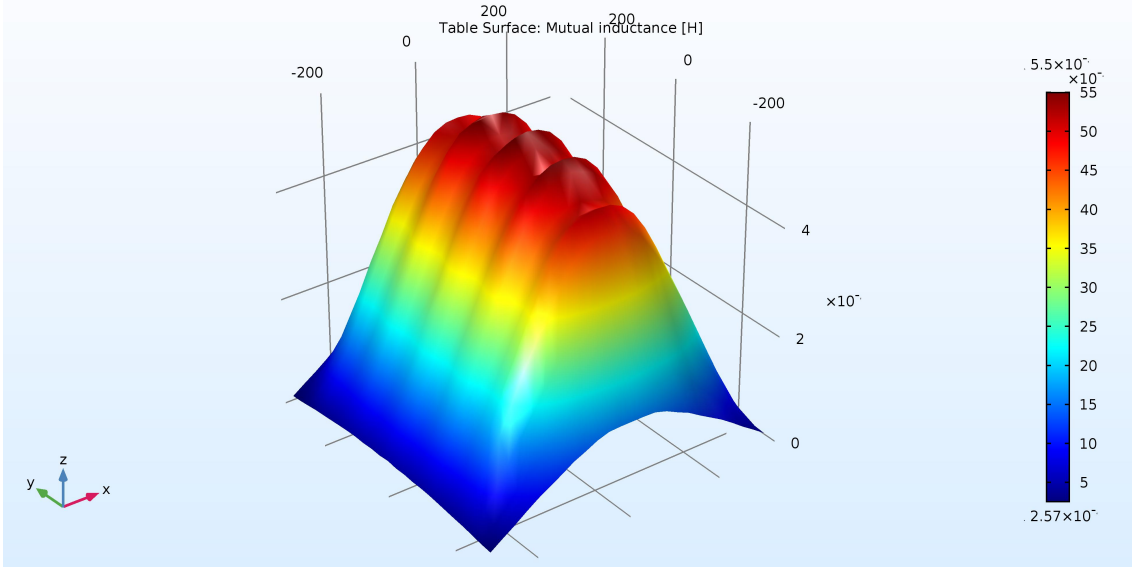
Figure 2.20: Mutual inductance values between coils as a function of misalignment.

The resulting mutual coupling grid was mirrored in both lateral and longitudinal direction to compose the mutual coupling grid for all possible misalignment positions, that is shown in Figure 2.20. In this figure the mutual inductance relative to the misalignment from perfect alignment are shown.

2.5.3 Power mapping

Analytic mapping

The mutual inductance values are used to determine the optimal R_{load}, I_s, and power output for all misalignment's. To achieve a stable power output the DC-DC converter on the receiver side is used to regulate the R_{load}, while the I_p is kept constant. The flowchart for finding the maximum power settings are shown in the flowchart of Figure 2.21.
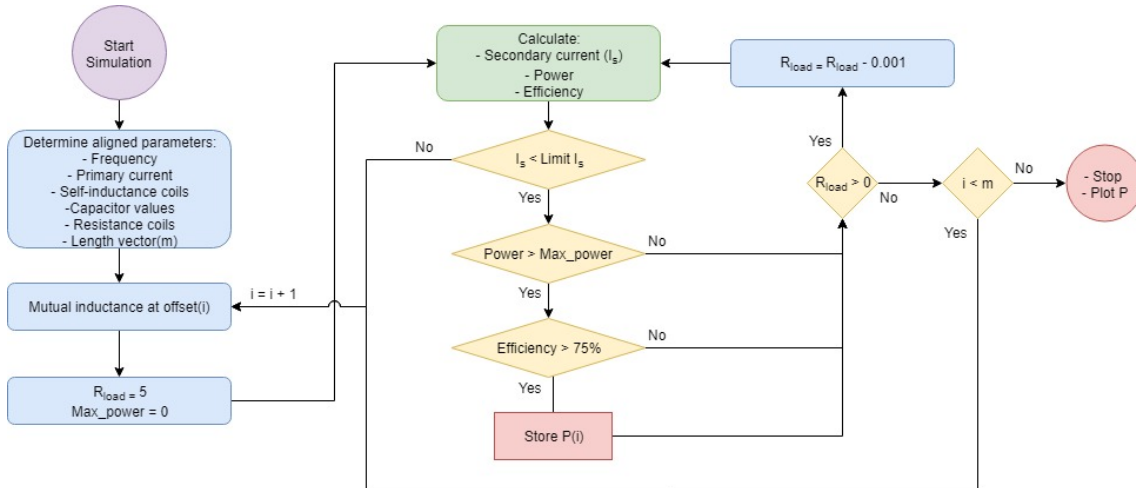

Figure 2.21: Flowchart power transfer mapping.

In order to determine the secondary side power output, the secondary side current was calculated with the help of equation (2.14) as shown in the previous section.

$$I_s = \frac{j\omega L_m I_p}{Z_2} \tag{2.14}$$

48

Therefore, the secondary circuit impedance(Z_2) needs to be determined by equation (2.15). In this equation the i represents the location of the mutual inductance, that corresponds with an offset.

$$Z_2 = R_2 + R_{load} + j * (\omega * (L_s + L_m(i) - \frac{1}{\omega * C_s})) \tag{2.15}$$

In the calculation the only varied parameters for all different misalignment situations was the mutual inductance and the resistance of the load(R_{load}). The load resistance was varied while all other parameters were kept equal to establish the maximum power transfer for each misalignment. All misalignment's that caused an efficiency below 75% were stored as empty values. The result of this mapping is shown in Figure 2.22.
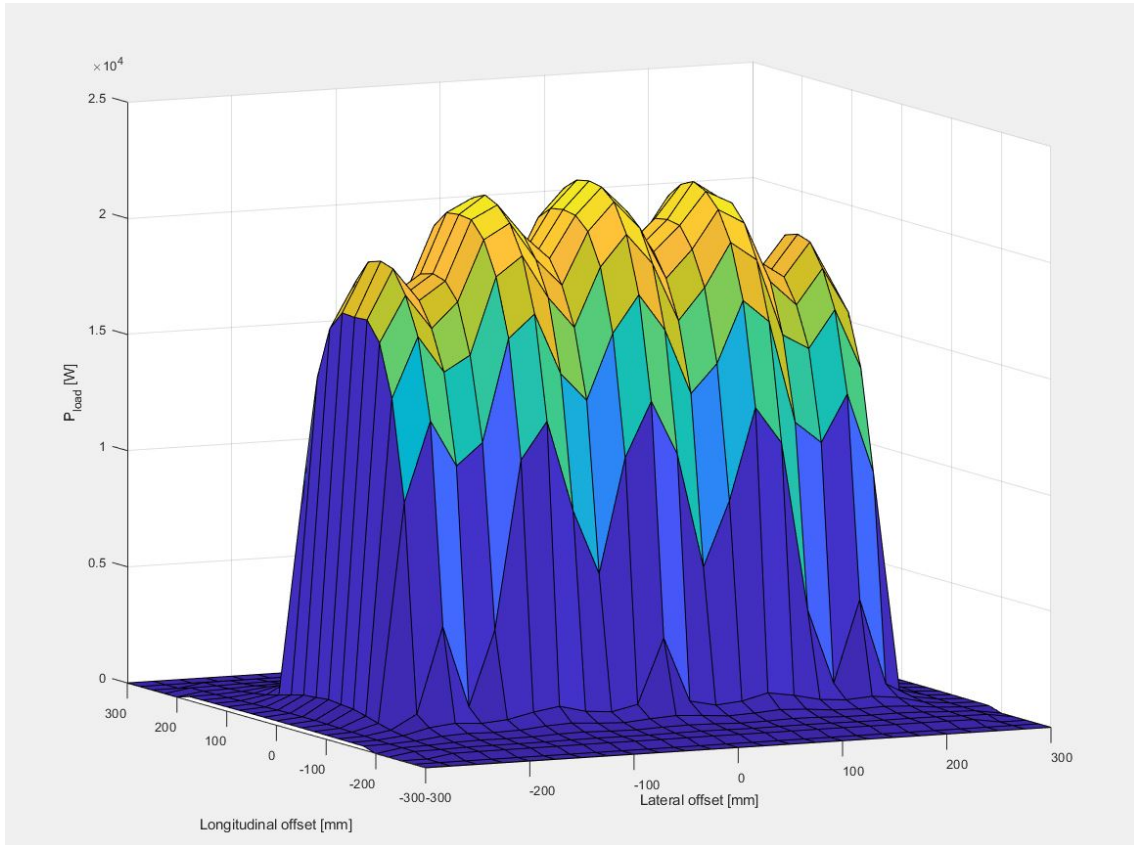
Figure 2.22: Analytic power mapping.

Simulink verification

The simulation in the Simulink model was preformed to verify the analytic calculations. Figure 2.23 shows the flowchart for finding the optimal power output according to the Simulink model, that should be in accordance with the analytically calculated power mapping. The R_{load} from the analytic calculations was used as input after which the voltage of the primary was determined to ensure that the primary side is kept at 40 A. The load adaptation ensures that the currents and efficiency do not exceed the set limits. The power output graph is shown in Figure 2.24.
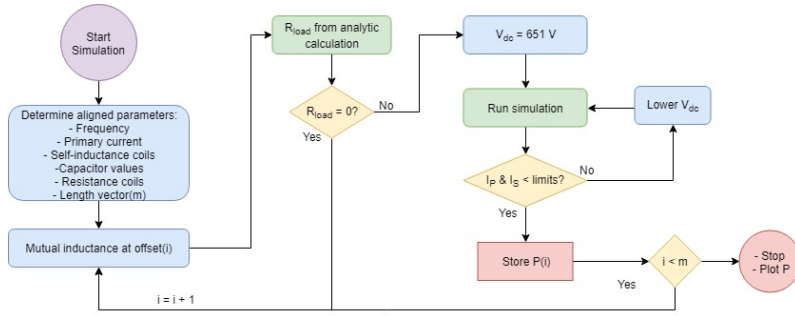
Figure 2.23: Flowchart for V_{dc} adaption in Simulink.

The voltage drop across many different electrical components in the system is not taken into account in the analytically calculation. This is expected to cause some deviation between the calculated and simulated power-maps. However, as both power-maps are quite similar the calculations are deemed verified. The deviations between the two graphs is mainly seen in the areas of high power output; this is likely to be a result of the higher secondary current, that cause more losses. Further development leaves many possibilities for optimization, but this is not in the scope of this research.
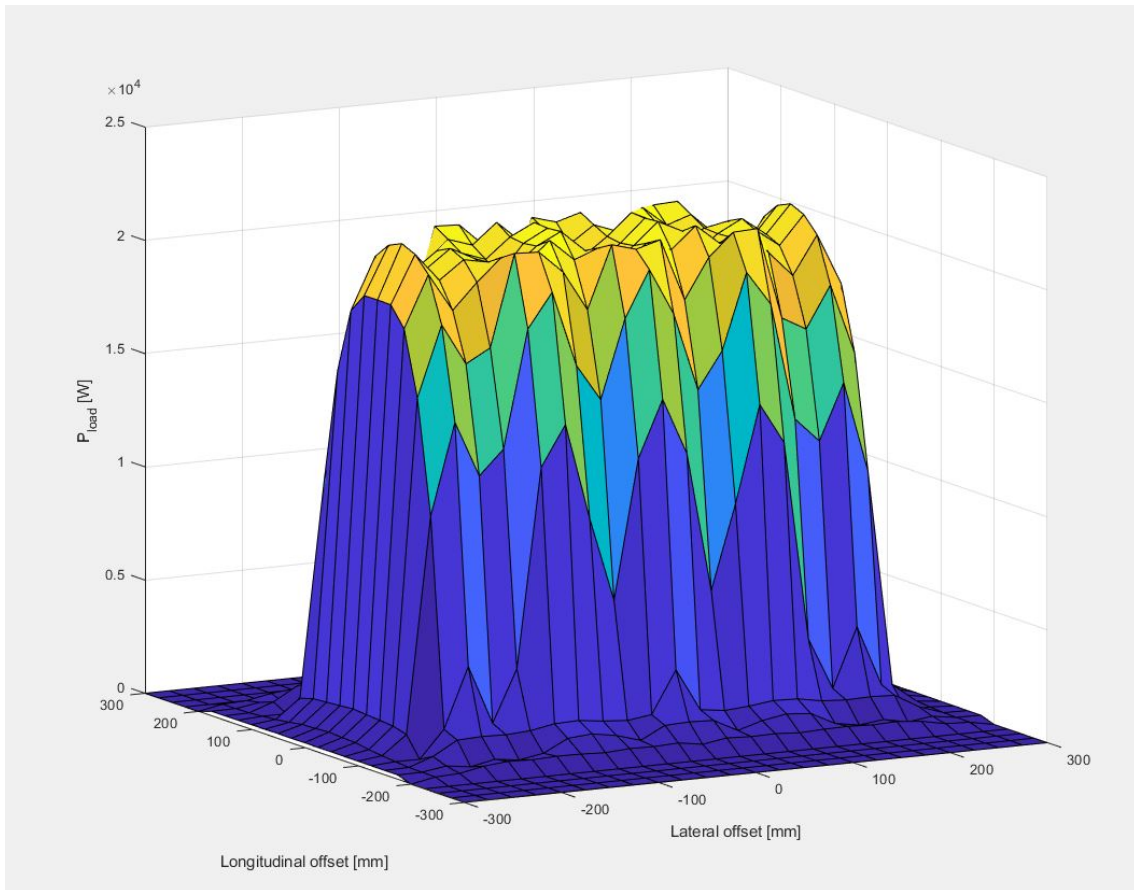
Figure 2.24: Simulink power mapping.

2.6 Conclusion

The goal of this chapter was to determine the boundaries of the system and design an IPTS suitable to implement on a rental go-kart. In order to make an informed decision on the optimal setup for such a system, all possible setups within the boundaries had to be compared; for which a design method was determined. It has shown the reasoning behind the boundaries and the effect that power-levels have on the amount of copper required by the system. The main variable within this comparison was the amount of Litz-wire used, that determined the magnetic field around the transmitters.

First, all boundaries of the systems were established and the average design was determined. This was mostly determined by the geometry of the go-kart and current density requirements for Litz-wire. The installation area was determined to be 1200x 600 mm, where the coils width could be 50 mm at maximum. These boundaries were used in a FEM analysis to determine the mutual inductance between transmitters and receivers, that could be scaled in analytic calculations to determine the coupling for all number of windings within the boundaries of the system. A script was then ran to determine all possible power-levels and show how these related to the total usage of copper is the system. This amount of copper used is important as it is a substantial contributor to the total cost of the system. From these results a 23 kWh IPTS was selected, as several iterations determined that this was the minimal power output for the system to have the desired effect on the SOC of the battery-pack.

COMSOL was then used to determine the mutual inductance of the design at all alignment-positions, that was used to calculate the power output of the system at all positions. This was done by varying the mutual coupling of the system, while the rest of the input parameters remains fixed; much like a real system. The maximum power output was then determined as a function of the output resistance(R_{load}) and efficiency of the system. A Simulink model provided by the University was used to verify these calculations. The resulting power-map, shown in Figure 2.22, will be used in the case-study of Chapter 4.

Chapter 3

Safety analysis of go-kart ipts

3.1   Introduction

Safety is an important factor in the designing of Induction Power Transfer System (IPTS) that should be carefully examined before construction. Detailed analysis and physical measuring of the Electromagnetic Field (EMF) for any IPTS is of the utmost importance for the safety of the public and workers before it is used.

The first part of this chapter is used to identify the possible hazards of an EMF and how these effects the human body. Subsequently, the areas in which these values are required to stay within limits are indicated. These are used to determine whether the system operates within the limits set by the International Commission on Non-Ionizing Radiation Protection (ICNIRP). The second part discusses the flux- guidance and shielding in the system. It also elaborates on the materials that are used to achieve this guidance and shielding. Simulations of both the shielding and guidance of flux then helps to determine the best setup for the final design of both the transmitter and the receiver. In the final section the magnetic flux levels in the areas of interest of the final design are determined. Some suggestions to improve the design before construction are also shown here.

The conclusions from previous chapters are used to determine the design for which the safety of the system is analyzed. In this chapter only the most important figures are shown, that are key in determining the final design requirements for safety. For all graphs the size of the elements in the Finite Element Method (FEM) analysis causes some distortion; therefore, it is imperative to look for trends in these graphs, rather then between the resulting values themselves.

3.2   Safety hazard's of Electromagnetic Field

The ICNIRP has developed limits for both public and occupational exposure to protect them from harmful EMFs. Occupational exposure can be higher as the workers are trained to the effects of EMF, whereas untrained public could be confused by the effects. In both cases the EMF is small enough to prevent any damage to tissue or nerves. There is also a distinction based on frequency by the ICNIRP, namely:

- Low frequency (< 100 kHz)
- High freqeuncy (> 100 kHz)

As the frequency is determined to be 20 kHz, the low frequency guidelines are considered. These are in many aspects similar to the high frequency guidelines, but lack the consideration of tissue heating due to high frequencies. The safety hazard's associated with EMF according to the ICNIRP at low frequencies are the following:

- Induced retinal phosphenes
- Perception of surface electric charge effects
- Peripheral and central nerve stimulation
- Possible effects on some aspects of brain function

These effects are all acute as the ICNIRP found no scientific evidence that proves a causal relationship between low frequency magnetic fields and chronic effects on the human body. Studies on both direct and indirect effects were examined to achieve the most comprehensive understanding of the effects of EMF on the human body. The direct effect are the effects of the fields on the body, whereas the indirect effect are the effect of potential difference between the body and a conductor that is influenced by this field.

Based on all these studies the guidelines for limiting exposure to time-varying electric and magnetic field(1Hz-100kHz) were determined. However, as this guideline is based on the understanding of these effects by science at this time, these guidelines might need to be adjusted in the future. The guidelines from 2010 are also a reworked version from the 1999 guidelines, that were a lot more strict as understanding was not as great as it is right now. The table for exposure limits of the public is shown in Figure 1.29. Here it can be seen that, for frequencies between 3kHz and 10 MHz, the maximum magnetic flux density(B) is 2.7×10^{-5} [T]. The magnetic flux density should therefore not be exceeded beyond this values on and around the go-kart. This maximum is 5 times lower than the maximum of workers, that have been instructed on how to deal with these effects.

Retinal phosphenes

Most effects are descriptive in nature, but retinal phosphenes are less intuitive and is therefore discussed briefly. A retinal phosphenes is the perception of light in the eye, while this light is not actually subjected to the eyes but induced by stimulation of the retina. In this context the magnetic field effects the retina in such a way that phosphenes occurs. This induced retinal phosphenes causes a distortion in the visual field of persons effected by this. A artistic example of this distortion effect is given in Figure 3.1.
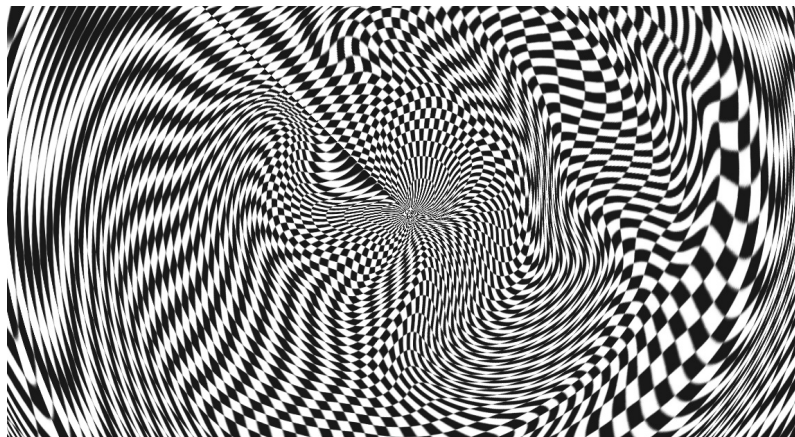

Figure 3.1: Artistic impression of a phosphene [45].

3.2.1 Areas of interest

The EMF analysis is mostly done to determine the safety of the public and to ensure that no saturation occurs. However, not all areas around a go-kart need to fall between these limits. In the area where power transfer occurs –between the go-kart and the transmitter– the level will need to be higher in order to transfer the required amount power. For all situations it is assumed that the system knows when a go-kart is in the charging position above the coils and is only then activated.

The area in which the driver is seated will be the primary focus for the safety analysis and this is, therefore, the most important area of interest. The ferrite bars are also an important area to review, as the magnetic flux density needs to stay within certain limits for the bars to effectively guide the flux.

(a) Driver-box.
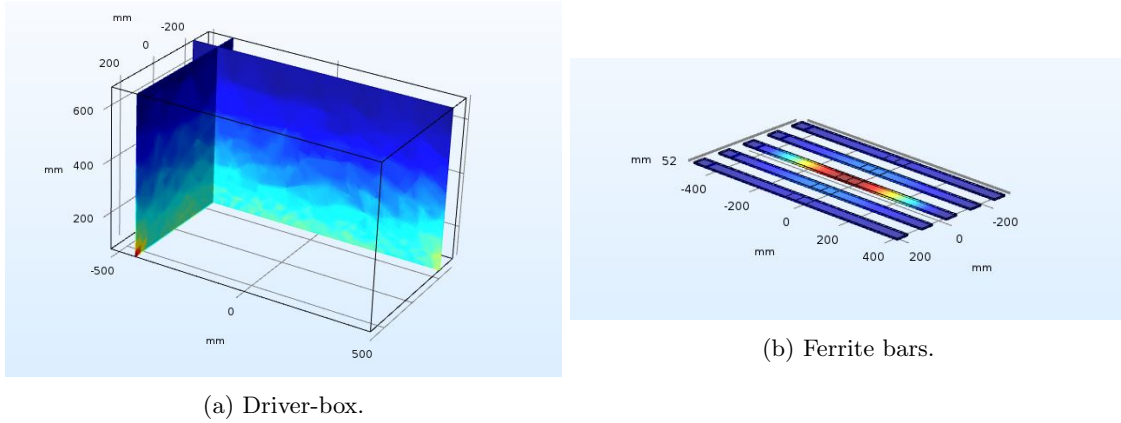
(b) Ferrite bars.

Figure 3.2: Areas of interest for magnetic flux density analysis.

Figure 3.2 shows the ferrite bars and the 'driver-box'; that was used in COMSOL to determine the maximal peak flux in the drivers area. It is assumed that the driver is confined to an area of 600 mm in width and 1000 mm in length. The box is positioned 50 mm above the shield, in order to leave room for the go-kart frame. The box was defined as a box of air, as the permeability of air is the same as that of human tissue [20].

3.3   Effect of flux guidance

In this section the effect of flux guidance on both the EMF around the go-kart and the coupling between the coils is determined. First, a closer look at the material that are used to guide the flux is taken: Ferroxcube 3C94. Secondly, the effects of different geometrical setups of flux guidance on the averaged design are established and used to determine the required length of the ferrite. For the average design multiple lengths of ferrite are swept in the COMSOL model, to determine its ideal length. The same is done for the thickness of the ferrite.

Material properties 3C94

The used material for the flux-guidance is 3C94 ferrite, that has a high magnetic permeability. The magnetic permeability of this material drops when the peak flux density becomes higher than 0.3 T; which is shown in Figure 2.8 of Chapter 2. From this point a larger external magnetic field does not further improve the amount of flux guided through the material; this effect is called saturation. The peak flux density in the ferrite should therefore remain below 0.3 T, as saturation occurs beyond this level. This can be achieved by adapting the thickness of the bars, which increases the area used to guide the flux. A larger area will reduce the flux density, as the amount of flux remains equal. In the COMSOL-models the H-B curve is implemented in the material properties to ensure that saturation is accounted for and calculations are as realistic as possible.

The permeability is also dependent on the temperature and frequency of the field. The variation of this permeability between the temperature of 25°C and 100°C is small. Because the working region [40] of the charger is very close to this range, the temperature effect on the permeability was neglected.

The frequency also impacts the permeability of the 3C94, as it decreases the permeability above a frequency of 100 kHz. Considering that the final design will be ran at 20 kHz, this causes no problem for the design. However, if future work would require the frequency to be adapted in modeling, this effect should be considered.

3.3.1   Receiver flux guidance

For the receiver it is important to determine the required length and thickness of the ferrite. Both will have to be minimized in order to reduce weight, while keeping the power levels high and the EMF values low.

Ferrite length

To determine the required length of the ferrite a sweep was conducted. The sweep ran from 100 mm ferrite bars –at which the ferrite just bridges the width of the coils in the center– up to 1000 mm long bars –at which the ferrite reaches the inner diameter of the coils again– with increments of 100 mm. The resulting mutual coupling at different offsets are shown in Figure 3.3. The first part of the graph shows an increase in mutual coupling correlated with the length of the ferrite in all cases. In the second part of the graph both longitudinal aligned flatten out asymptotically, whereas the misaligned case continue to rise at a lower rate. The reduce the weight and cost of the ferrite the length for the final model was set at 800 mm; which ensures that coupling can be guided throughout the total coverage of the coil, but no excess ferrite is used.
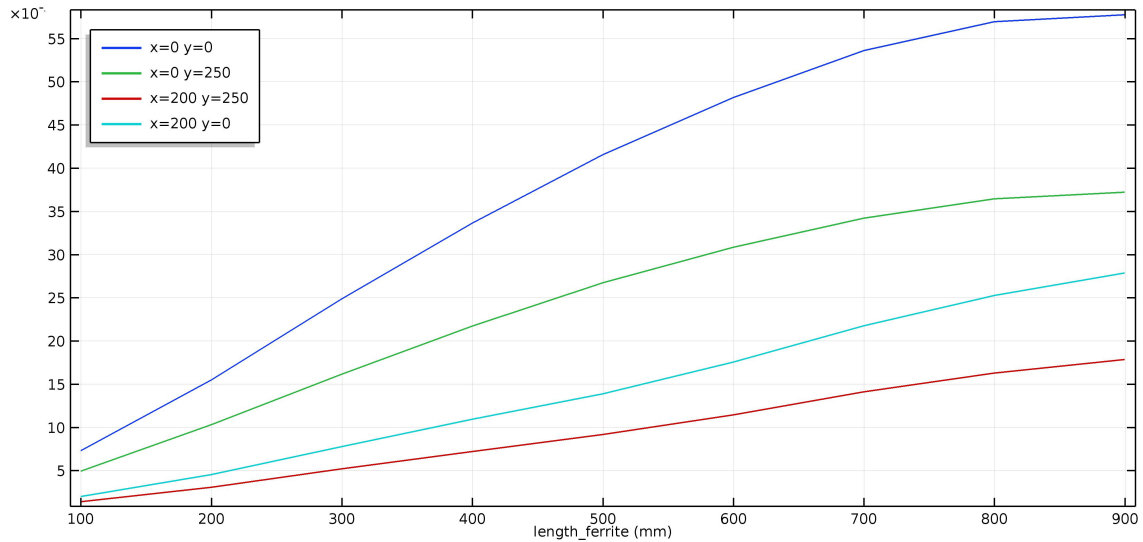
Figure 3.3: Influence of ferrite length on mutual coupling.

The EMF values in the drivers-box are shown in Figure 3.4, that shows that the influence of the ferrite length in the different alignment positions is very small. It also shows that the shielding in both directions needs to be improved, especially in the y direction. The mutual coupling will, therefore, be leading in the determination of the ferrite length; that was set at 800 mm.
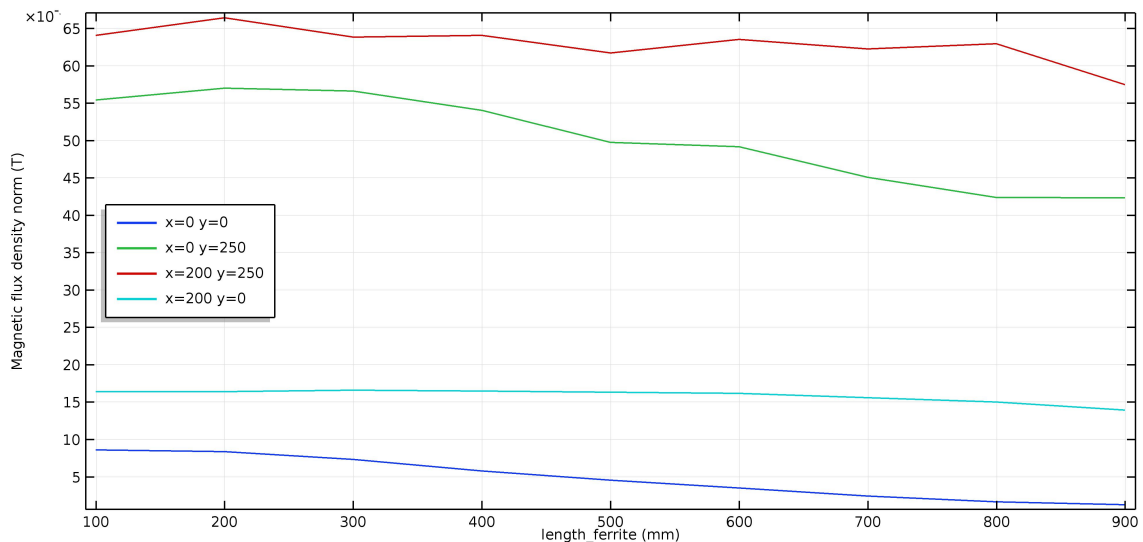
Figure 3.4: Influence of ferrite length on EMF in drivers-box.

55

Ferrite thickness

The thickness of the ferrite is important as it should not be loaded beyond saturation, which occurs at 0.3 T. As weight is such an important factor of the feasibility of the system it also should not be over-designed. For this a sweep was conducted to determine the minimum thickness of the ferrite. This sweep was done in the most aligned position, as this is the position in which the power transfer and thus magnetic field through the ferrite will be the strongest. The result of the maximum flux density of the different thicknesses are shown Figure 3.5. In this graph the saturation line is also shown; therefore, the minimum thickness of the ferrite should be 3 mm as the line is cleared beyond this point.
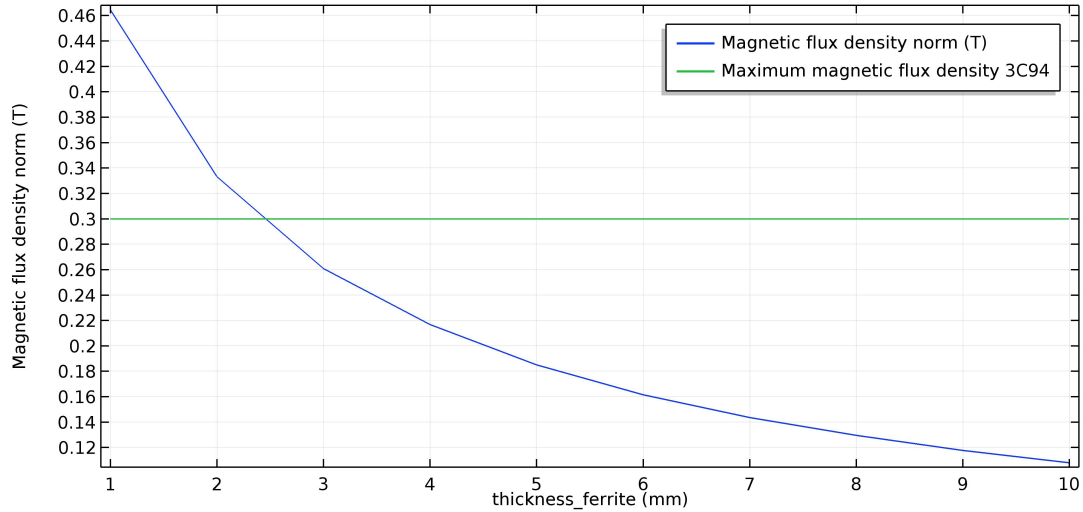
Figure 3.5: Ferrite 3C94 thickness effect on flux density in bars.

However, the mutual coupling is also effected by this thickness as shown in Figure 3.6. For this reason the thickness of the ferrite was set at 7 mm. Optimizing the ferrite could result in some reduction in weight and should thus be considered in prototype design.
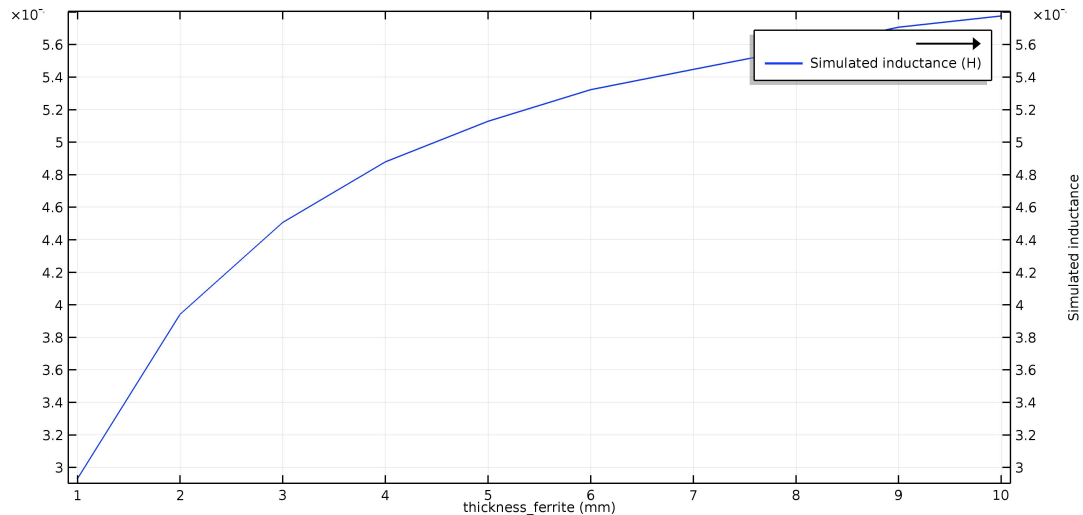
Figure 3.6: Mutual coupling with varying thickness of receiver ferrite.

3.3.2 Transmitter flux guidance

For the transmitter design of the S-shape tracks [32] are used, as they have proven to be able to transfer 22 kW at this frequency. For the base ferrite a larger block is required, as the magnetic

56

flux density at the corner of the coils got very high. This should be further optimized before production, as a significant reduction in amount of ferrite –hence cost– can be achieved and this is probably the effect of the mesh-size that was used in calculation.

3.4 Effect of flux shielding

To ensure that the EMF around the go-kart is within the limits of the ICNIRP guidelines, the final design is investigated. As shown in Chapter 1, the mutual coupling is negatively effected by the shielding. An aluminum shield above the coils was already installed before optimizing the parameters to reduce changes in coupling after optimizing. In this section the influence of the material, the thickness of the shield, and the addition of a aluminum rim is investigated.

Shield material requirements

The shielding of a magnetic field is established by the eddy currents in the shielding material, which oppose the magnetic field that creates them [46]. In order to create eddy currents a material has to have a high electric conductivity. This is the reason that air is not a good shield, even though the magnetic permeability of air is almost the same as copper and aluminum.

Table 3.1: Cost of shielding materials.

Material	Permeability	Cost [1]
Aluminum	1.256665×10^{-6} H/m	€1,73/kg
Copper	1.256629×10^{-6} H/m	€5.55/kg

The most important reason to use aluminum instead of other materials is that it is relatively cheap and provides a solid framework for the rest of the receiver to be attached to. Table 3.1 shows the permeability of aluminum and copper, together with their cost. The need for a framework and difference in price make aluminum the obvious choice for this system. It is imperative that during installation the attachment methods to the go-kart are reviewed, as some might compromise the effectiveness of the shield.

3.4.1 Receiver shielding

The receiver shielding is provided by the shield itself and the rim around the coil. Both are used to restrain the magnetic field to the area of transfer.

Shield thickness

The effect of shielding thickness is determined by simulations. The height of the shield is varied from 4 mm up to 10 mm, in 1 mm increments. The maximum is determined by the thickness boundary of the transmitter –which was set at 30 mm– and the reserved spacing for the ferrite and coils; that were set to be 10 mm in both cases. The minimum is determine by its requirement to act as a framework for the receiver, in which 4 mm is already consider small for construction purposes. The distance of the shielding from the coil is frozen and the increase in thickness was directed towards the go-kart, without moving the shield closer to the coils; as this could negatively effect the coupling between the coils. The effect of the shield thickness is measured by determining the mutual coupling, and the maximum EMF values in the driver-box.

---

[1]data from 4-12-2018
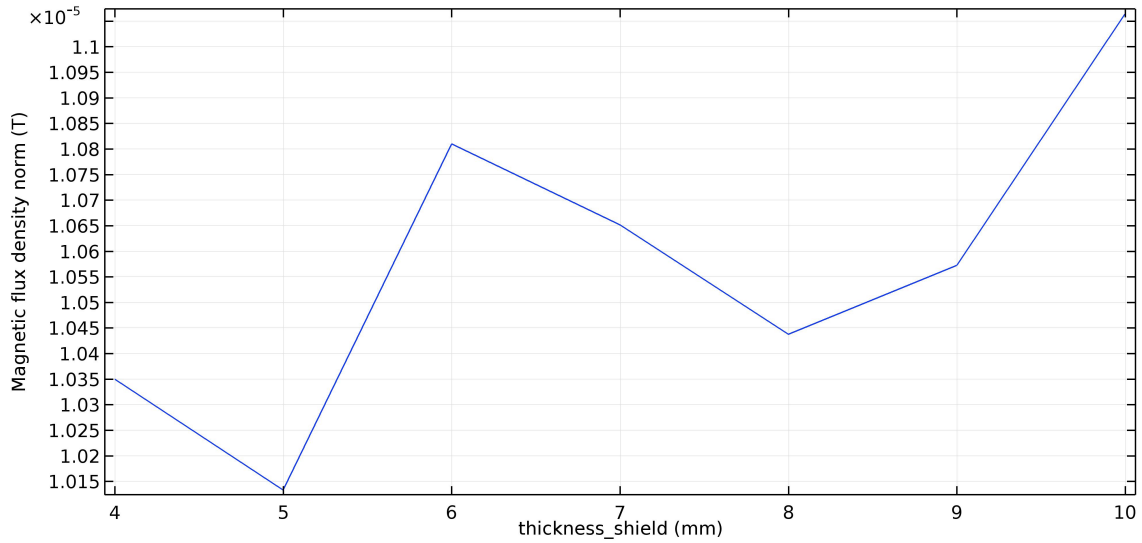
Figure 3.7: Influence of shield thickness maximum magnetic flux density in drivers-box.

The shield thickness hardly effects the EMF in the driver-box, as shown in Figure 3.7. The effect on the mutual coupling is even smaller, under 2%. Therefore, the shield should be chosen to be as thin as 4 mm. A smaller shield would be impractical as it needs to support the weight of the other components and hold the threads that construct the shield to the go-kart. The use of a hollowed frame or composite materials might be able to lower its weight even further without compromising its structural strength. However, this falls beyond the scope of this research and for now a 4 mm thick shield will be used in the final design.

Rim height

The addition of a rim in the final design could be able to greatly reduce EMF around the go-kart, especially in stationary charging. By varying the height of this rim and studying the effects, the optimal design of the rim is determined. The effect it has on the mutual inductance, and the maximum EMF in the driver-box in the aligned position is investigated.

The rim-width was set to be 10 mm. It was designed to start at the outer dimensions of the receiving coils. The height of the rim was then varied in 1 mm increments from 1 mm to 26 mm, which is the maximum height determined by the boundaries of the receiver geometries and the minimal thickness of the shield.
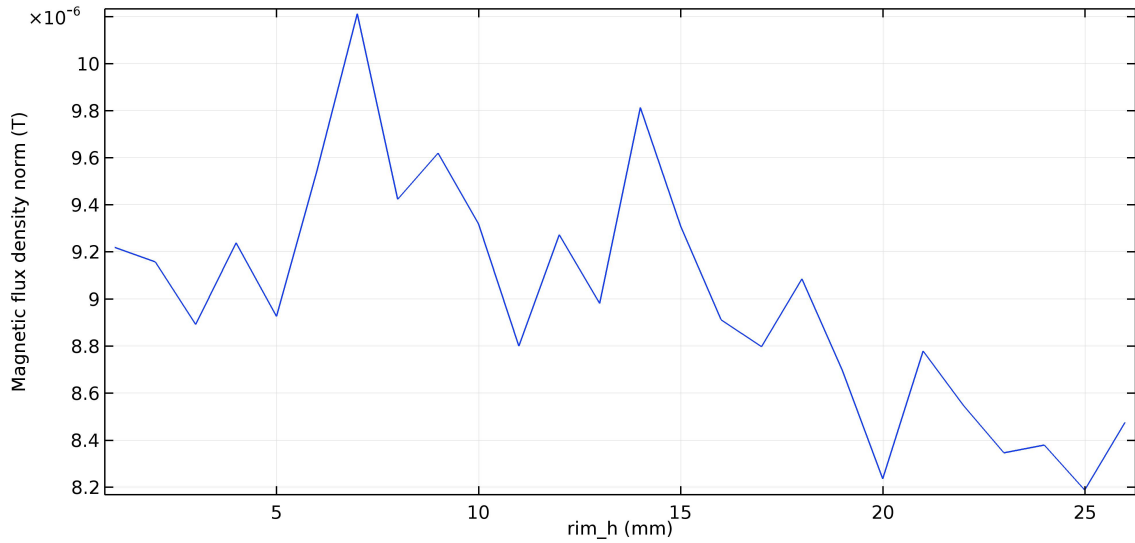
Figure 3.8: Influence of rim height on maximum magnetic flux density in drivers-box.

The resulting mutual inductance values differs only slightly, together with the magnetic flux density in the bars. In the driver-box a downward trend in magnetic flux density can be observed as function of the rim height; that is shown in Figure 3.8. The rim is determined to be equal to the height of the ferrite and the coil combined, so no extra height is introduce in the receiver by the rim. In this case the previous section had determined them to be 16 mm in height combined.

Shielding extensions

The shield does not yet offer the shielding required to protect the driver. However, extension of this shield or shielding applied to the go-kart could significantly improve these resulting EMF values. In order to determine the require addition shielding in lateral direction, the maximum misalignment is prescribed and the shield is extended until the driver-box values are within the limits. This is reached when the shield width is 800 mm, as shown in Figure 3.9:
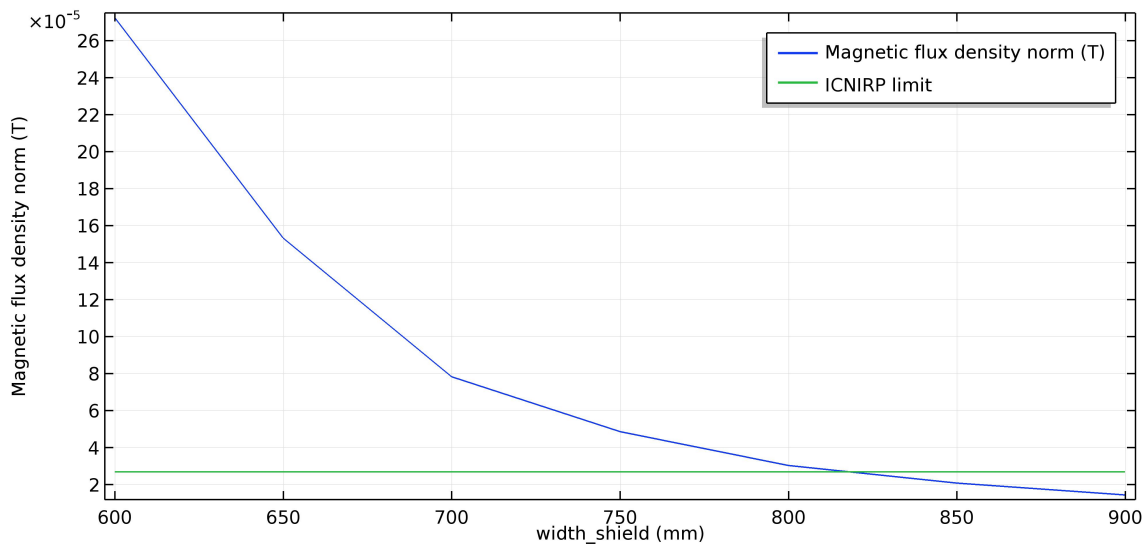

Figure 3.9: Shield width extension effect on maximum magnetic flux density in driver-box.

A misalignment is then also introduced in the longitudinal direction –with the shield width extended to 800 mm– and a sweep is conducted to determine the require length of the shield. However, the shielding proves to be slightly too small and the width is extended with an extra 50

mm; that brought the total width to 850 mm. The resulting graphs are shown in Figure 3.10, that shown that the length of the shield is required to be 1350 mm.
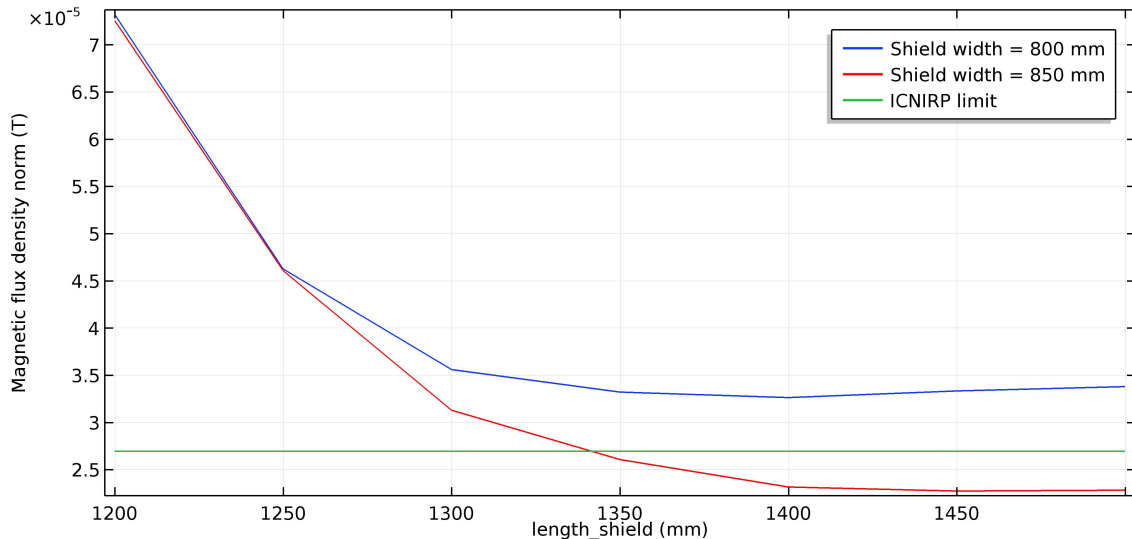

Figure 3.10: Shield length extension effect on maximum magnetic flux density in driver-box.

Figure 3.9 and 3.10 show that a shield extensions –of merely 250 mm in width and 125 mm in length– can provide the shielding required to keep the EMF within the limit in the driver-box. This can also be achieved with shielding integrated in the frame of the go-kart.

3.4.2 Transmitter shielding

The shielding of the primary coils was already assumed constant in all simulations, as it deemed required to keep the EMF values low enough around the track. The isolation of transmitters-pairs is required to achieve a low EMF around the track [29]. However, as will be shown in the section on cost, this is of great influence of the feasibility of the system and optimization can help reduce this cost. An simple example of this optimization is provided, by the use of less ferrite and the addition of ferrite in places that require a lower magnetic flux density.

3.5 EMF levels in final design

The previous sections were used to determine the required geometrical parameters for the receiver, which are shown in Table 3.2. The following section should, therefore, all fall within the limits of saturation and ICNIRP. The sweep conducted in COMSOL for the determination of the mutual inductance is used to also determine the EMF values in the different offset positions.

Table 3.2: Geometry of shielding and guidance materials in the final design.

Geometry parameter	Value
Shield length	1020 [mm]
Shield width	600 [mm]
Shield thickness	4 [mm]
Ferrite length	800 [mm]
Ferrite thickness	7 [mm]
Rim height	17 [mm]

3.5.1 EMF values in ferrite bars

The maximum magnetic flux density in the ferrite bars is required to be below 0.3 [T] at all times, to prevent saturation of the ferrite. The ferrite thickness was determined in previous section and the resulting flux density of the final design is shown in Figure 3.11.
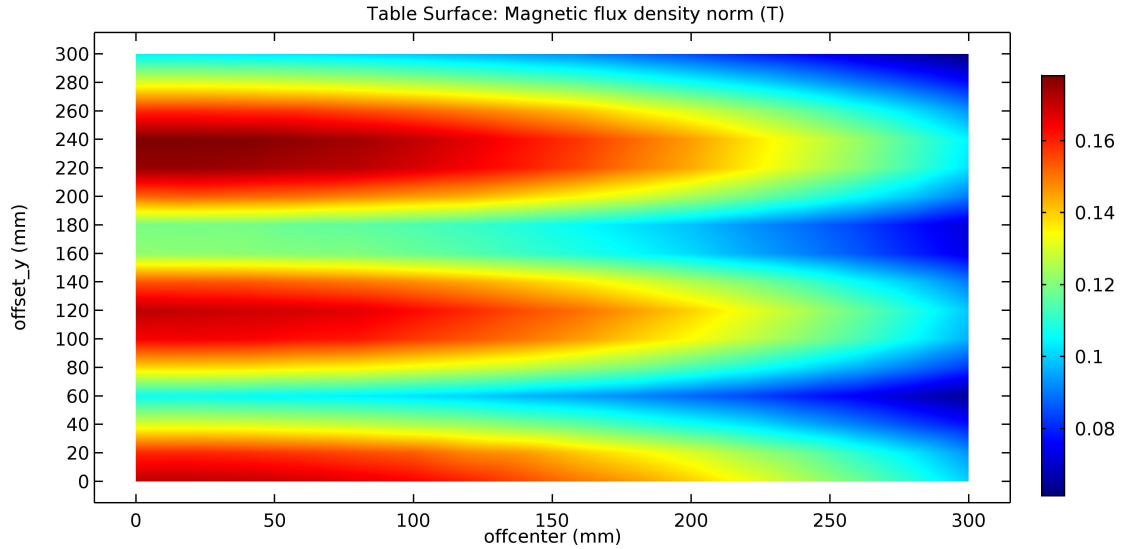
Figure 3.11: Maximum magnetic flux density in ferrite bars.

3.5.2 EMF values in driver-box

The maximum level of magnetic flux in the driver-box is also determine by the COMSOL sweep. The resulting values are processed in Matlab to create Figure 3.12; that also shows the ICNIRP limit-value as a dark-blue surface in the graph.
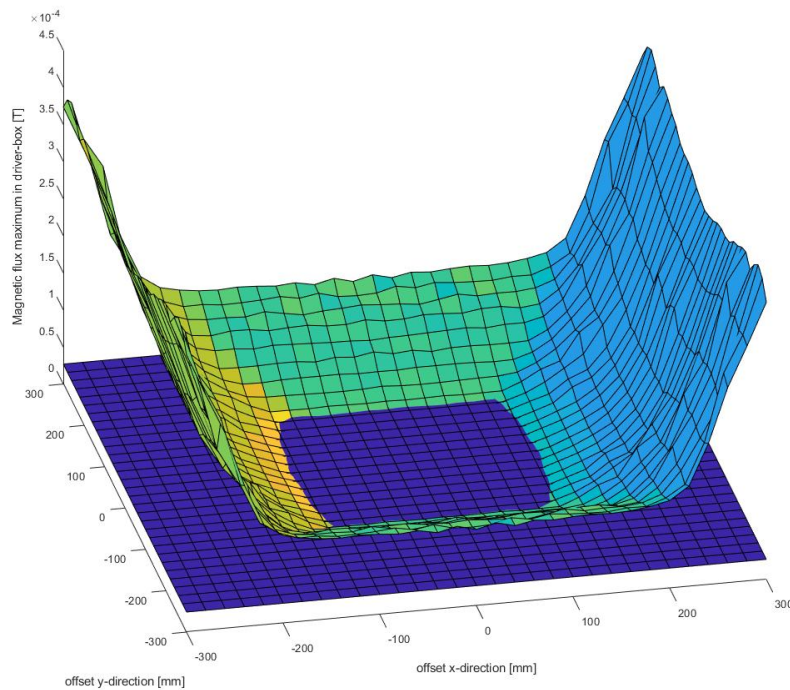
Figure 3.12: Map of EMF and limit of exposure.

As the graph shows, there is only a small area were the EMF values do not exceed 2.7×10^{-5}. This would drastically limit the overall charging capabilities of the system, as the allowed charging sections would be reduced. However, these levels are the absolute maximum, as the frame of the go-kart is not accounted for in this simulation; that will also generate eddy currents that oppose the EMF and thus reduce the maximum values.

EMF after shielding extensions

To enable a larger charging area, the additional space between both the front and back wheels could be used to provide extra shielding. This extra shielding could also be done in other parts of the go-kart–between spacing in the frame for example–. However, this is not in the scope of this research, as it is optimizing the design.

For now, the effects of the shielding extensions –from the previous section– are investigated. The edge is placed around the existing shield, up to the values deduced in the previous section. The resulting EMF mapping of the driver-box shown in figure 3.13.
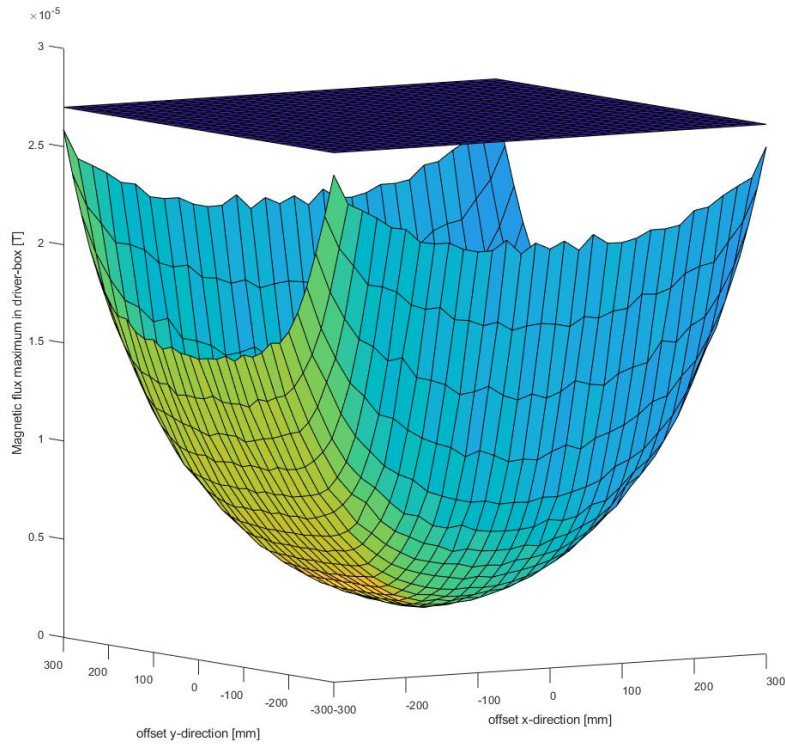
Figure 3.13: Map of EMF and limit of exposure with addition shielding.

As can be seen from Figure 3.13, the resulting EMF values are all beneath the ICNIRP limit. This leads to the conclusion that this model could be used on the condition that enough shielding is applied. If enough shielding is applied, the entire charging region could be used from a EMF level perspective. This does, however, not guarantee that this entire area could be used for power transfer, as there is a limiting factor on this area from a current and efficiency point of view as well, as was shown in Chapter 2.

3.6 Conclusion

This chapter was used to determine the safety of the IPTS in a go-kart by examining the EMF values in COMSOL. An overview of the hazards of EMF was given, along with the maximum exposure limit; that is set by the ICNIRP at $2.7\text{x}10^{-5}$ [T]. The EMF in the driver-box has to fall within the limits of public safety to not harm any individuals driving the go-karts. The ferrite length has little influence on these values, especially beyond the set length of 800 mm. The determination of this length was a compromise between the mutual inductance at longitudinal offset and the weight of the receiver. The EMF limits within the ferrite are set by the saturation point of the material, that is at 0.3 [T]; beyond this point no additional flux is properly guided by the ferrite. The minimal thickness of the ferrite bars to prevent this saturation is 3 mm. However, as mutual coupling was negatively effected by this reduction of thickness, a 7 mm thickness of ferrite was established.

The effect of shielding was then discussed, along with the additional benefit of a shielding rim around the receiver. The simulations for determining the ferrite length had shown that the EMF values in the driver-box were too high in misaligned positions. Shield extensions were proposed and shown to be effective enough for implementation. It is also important to realize that the frame of the go-kart will act as shielding too, but is not yet taken into account. The additional shielding is not complicated, but should be thoroughly investigated before prototyping nonetheless.

The results from this chapter have shown that it is possible to create flux-guidance and flux-shielding, that function within the requirements. The exact design of it is not in the scope of this research and is, therefore, not shown. And additional edge was enough for all misalignment to be shielded in the active region, which is very promising for future design.

Chapter 4

System simulation and cost analysis - Case study

4.1 Introduction

To determine the feasibility of the Induction Power Transfer System (IPTS) on go-karts, designed previously, a case-study was conducted. In this case-study, it was determined whether enough power could be transferred to the go-kart on the specified track. The case-study was performed in Simulink for a 451 meter long, square track combined with set of 20 go-karts. A model was constructed to determine the State of Charge (SOC) of the battery-pack of an electric go-kart and to access what the impact of a IPTS is on the required battery-pack sizing.

First, the track was modeled by recording all accelerations on the track in a Internal Combustion Engine (ICE) rental go-kart. From these measurements a speed-profile was determined and used to construct a virtual 15 minute heat, followed by a 5 minute stationary charging period. In the slowest sections of the track 97 meters of track-wide chargers were then implemented. Second, the go-kart and charger were modeled in Simulink. The speed-profile was then used to determine the distance between the charger sets and the go-kart, in order to determine the power transfer at all points of the track. Third, multiple simulations were to determine influence of the charge, by varying misalignment's and battery-pack sizes. Finally, a comparison of both cost and weight was done for the designed system and alternatives in the market.

4.2 Track modeling

For the modeling of the track a test was performed with a ICE go-kart, to ensure the results are as close to reality as possible. The acceleration in x-, y-, and z-direction were documented. However, the maximum height difference was considered small enough to neglect the acceleration in the z-direction. To simplify the model further only the x-direction speed profile was considered for the simulation. The y-direction, that has an effects on the misalignment in this direction, was simulated by assuming the worst case scenario.

To obtain the speed profile from the acceleration data, it first needed to be filtered and integrated. A low pass filter was applied to smooth out the vibration of the engine and the road surface. After this the result was integrated to obtain the speed profile, as shown in Figure 4.1.

Table 4.1: Parameters of the case-study track.

| Track parameter	Value
Length	451.5 [m]
Width at charging sections	5 [m]
Maximum height difference	0.3 [m]
Top speed (during heat)	67.32 [kph]
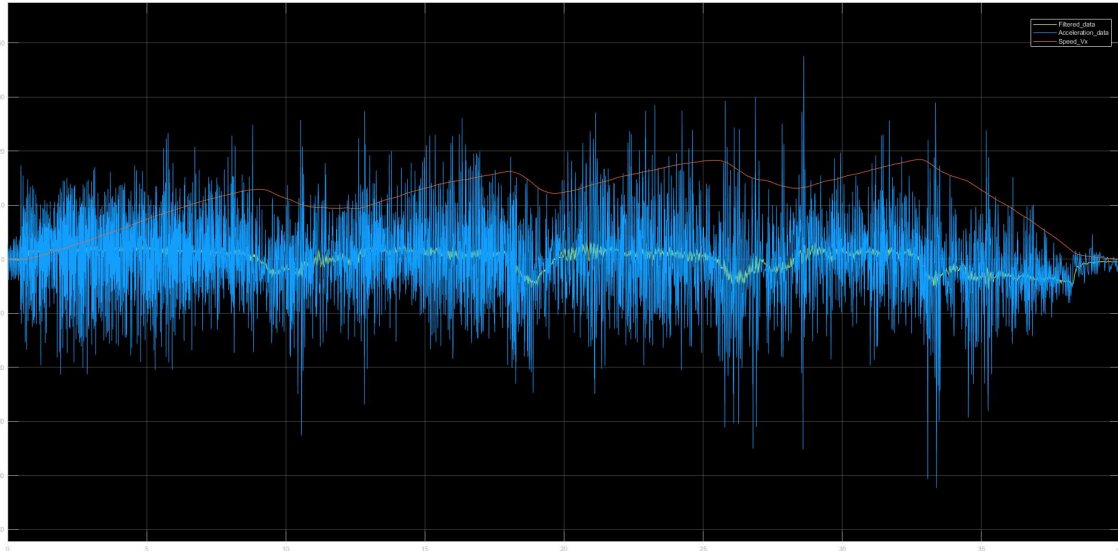
Figure 4.1: Speed profile constructed from acceleration data.

4.2.1 Heat construction

In order to obtain a full length heat simulation, the speed profile from the best lap was divided into three sections: start, middle, and end. These best sections were combined –appendix C.1– and a new time-series was constructed to simulate the full length of the heat, by appending the middle part of the lap until the full length of a heat –15 minutes– was surpassed. The resulting speed profile is shown in Figure 4.2.
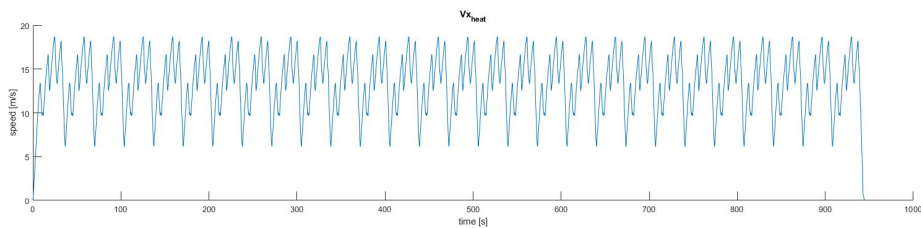

Figure 4.2: Optimized speed profile go-kart heat.

4.2.2 Charging sections

To determine the placing of the charging section, the speed profile from Figure 4.1 examined. The charging is most effective in the low speed sections of the track; contrary to public road charging, where good alignment on the highways results in more effective charging. The location of these sections was determined and for the two sections with the lowest speed a section of approximately 50 meters, track wide primary coils were installed.

4.3 Simulink modeling go-kart

The goal of this modeling is to determine if a go-kart can be run continuously, while being driven for 15 minutes with just 5 minutes stationary intervals. The track is assumed to be 5 meter wide at the charging sections and the speed profile for a average driver is shown in Figure 4.2. The model is shown in Figure 4.3.
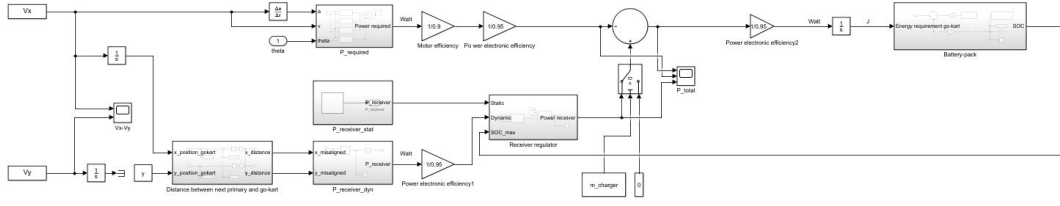
Figure 4.3: Simulink model for an IPTS on a go-kart.

In order to obtain a proper simulation file several aspects will have to be modeled:

- Power requirement from go-kart
- Power supply by IPTS
- Battery levels
- Losses in system

4.3.1 Go-kart power modeling

The primary part to determine is the power requirement of the go-kart, how much energy is required for a go-kart of this weight and size to obtain the speeds and accelerations measured on the track. This is obtained by using the physical formulas for the power required to overcome different forces [47]. These formulas are given in the following equations:

$$P_{go-kart} = P_{roll} + P_{air} + P_g + P_{accel} \tag{4.1}$$

$$P_{roll} = C_{rr}mg\cos\theta|v| \tag{4.2}$$

$$P_{air} = \frac{1}{2}C_d\rho|v|^3A_{front} \tag{4.3}$$

$$P_g = mg\sin theta|v| \tag{4.4}$$

$$P_{accel} = ma|v| \tag{4.5}$$

Theses formulas were used in Simulink to derive the required power of the go-kart motor from the speed profile, as shown in Figure 4.4. The same speed profile is used to determine the acceleration, that is used in the calculations. The parameters required to solve these equations are given in Table 4.2.

Table 4.2: Parameters go-kart for power calculation.

Parameter	Value
Mass (m)	270 kg
Gravitational acceleration (g)	9.81 $\frac{m}{s}$
Coefficient of rolling resistance (C_{rr})	0.015 [48]
Coefficient of drag (C_d)	0.804 [49]
Frontal Area (A_{front})	0.57484 m_2 [49]

Regenerative braking

The present model is not equipped with regenerative break, even though the design allows for this to be implemented. As this is not part of the study it was not considered. However, it is common knowledge that regenerative breaking reduces the required battery size and this should be carefully consider before construction of the go-kart. For now it helps to setup the 'worst-case-scenario' and see if the go-kart could preform without these addition features.
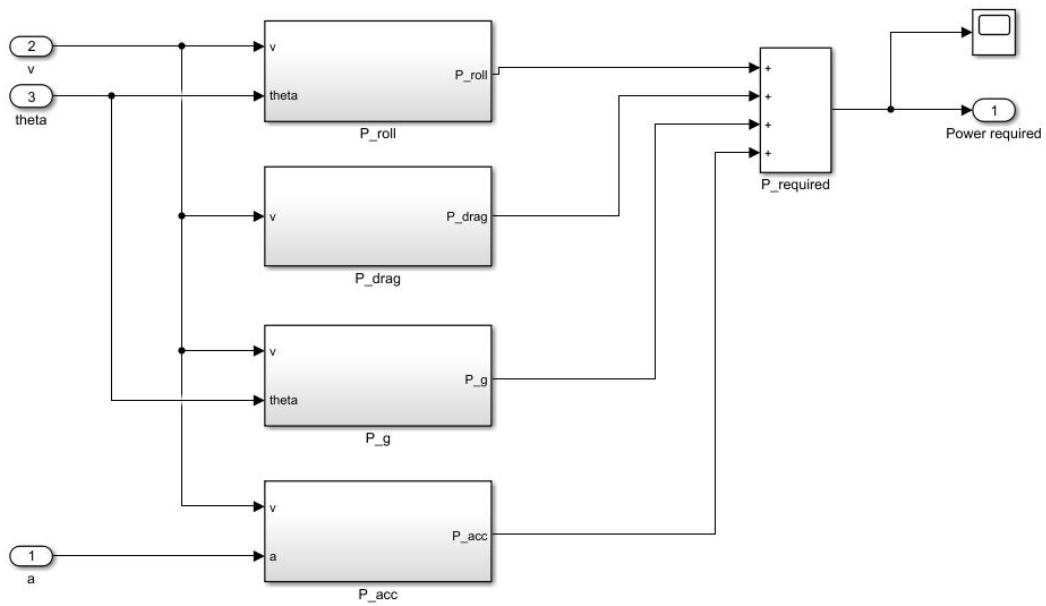
Figure 4.4: Power requirement simulation.

4.3.2 Battery modeling

The modeling of the battery is done to check whether the levels remain within the manufacturers limits. For most lithium-ion batteries the upper limit is set at 95% SOC and the lower limit is set 20% SOC. The initial values of the battery-pack for the simulation of the electric go-kart without the charger and the large battery-pack are shown in Table 4.3:

Table 4.3: Setting of battery-pack.

Parameter	Value
Initial SOC	0.95 %
Battery capacity	4 kWh

For the modeling of the battery, a lithium-ion model from Simulink was initially used; that requires current as an input and returns both SOC and voltage as output. However, as the battery becomes smaller due to the addition of the charger and the cells that build up the battery-pack remain the same, the peak power drawn from the battery becomes to large and shuts down the simulation.
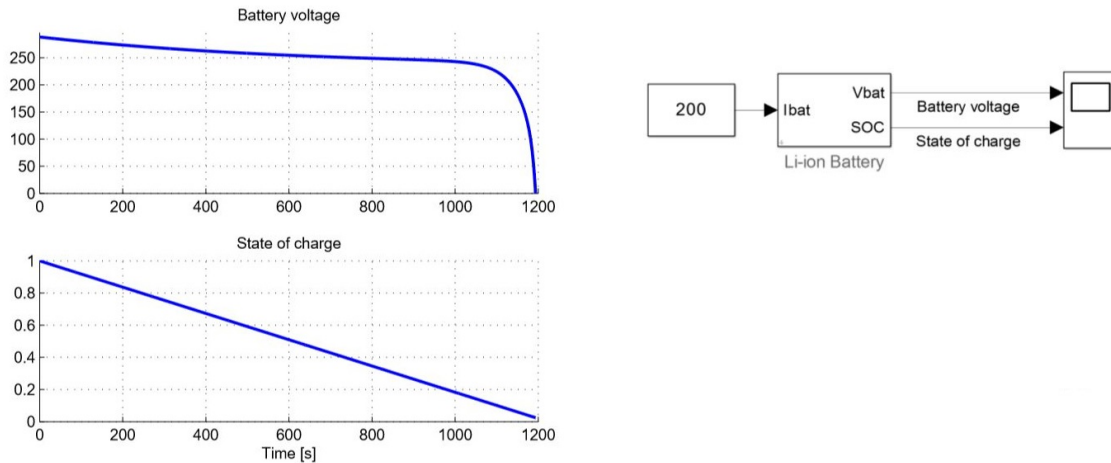
Figure 4.5: Lithium-ion battery-pack Simulink.

This problem can be overcome by the use of power electronics, but designing the right converter is out of the scope of this study. Therefore, a simpler approach was chosen were the required power is integrated to determine the energy requirement; the assumption of this linear behaviour is valid as long as the SOC does not go under 20%, as can be seen from the Lithium-ion model in Figure 4.5.

The energy requirement was corrected by the power electronics efficiency and then added to the energy of the battery-pack. The charger in the model is automatically switched off if the SOC becomes higher than 95%. It also has a protection against deep discharging that stops the simulation if the SOC becomes lower than 20%.

4.3.3 Power receiver modeling

For the modeling of the power transferred by the IPTS, two situations should be considered: stationary charging and dynamic charging.

Stationary charging

For the stationary charging a good alignment was assumed; the misalignment between charger was assumed to be below 50 mm in all directions,due to the guiding rails and wheel-pits in the pit lane. The time between heats was assumed to be 5 min; this time is required to switch drivers. This is the only time that the stationary charging takes place and it is required to replenish the battery to a SOC of 95%, otherwise continuity can not be assumed. It is assumed that the battery-pack can be charged at the rate of the power output of the charger.

The modeling of this situation was done by switching to the stationary charger at the end of the dynamic part. The simulation time was lengthened by t_{stat}, that equals 5 minutes. The stationary charger assumed the minimal power transfer for the prescribed misalignment. However, due to the small misalignment the power transfer is very high during this charging situation. The alignment provides both proper shielding and high efficiency. Figure 4.6 shows the power transfer is this region.

Dynamic charging

In the dynamic charging case the speed profile from the testing was used to first determine the location on the track. By integrating the speed, the position in x-direction was determined. The location of the go-kart with respect to the next primary coil was then determined. The misalignment scalar was then inserted in a 2D look-up table, that contained the data from the power calculation from Chapter 2. The look-up table then determined the power transferred from the transmitter to the receiver.
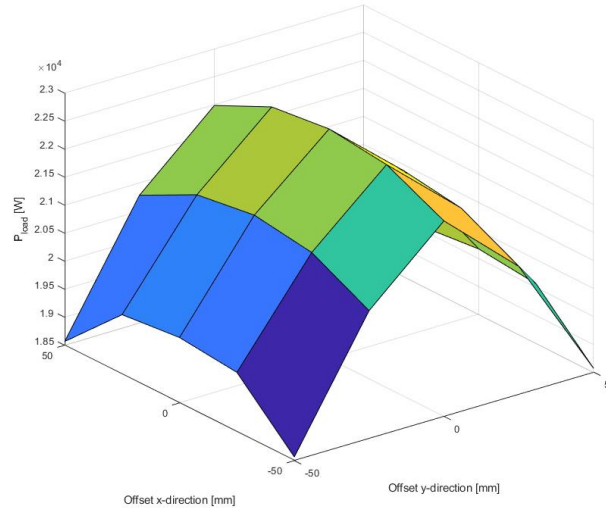
Figure 4.6: Power transfer on stationary coils within the limited alignment.

4.3.4 Losses modeling

In the modeling of Simulink some assumptions had to be made. However, to achieve a model that represents the reality as close as possible losses were assumed for all different stages of power conversion. The losses were represented in Simulink as a gain, that reduces the power out of the receiver and enlarges the required energy delivered by the battery-pack.

Losses in electric motor

Electric motors have different losses depending on their use. A motor being driven at constant speeds will be far more efficient that a motor that is used to accelerate. The electric motor that was chosen has a 92% efficiency in the working range of 24-72 VDC. Therefore, a assumed overall efficiency of 90% will be assumed. Before production the exact electric motor can be modeled and put into the simulation to more accurately determine the power usage of the system.

Losses in power electronics

The power electronics that are used to convert the power in the system are of relative high efficiency but should be considered none the less. For a converter stage a 98% efficiency was assumed, as exact modeling is only important in the final design and will differ only slightly from this assumption.

Losses in receiver

The losses in the receiver are already considered in the Simulink model, that determined the maximum power output of the IPTS. As the mutual coupling analysis from COMSOL was performed with all shielding and flux guidance in place, the losses are inherently considered in the design. These losses are the following:

- Aluminum losses
- Copper losses
- 3C94 ferrite losses

The losses in the aluminum shielding are due to the eddy currents, that create an opposing Electromagnetic Field (EMF) to counteract the changing magnetic field. The copper losses are due to the Alternating Current (AC) resistance in the coils and the ferrite losses are due to the friction caused by the rotation of the field aligning particles in the material. All losses could be determined individually but are of relative low importance to the feasibility of the system, as they are accounted for in the COMSOL simulation.

4.3.5 Final simulation

In order to determine the effect that the IPTS has on the battery-pack, a benchmark was set by implementing a purely battery powered go-kart –Battery Electric Vehicle (BEV)– in the Simulink model. Several battery-pack sizes were simulated and the resulting SOC of each simulation is shown in Figure 4.7. The mass of the go-karts was adapted according to the size of the chosen battery-pack.
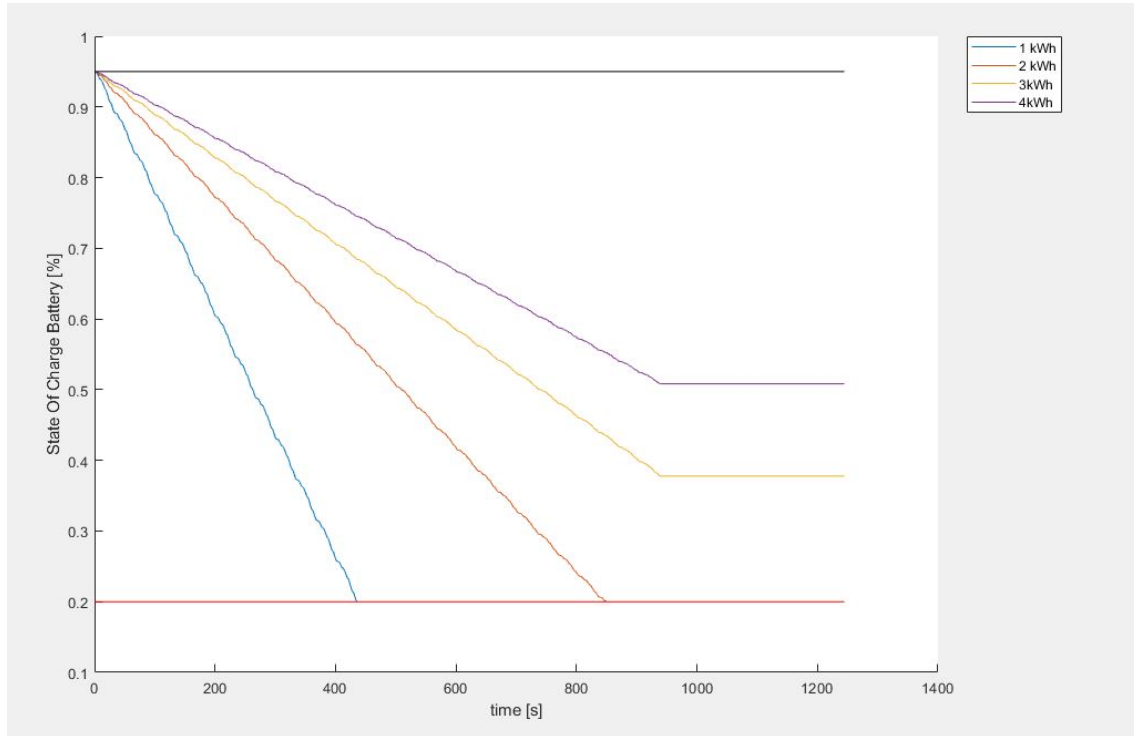

Figure 4.7: Benchmark SOC simulation for different battery-pack sizes(without charger).

The graph shows that a battery-pack smaller than 3 kWh is unable to complete a 15 minute heat on the track. As there is no automatic recharging on these go-kart, and swapping out 20 battery-packs –along with switching drivers– would be impractical within 5 minutes, a secondary fleet would be required. Staff would have to ensure that drivers are seated and all go-kart are connected and fully charged within these 20 minutes. These problems can be overcome by the IPTS as it automatically charges the go-kart in the pit-lane.

To investigate the impact of the IPTS on the SOC of the battery-pack, three simulations for a go-kart with IPTS on the same track were conducted, namely:

- Charger off
- Maximum power output
- Minimum power output

The first is to determine the impact of the weight of the charger on the state of charge, the other two will help show the maximum and minimum SOC of the go-kart at the end of a heat. The size of the battery-pack was adjusted to 2 kWh and the weight of the different components and the total mass of the go-kart are shown in Table 4.4 for comparison.

Table 4.4: Masses of both powering systems.

Electrical component	Battery powered go-kart	IPTS go-kart
Power electronics	4 kg	4 kg
Electric motor	16.47 kg	16.47 kg
Battery-pack	40 kg	20 kg
IPTS receiver	0 kg	20 kg
Total	60.47 kg	60.47

Once the simulation was completed, the minimal power-output –occurring at the lateral limit of 250 mm– turned out to be insufficient. The power-map already showed that this would be a critical point, as the power-output drastically drops at this point. Therefore, another simulation was conducted that shows the result of the next lowest power-output. The results are shown in figure 4.8.
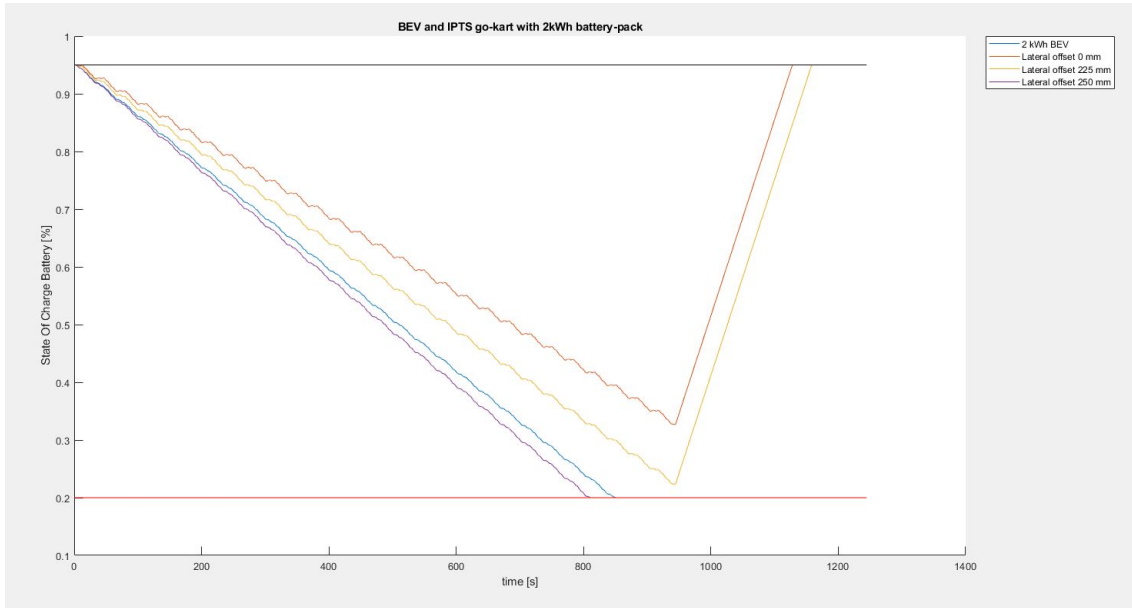

Figure 4.8: Impact of IPTS on SOC for different offsets(BEV benchmark included).

The graph shows that the charger is able to deliver the required amount of power, if a smaller limit is selected. This can be done by slightly widening the pick-up coils or placing a extra set of transmitters in the width of the track. Considering the cost of adding another set of transmitters, the option of widening the coil is the preferred option. The design of the coil might have to be slightly alternated to be able to fit on a go-kart. For the cost analysis this options was assumed to be feasible as the difference between the designed coil and the desired coil is small.

4.4   Cost analysis

Cost is a important factor in the determination of the feasibility of the system; therefore, the total cost of the system is analyzed and compared to both electric go-karts and fossil fuel go-karts. The cost is split in several sections as it depends on the track, a longer tracks requires more primary coils. However, the methods used for determining these costs can be used on all tracks.

In the calculation for the optimal power transfer design, the weight of the receiver is considered the most important factor. However, cost could also be used to determine the optimal design as it can have a significant effect on the total cost of the system. Especially, in systems with large amount of primary coils. For now, the feasibility is the most important factor and this is strongly related to the weight of the go-kart.

Table 4.5: Estimated cost of material per kg.

Material	Cost
Aluminum [50]	€8,-/kg
Ferrite 3C94 [51]	€20,-/kg
Litz-Wire [1]	€35,-/kg
PVC	€6,-/kg
Lithium-ion battery [52]	€6,-/kWh

First, the cost of the materials needed for the construction of a single transmitter/receiver are determined. These cost are straight forward and only allow for little variation. The estimated cost of the materials are shown in Table 4.5. As these estimated are dependent on several factor, variations might be applicable.

Secondly, the cost of labour for construction and installation was estimated;based on literature. Finally, the cost of the case study were compared to both BEV and ICE powered go-karts.

All cost were applied to the case study; that requires 20 go-karts –receivers– and 970 transmitter-sets. The maximum lateral coverage of the chargers –500 mm– and the track-width in the charging sections –5000 mm– set a requirement of 10 transmitter in the width of the track. The amount of transmitters that fits into a 1 meter along the track is exactly 1. Therefore, the number of transmitter-sets per 97 meter of track is 970.

Table 4.6: Case-study requirements of IPTS.

Component	Number required
Receiver	20
Transmitter-sets	970

4.4.1 Receiver cost

The cost of a single receiver –that consists of two poles– is comprised from the material and construction cost of a receiver. The total cost for a receiver and the cost of the case-study are shown in Table 4.7:

Table 4.7: Total cost of a single receiver.

Material cost	Construction cost	Cost per receiver
€537	€400	€937

Material cost receiver

The receiver is composed out of 4 elements; the aluminum shield, the aluminum rim, the ferrite, the Litz-wire and the plastic cover(rigid PVC). Table 4.8 shows the different materials used in the construction of the receiver. All cost were estimated from the weight of the material, using prices of finished product rather than raw material prices; that is much lower as it needs processing. The average cost per m^3 of the material was determined and adapted to the required amount. As all materials have simple forms no addition cost will be expected when large volumes are ordered to these custom requirements. The cost of the additional shielding is not considered in this calculation, as it will be such a small percentage of the cost.

Table 4.8: Weight and cost of receiver.

Receiver components	Weight/receiver	Cost/receiver
Aluminum shield (1020x600x4mm)	7.8 kg	€62
Aluminum rim (16x10x3800mm)	1.6 kg	€12
Extended shielding	0 kg	€0
Ferrite 3C94	7.6 kg	€152
Litz-wire	8.7 kg	€305
PVC cover	1 kg	€6
Total	26.7 kg	€537

Construction cost receiver

For the construction of the receiver, several steps are required. The rim needs to be cut into the right sizes and then attaching it to the shield, along with the ferrite. The attachment and connection of the Litz-wire will be the most labour intensive part of the system. Once complete, the receiver needs to be fitter with the plastic cover and attached to the go-kart. The entire process is estimated to take a 8 hour working day, for which a labour cost of €50,- an hour is estimated; resulting in a labour cost of €400,- for every receiver.

Electrical components cost go-kart

The cost of the other components required to drive the go-kart and convert the power on the side of the go-kart are shown in Table 4.9.

Table 4.9: Weight and cost electrical components IPTS go-kart.

Electrical component	Weight	Cost
Power electronics	4 kg	€1100 [53]
Electric motor	16.5 kg	€762 [54]
Battery-pack	16 kg	€3000 [52]
Total	36.5 kg	€4862

4.4.2 Transmitter track cost

The cost of a single transmitter-set -that consist of two poles- and the total amount of transmitters required for the track are shown in Table 4.10:

Table 4.10: Total cost of a pair of transmitters.

Material cost	Construction cost	Installation cost	Cost per transmitter
€165.9	€100	€100	€365.9

Material cost transmitter

The material cost of the transmitter is calculated in the same way as the receiver. For every transmitter a box enclosing a pole pair was reviewed. As all poles need to be connected a third of the Litz-wire weight was added to ensure enough is present to secure this connection between boxes.

Table 4.11: Material cost of a transmitter pair.

Receiver components	Weight/receiver	Cost/receiver
Aluminum shielding	9.3 kg	€74.4
Ferrite 3C94	8.1 kg	€162
Litz-wire transmitter	1.6 kg	€56
Litz-wire connector	0.5 kg	€17.5
Total	19.5 kg	€309.9

For the calculations the s-shaped geometry of the literature was used. However, with just a small optimization of the transmitter, cost can be reduced substantially. The height of the ferrite is required to fit this coil-width and can thus be lowered to the coil-width. The thickness of the base ferrite could be lowered by placing small additional ferrite slabs at placed where the magnetic flux density requires it. The width of the ferrite could also be lowered to reduce the amount of ferrite that is used.
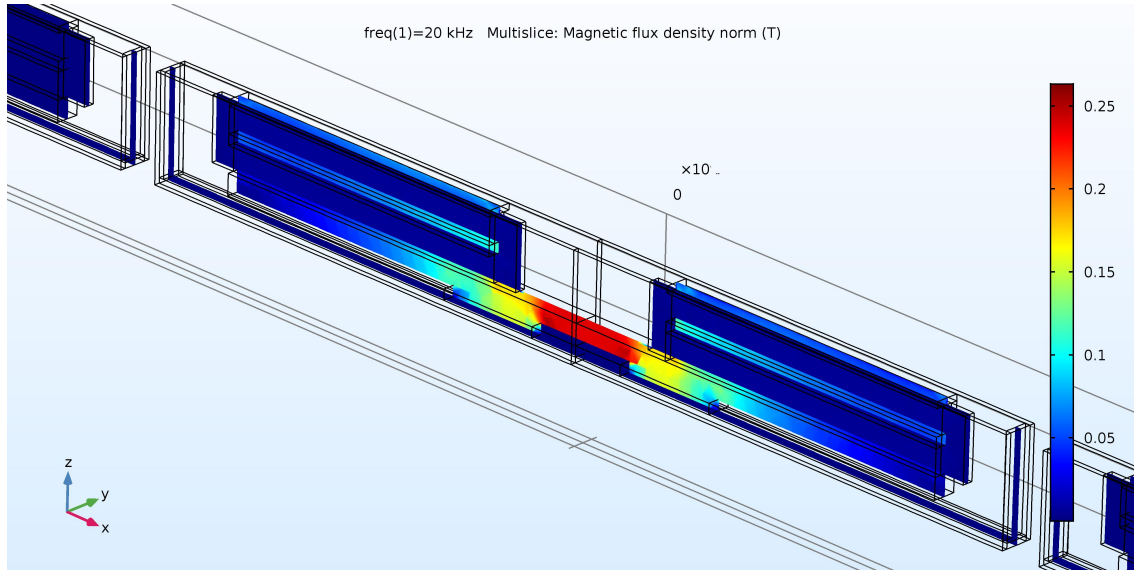
Figure 4.9: Transmitter after optimization.

Table 4.12: Material cost of an optimized transmitter pair.

Receiver components	Weight/receiver	Cost/receiver
Aluminum shielding	2.8 kg	€22.4
Ferrite 3C94	3.5 kg	€70
Litz-wire transmitter	1.6 kg	€56
Litz-wire connector	0.5 kg	€17.5
Total	8.4 kg	€165.9

The reduction of ferrite also causes the amount of aluminum to be decrease as well, as the overall size of the transmitter is reduced. The mutual coupling is lowered by 10%, but a simulation for the scaled power shows that the system is still able to ensure enough power is transferred, despite the fact that less ferrite is used in the transmitter. The resulting s-shaped transmitter is shown in figure 4.9. It shows how optimization is still of great importance for a final design.

Construction cost transmitter

The construction of the transmitter is estimated to take about 2 hours, considering that less construction is required due to the low complexity and number of working steps. The large volumes also allows for more efficient construction-time. The same hourly-rate of €50,- was applied. This puts the construction cost at €100,- per transmitter pair.

Installation cost transmitter

The installation cost of the transmitters are hard to estimate, as this heavy relies on the amount of transmitter that need to be installed and the complexity of the installations. However, literature estimates about €100.000,- per kilometer [53]. Considering that for every meter a single pair is installed, the average installation cost per transmitter-sets will be €100,-. The total length of the installation required is 1000 meters.

4.4.3 Electrical components cost transmitter

As the assumption was made that every set of poles was able to be activated only when its was covered by a go-kart, the requirement of actively turning on every transmitter arises. Even though this activation procedure is far beyond the scope of this thesis, an estimation of its cost is required. The results of this estimation were added to the total cost of the system to make a fair comparison with the other options.

When large enough, the inverter can supply power to all transmitters in each grid, by coupling them in series. More likely, a few inverter will used to power different section. The price of inverter is usually assumed to be linearly linked with its rated capacity, making the estimation easier. The 20 go-karts can be charged at 22kW each, making the maximum power required by the system 440 kW; when all chargers are activated to the maximum capacity. The estimated price for converters per kW is €50 [53],-. Rounding the maximum power output up to 600 kW, the total cost of the converters for the primary side is estimated at €30.000,-.

The primary coils should also be able to switch on and off. For every coil a switching box was used with an estimated cost of €50,- per switching box. For the case-study this would entail a total cost of €48.500,-. Other options to activate the appropriate transmitter could also be considered, as this method is quite expensive.

4.4.4 Total cost IPTS go-karts

The total cost of all the components are summed in Table 4.13. The cost of the system is quite high, mainly due to the large amount of transmitters that are required. A lower amount of transmitter is not possible, as the system will then not provide enough power to the go-kart for it to be able to substantially diminish the required battery-pack. Clever placements of the charger could lower the required amount of charger but this should be studied further before any conclusion regarding this could be drawn.

Table 4.13: Total cost of an IPTS on go-karts in the case-study.

Component of IPTS	Cost
Transmitters	€354923
Receivers	€18740
Electrical components go-kart	€97240
Electrical components primary	€78500
Total cost	€549403

4.5 Weight and cost comparison

For the comparison with rental go-kart of other powering methods, Table 4.14 shows the weight and price of the different powering methods. This table is constructed from the total cost of the case-study, that contains 20 go-karts and 970 transmitters.

The cost of the frame and all non-driving components are assumed to be €5.000,- in all cases. The cost of the ICE is assumed to be €1000,-. The weight of the go-kart frame and all non-powering components is assumed to be 125 kg.

Table 4.14: Weight and cost comparison of powering methods on a go-kart.

Type of power system	Powering system weight	Total cost case-study track
ICE go-kart	30 [kg]	€120.000,-
BEV	60.5 [kg]	€339.227,-
IPTS go-kart	63.2 [kg]	€549.403,-

As can be seen from the table, the initial investment is substantially higher for the IPTS, predominantly caused by the large number of transmitter that are required. The weight is still in the same range as the BEV. The shield of the receiver is accountable for the majority of the weight and reducing can be done fairly easy with the use of composites, considering that the thickness of the shield is of little influence of the EMF around the receiver.

4.6   Conclusion

The case study performed in this section has shown that for an IPTS with a coverage of 25% the size of the battery can be reduced by dynamic charging. However, the total initial investment of the system is substantially larger than other systems, due to the great number of transmitters that are required. Most of these transmitters will hardly ever be activated, as they are simply too far from the racing-line. Therefore, the system is not feasible in its current form, as the cost of the system is simply too high. However, a better placing of the transmitter could result in a more cost-effective system, that can be used to reduce the battery-size and charging problem of electric go-karts.

Even-though the initial investment cost of the system is much higher than a purely battery powered system, other cost will be reduced due to the implementation of an IPTS. These cost fall outside the initial investment, but could have a large impact on operational cost. For one, there is no requirement for staff to connect and disconnect all charger in 20 minutes, while also ensuring that all drivers are properly seated and overseeing the track. This means that one person can oversee the track during racing and the switching of driver in between heats, whereas this would require at least two persons when using BEV's. Another cost advantage is the reduced battery-pack; that is less expensive to replace due to its smaller size.

Compared to conventional ICE go-karts systems the initial investment cost are substantially higher. However, considering the growing awareness on global warming of the public, this would be an investment that is greener and thus more future proof. This green label can be used in marketing to attract more customers. Also, regulations on exhaust gasses are expected to become stricter in coming year in all industries and the impact of this should not be under estimated.

The added weight of the receiver eliminates the advantage gained by the reduction in battery-size. However, this IPTS was based on a charger designed to transfer power at 200 mm; which means that the optimization for such a charger is likely to reduce the weight of the receiver as well. As this is not in the scope of this study this is not further investigated, but some simple simulations with varying primary coil length suggest that this is possible. This is related to the effective area of the charger and the required pole distance.

This case study has shown that a track wide implementation of an IPTS on go-karts could reduce the battery-size of electric go-karts even in a basic setup, while ensuring the safety of both public and staff. Optimization of the system could increase the impact of these charger, while reducing the total weight receiver and cost of the entire system even further. However, current cost calculations result in a initial investment that is much higher than other systems. This could be resolved by more clever placement of the chargers, as these account for the largest portion of the cost; although most of the will almost never be activated.

Chapter 5

Conclusion and recommendations

5.1 Conclusion

This study shows that the use of an Induction Power Transfer System (IPTS) on a go-kart is not feasible in its current form, which requires 25% of the area of the track to be covered with chargers. However, the lack of feasibility is only due to cost; as its technical feasibility is proven. Optimizing of the system could significantly reduce the amount of charger and thus cost. This would make the system not only feasible, but even competitive in the go-kart industry.

A system was designed that enables required driving capability in electric go-karts without adding weight to Battery Electric Vehicle (BEV) go-karts. Further optimization is required to reduce the weight of the receiver –and thus go-kart– and the cost of the system. When compared to the current electrical go-kart, that requires a larger battery-pack, some important benefits can be gained from the implementation of an IPTS. First, there is no longer a requirement for labour-intensive swaps of either go-karts or battery-packs, as charging in the stationary setting is done automatically. Furthermore, the maintenance cost of the battery-packs can be greatly reduced. The smaller battery-packs used in the IPTS will be far cheaper to replace when it has reached the end of its life-cycle, due to their smaller size. These battery-packs represent a large portion of the cost of an electric go-kart and reducing them will add to the sustainability of a go-kart track.

Another important comparison for this study was how the weight of the go-kart with an IPTS would relate to the weight of an go-kart using an Internal Combustion Engine (ICE); which is currently the industry standard. These go-karts already have the capability to run continuously; due to the high energy density of fossil fuels and the short time required for refilling. The weight of the power unit is increased, from 30 kg for an ICE to 63.5 kg for an IPTS, which is slightly higher than the fully electric go-kart –60.5kg–. Optimization of the receiver should be done, to reduce the weight of the receiver, that account for the largest portion of the weight. As this study was done without much optimization, a lighter version is probably achievable; whereas the weight of the ICE is not likely to be reduced, considering it is in a more mature state of development. However, it is unlikely to be able to compete with an ICE power-train when it comes to weight.

The conversion to electric go-karts eliminates the exhaust gasses, which is especially beneficial for indoor go-kart tracks. It also reduces the maintenance-requirements on the motor, as this is even less for electrical motors than for an ICE. However, the initial investment for the installation and construction of the IPTS with its power electronics is much higher than the BEV option at this point. This needs to be significantly reduced before implementation would become cost-effective. The width of the track makes the system very costly and most charger will not be used due to the desire of drivers to drive the racing-line. Therefore, a more cost efficient system should be developed in which individual tracks are analyzed for this behaviour.

The results from this study shows that the system is technically achievable, but not very cost-effective without optimization. The system is shown to be able to reduce the size of the battery-pack, while keeping the same range. However, it was also shown that optimization could influence the outcome of this cost tremendously and it should, therefore, be further investigated.

5.2 Recommendations

In future studies, the track-patrons of go-karts should be investigated to determine the optimal placement of the charger, as this can result in a more affordable system. This might require track segments that force drivers in much more narrow charging sections or boost-strips. Also creating slower track sections could help diminish the required amount of charger. This would have the greatest impact on the total cost of the system and make it more competitive in the go-kart industry.

Furthermore, a more detailed optimization of the IPTS components and the controlling of the primary coil activation has to be studied. As these were not in the scope of this study, some assumption were made; these need to be studied in detail before the construction of such a system can be considered. For the components this could result in an even more efficient and lower costing system. However, the excitation of the primary coils is the most important, as this is a requirement for the Electromagnetic Field (EMF) to stay within the required limits set by the International Commission on Non-Ionizing Radiation Protection (ICNIRP).

Another important aspect to study is the effective area ratio and optimal pole distance for transmitters at this close proximity, as this could very well result in an even more efficient and light-weight system. This is far beyond the scope of this study, as it goes into the actual magnetic field construction by coils, but could also reduce cost substantially. Moreover, the optimal design of components in both receiver and transmitter should be studied. A reduction in the materials used in transmitters reduces the total initial investment of the system as the amount of transmitters is so large. All reduction in weight in the receiver gives the system an advantage over BEV go-karts as weight is an important aspect in racing go-karts.

Bibliography

[1] S. Chopra and P. Bauer, "Driving Range Extension of EV With On-Road Contactless Power Transfer #x2014;A Case Study," *IEEE Transactions on Industrial Electronics*, vol. 60, pp. 329–338, Jan. 2013.

[2] Honda, "https://engines.honda.com/models/model-detail/gx270," 2018. https://engines.honda.com/models/model-detail/gx270.

[3] S. Chopra and P. Bauer, "Analysis and design considerations for a contactless power transfer system," in *2011 IEEE 33rd International Telecommunications Energy Conference (INTELEC)*, pp. 1–6, Oct. 2011.

[4] Wikipedia, "https://en.wikipedia.org/wiki/transformer," 2018. https://en.wikipedia.org/wiki/Transformer.

[5] M. Yilmaz, V. T. Buyukdegirmenci, and P. T. Krein, "General design requirements and analysis of roadbed inductive power transfer system for dynamic electric vehicle charging," in *2012 IEEE Transportation Electrification Conference and Expo (ITEC)*, pp. 1–6, June 2012.

[6] J. Kim, J. Kim, S. Kong, H. Kim, I. S. Suh, N. P. Suh, D. H. Cho, J. Kim, and S. Ahn, "Coil Design and Shielding Methods for a Magnetic Resonant Wireless Power Transfer System," *Proceedings of the IEEE*, vol. 101, pp. 1332–1342, June 2013.

[7] Wikipedia, "https://en.wikipedia.org/wiki/skin_effect," 2018. https://en.wikipedia.org/wiki/Skin_effect.

[8] circuitglobe, "https://circuitglobe.com/proximity-effect.html," 2018. https://circuitglobe.com/proximity-effect.html.

[9] C. R. Sullivan, "Optimal Choice for Number of Strands in a Litz-Wire Transformer Winding," *IEEE TRANSACTIONS ON POWER ELECTRONICS*, vol. 14, no. 2, p. 10, 1999.

[10] electronics tutorials, "https://www.electronics-tutorials.ws/electromagnetism/magnetic-hysteresis.html," 2018. https://www.electronics-tutorials.ws/electromagnetism/magnetic-hysteresis.html.

[11] K. Knaisch and P. Gratzfeld, "Comparison of magnetic couplers for inductive electric vehicle charging using accurate numerical simulation and statistical methods," in *2015 5th International Electric Drives Production Conference (EDPC)*, pp. 1–10, Sept. 2015.

[12] A. Zaheer, D. Kacprzak, and G. A. Covic, "A bipolar receiver pad in a lumped IPT system for electric vehicle charging applications," in *2012 IEEE Energy Conversion Congress and Exposition (ECCE)*, pp. 283–290, Sept. 2012.

[13] K. Knaisch, M. Springmann, and P. Gratzfeld, "Comparison of coil topologies for inductive power transfer under the influence of ferrite and aluminum," in *2016 Eleventh International Conference on Ecological Vehicles and Renewable Energies (EVER)*, pp. 1–9, Apr. 2016.

[14] M. Budhia, G. A. Covic, J. T. Boys, and C. Y. Huang, "Development and evaluation of single sided flux couplers for contactless electric vehicle charging," in *2011 IEEE Energy Conversion Congress and Exposition*, pp. 614–621, Sept. 2011.

[15] Wikipedia, "https://en.wikipedia.org/wiki/volt-amperereactive," 2018. https://en.wikipedia.org/wiki/Volt-amperereactive.

[16] B. power, "http://electricalsynergy.edublogs.org/2015/11/30/knowledge-of-power-is-power/." http://electricalsynergy.edublogs.org/2015/11/30/knowledge-of-power-is-power/.

[17] C.-S. Wang, O. H. Stielau, and G. A. Covic, "Design considerations for a contactless electric vehicle battery charger," *IEEE Transactions on Industrial Electronics*, vol. 52, pp. 1308–1314, Oct. 2005.

[18] B. Peschiera and S. S. Williamson, "Review and comparison of inductive charging power electronic converter topologies for electric and plug-in hybrid electric vehicles," in *2013 IEEE Transportation Electrification Conference and Expo (ITEC)*, pp. 1–6, June 2013.

[19] J. L. Villa, J. Sallan, J. F. S. Osorio, and A. Llombart, "High-Misalignment Tolerant Compensation Topology For ICPT Systems," *IEEE Transactions on Industrial Electronics*, vol. 59, pp. 945–951, Feb. 2012.

[20] ICNIRP, "Guidelines for limiting exposure to time-varying electric and magnetic fields (1 Hz to 100 kHz)," *Health physics*, vol. 99, no. 6, pp. 818–836, 2010.

[21] ICNIRP, "Guidelines for limiting exposure to time-varying electric and magnetic fields (up to 300 MHz)," *Health physics*, vol. 74, no. 4, pp. 494–522, 1998.

[22] N. Kuyvenhoven, C. Dean, J. Melton, J. Schwannecke, and A. E. Umenei, "Development of a foreign object detection and analysis method for wireless power systems," in *2011 IEEE Symposium on Product Compliance Engineering Proceedings*, pp. 1–6, Oct. 2011.

[23] M. Budhia, J. T. Boys, G. A. Covic, and C. Y. Huang, "Development of a Single-Sided Flux Magnetic Coupler for Electric Vehicle IPT Charging Systems," *IEEE Transactions on Industrial Electronics*, vol. 60, pp. 318–328, Jan. 2013.

[24] D. Bululukova and M. Kramer, "Application of existing wireless power transfer standards in automotive applications," in *2014 International Conference on Connected Vehicles and Expo (ICCVE)*, pp. 863–864, Nov. 2014.

[25] D. v. Wageningen and T. Staring, "The Qi wireless power standard," in *Proceedings of 14th International Power Electronics and Motion Control Conference EPE-PEMC 2010*, pp. S15–25–S15–32, Sept. 2010.

[26] "Wireless power transfer for light-duty plug-in/electric vehicles and alignment methodology (J2954 ground vehicle standard) - SAE Mobilus." https://saemobilus.sae.org/content/J2954_201711/.

[27] S. Jeong, Y. J. Jang, and D. Kum, "Economic Analysis of the Dynamic Charging Electric Vehicle," *IEEE Transactions on Power Electronics*, vol. 30, pp. 6368–6377, Nov. 2015.

[28] G. A. Covic and J. T. Boys, "Modern Trends in Inductive Power Transfer for Transportation Applications," *IEEE Journal of Emerging and Selected Topics in Power Electronics*, vol. 1, pp. 28–41, Mar. 2013.

[29] J. Huh, S. W. Lee, W. Y. Lee, G. H. Cho, and C. T. Rim, "Narrow-Width Inductive Power Transfer System for Online Electrical Vehicles," *IEEE Transactions on Power Electronics*, vol. 26, pp. 3666–3679, Dec. 2011.

[30] S. Y. Choi, B. W. Gu, S. Y. Jeong, and C. T. Rim, "Advances in Wireless Power Transfer Systems for Roadway-Powered Electric Vehicles," *IEEE Journal of Emerging and Selected Topics in Power Electronics*, vol. 3, pp. 18–36, Mar. 2015.

[31] C. Park, S. Lee, S. Y. Jeong, G. H. Cho, and C. T. Rim, "Uniform Power I-Type Inductive Power Transfer System With DQ-Power Supply Rails for On-Line Electric Vehicles," *IEEE Transactions on Power Electronics*, vol. 30, pp. 6446–6455, Nov. 2015.

[32] S. Y. Choi, S. Y. Jeong, B. W. Gu, G. C. Lim, and C. T. Rim, "Ultraslim S-Type Power Supply Rails for Roadway-Powered Electric Vehicles," *IEEE Transactions on Power Electronics*, vol. 30, pp. 6456–6468, Nov. 2015.

[33] O. C. Onar, J. M. Miller, S. L. Campbell, C. Coomer, C. P. White, and L. E. Seiber, "A novel wireless power transfer for in-motion EV/PHEV charging," in *2013 Twenty-Eighth Annual IEEE Applied Power Electronics Conference and Exposition (APEC)*, pp. 3073–3080, Mar. 2013.

[34] X. Zhang, Z. Yuan, Q. Yang, Y. Li, J. Zhu, and Y. Li, "Coil Design and Efficiency Analysis for Dynamic Wireless Charging System for Electric Vehicles," *IEEE Transactions on Magnetics*, vol. 52, pp. 1–4, July 2016.

[35] J. Huh, W. Lee, S. Choi, and C. Rim, "A new cross-segmented power supply rail for roadway powered electric vehicles," in *2012 3rd IEEE International Symposium on Power Electronics for Distributed Generation Systems (PEDG)*, pp. 291–296, June 2012.

[36] C. Fernandez, O. Garcia, R. Prieto, J. A. Cobos, S. Gabriels, and G. V. D. Borght, "Design issues of a core-less transformer for a contact-less application," in *APEC. Seventeenth Annual IEEE Applied Power Electronics Conference and Exposition (Cat. No.02CH37335)*, vol. 1, pp. 339–345 vol.1, 2002.

[37] J. d. Santiago, H. Bernhoff, B. Ekergård, S. Eriksson, S. Ferhatovic, R. Waters, and M. Leijon, "Electrical Motor Drivelines in Commercial All-Electric Vehicles: A Review," *IEEE Transactions on Vehicular Technology*, vol. 61, pp. 475–484, Feb. 2012.

[38] Wikipedia, "https://nl.wikipedia.org/wiki/lithium-ion-accu." https://nl.wikipedia.org/wiki/Lithium-ion-accu.

[39] G. A. J. Elliott, G. A. Covic, D. Kacprzak, and J. T. Boys, "A New Concept: Asymmetrical Pick-Ups for Inductively Coupled Power Transfer Monorail Systems," *IEEE Transactions on Magnetics*, vol. 42, pp. 3389–3391, Oct. 2006.

[40] digikey, "https://www.digikey.my/product-detail/en/ferroxcube/e25-13-11-3c94/1779-1019-nd/7041479," 2018. https://www.digikey.my/product-detail/en/ferroxcube/E25-13-11-3C94/1779-1019-ND/7041479.

[41] C. R. Sullivan and R. Y. Zhang, "Simplified design method for litz wire," in *2014 IEEE Applied Power Electronics Conference and Exposition - APEC 2014*, (Fort Worth, TX, USA), pp. 2667–2674, IEEE, Mar. 2014.

[42] X. Nan and C. R. Sullivan, "An equivalent complex permeability model for litz-wire windings," in *Fourtieth IAS Annual Meeting. Conference Record of the 2005 Industry Applications Conference, 2005.*, vol. 3, pp. 2229–2235 Vol. 3, Oct. 2005.

[43] *Centre of Advanced Study of the University Grants Commis-*.

[44] J. A. Ferreira, "Appropriate modelling of conductive losses in the design of magnetic components," in *21st Annual IEEE Conference on Power Electronics Specialists*, pp. 780–785, 1990.

[45] Wikipedia, "https://en.wikipedia.org/wiki/file:phosphene_artistic_depiction.gif," 2018. https://en.wikipedia.org/wiki/File:Phosphene_artistic_depiction.gif.

[46] S. Ahn, C. Hwang, and H. H. Park, "Optimized shield design for reduction of EMF from wireless power transfer systems," *IEICE Electronics Express*, vol. 11, no. 2, pp. 20130930–20130930, 2014.

[47] J. Larminie and J. Lowry, *Electric vehicle technology explained*. West Sussex, England ; Hoboken, N.J: J. Wiley, 2003.

[48] H. Wizard, "http://hpwizard.com/tire-friction-coefficient.html," 2018. http://hpwizard.com/tire-friction-coefficient.html.

[49] M. Biancolini, C. Del Bene, T. Larsson, and C. Groth, "Evaluation of go-kart aerodynamic efficiency using cfd, rbf mesh morphing and lap time simulation," *International Journal of Aerodynamics*, vol. 5, p. 146, 01 2016.

[50] aluminium op maat, "https://www.aluminiumopmaat.nl," 2018.

[51] magnetic applications, "http://www.magnetapplications.com/news/view/52/," 2018. http://www.magnetapplications.com/news/view/52/.

[52] all battery, "http://www.all-battery.com/tendura-48v-34215.aspx," 2018. http://www.all-battery.com/tendura-48v-34215.aspx.

[53] P. Venugopal, *Magnetic Energy Transfer in Roads*, ch. Economic Analysis of IPTS systems - a case study. 2018.

[54] eletric motorsport, "https://www.electricmotorsport.com/ev-parts/controllers/brushless-motor-controllers/sevcon-gen4-110-300.html," 2018. https://www.electricmotorsport.com/ev-parts/controllers/brushless-motor-controllers/sevcon-gen4-110-300.html.

Appendices

Appendix A

Power calculation aligned system

A.1 Optimization of winding geometry

```matlab
1  clear all
2  close all
3  clc
4  tic
5
6  %% Parameters
7  rho           = 1.68E-8;
8  f             = 20000;
9  omega         = 2*pi*f;
10 mu0           = pi*4E-7;
11 mu            = 0.999994;
12 Kf            = 0.4;
13 dens_cu       = 8950;
14 den_cur       = 5;
15 I_1           = 40;
16
17 %% Skindepth
18 [delta, r_strain]             = skindepth(f,mu,mu0,rho);
19
20 %% Power calculation
21
22
23 for i = 1:1:64
24
25     clear A
26     t = 1;
27     for sec_eff = 0.90:0.001:0.999
28     for pri_n = 1:1:20
29         G      = pri_geo_vfinal(den_cur,I_1,pri_n);
30         for h = 1:1:size(G,1)
31             h1 = G(h,1);
32             w1 = G(h,2);
33                 for w2 = 0.005:0.005:0.05
34                     for h2 = 0.005:0.005:0.01
35                         [P_load,eff_tot,den_cur_2,m_cu_1,m_cu_2] = ...
36                             ipts_cal(I_1,pri_n,w2,h2,w1,h1,sec_eff, ...
37                             delta,r_strain,rho,omega);
38                         if den_cur_2 <= 5 && eff_tot >0.60 && P_load>(i ...
39                             *1000)
40                             m_cu = 159*m_cu_1 + 20*m_cu_2;
41                             A(t,:) = [pri_n,P_load,eff_tot,m_cu,h1,w1,
```

```
                                    h2 , w2 , den_cur_2 , sec_eff ] ;
39                              t=t +1;
40                          end
41                      end
42                  end
43              end
44          end
45  end
46
47  [M, I ] = min (A( : , 4 ) ) ;
48  X( i , : ) = A( ( I ) , : ) ;
49
50  end
51
52
53  hold on
54  plot (X( : , 2 ) ,X( : , 4 ) , ' r+ ' )
55  xlabel ( ' P_{ load } [W] ' )
56  ylabel ( 'M_{cu} [ kg ] ' )
57  hold off
58
59  GEO =[X( : , 1 ) X( : , 5 ) X( : , 6 ) X( : , 7 ) X( : , 8 ) ] . ' ;
60
61  toc
```

A.2 Primary geometry determination

```
1  function [G] = pri_geo_vfinal ( den_cur , I , n )
2
3  Kf            = 0.4 ;
4  sig           = 3 ;
5  h_max         = 10;
6  w_max         = 50;
7  q             = 1 ;
8  A_single      = I /( Kf∗den_cur ) ;
9
10  h_single      = ceil ( sqrt ( A_single ) ) ;
11  w_single      = h_single ;
12
13  w             = w_single ∗n ;
14
15  if w <= w_max
16      G( q , : ) = [ h_single ,w ] ;
17      q = q + 1 ;
18  end
19
20
21  x = ceil ( ( A_single ∗n/h_max ) /5 ) ;
22  x = 5∗x ;
23  G( q , : ) = [ h_max , x ] ;
24  G = G∗10^−sig ;
25  end
```

A.3 Calculation of power-output for input parameters

```
1  function [ P_load , eff_tot , cur_den_2 , m_cu_1 , m_cu_2 ] = ipts_cal ( I_1 , pri_n ,
       sec_w , sec_h , pri_w , pri_h , required_eff , delta , r_strain , rho , omega )
2
```

```matlab
%% Parameters
Kf              = 0.4;
dens_cu         = 8940;


%coil 1
pri_ac          = 2;
pri_l           = 0.3;
height_fer      = 0.01;

%coil 2
sec_ac          = 2;
sec_n           = pri_n;
sec_l           = 0.5;

%Mutual inductance
M = ((sec_n/10)^2)*3.9567e-5;


%% Calculations
[pri_Astr, pri_Nstr]            = strain_det(pri_w, pri_h, pri_n, Kf, r_strain)
    ;
[sec_Astr, sec_Nstr]            = strain_det(sec_w, sec_h, sec_n, Kf, r_strain)
    ;

L1_av                           = 2*pri_l + pi*pri_w + 2*height_fer;
L2_av                           = 2*(sec_l-sec_w)+2*(0.58-sec_w);
L1_tot                          = L1_av*sec_ac;
L2_tot                          = L2_av*pri_ac;

[Rac_1,~]                       = R_ac(rho, L1_tot, delta, r_strain, pri_n,
    pri_Nstr, pri_Astr);
[Rac_2,~]                       = R_ac(rho, L2_tot, delta, r_strain, sec_n,
    sec_Nstr, sec_Astr);
R_L                             = required_eff/(1-required_eff)*Rac_2;

I_2                             = I_1*omega*M/(R_L+Rac_2);

cur_den_2                       = cur_den(sec_w, sec_h, sec_n, Kf, I_2);

Ploss_1                         = loss(I_1, Rac_1);
Ploss_2                         = loss(I_2, Rac_2);
P_load                          = loss(I_2, R_L);

m_cu_1                          = L1_av*pri_Astr*pri_Nstr*pri_n*dens_cu;
m_cu_2                          = L2_av*sec_Astr*sec_Nstr*sec_n*dens_cu;

eff_tot                         = P_load./(P_load+Ploss_1+Ploss_2);


end
```

Appendix B

Power calculation misaligned system

B.1 Analytic power-ouput calculation

```matlab
clc;
clear;

%% COMSOL parameters
data1 = xlsread('Lm_max','Blad1');

offset_x    = data1(:,1);
offset_y    = data1(:,2);
Lm_dat      = data1(:,4);
m           = length(data1);

%% Typical measurement
t        = 0.025;
N        = 12;
fs       = 20e3;
omega    = 2*pi*fs;
L1       = 109.8e-6;
L2       = 95.6e-6;
Cp       = 1/(L1*omega^2);
Cs       = 1/(L2*omega^2);
Lp       = L1 - Lm_dat(1);
Ls       = L2 - Lm_dat(1);


Ip               = 40;
required_eff     = 0.9860;
R1               = 0.0344;
R2               = 0.0485;
R1_cap           = 1e-6;
R2_cap           = 1e-6;
R_core           = 1e-6;


%% Power matrix
P = zeros(m,7);

%% SIMULATION

```

```matlab
39
40  a = 1;
41  b = m;
42
43    for i = a:b
44  tic
45  Lm              = abs(Lm_dat(i));
46  Max_p           = 0;
47
48
49  for R_o         = 10:-0.001:0.001
50  Z2              = R2 + R_o + 1j*(omega*(Ls+Lm_dat(i)) - 1/(omega*Cs));
51  Is              = abs(1j*Ip*Lm*omega/(Z2));
52  Power           = Is^2*R_o;
53  Eff             =(Is^2*R_o)/(Ip^2*R1 + Is^2*(R2+R_o));
54      if Is > 84
55          break
56      end
57      if Power > Max_p && Eff > 0.75
58          P(i-a+1,1) = offset_x(i);
59          P(i-a+1,2) = offset_y(i);
60          P(i-a+1,3) = Power;
61          P(i-a+1,4) = Ip;
62          P(i-a+1,5) = Is;
63          P(i-a+1,6) = Eff;
64          P(i-a+1,7) = R_o;
65      end
66  end
67
68  if P(i,3) == 0
69      P(i-a+1,1) = offset_x(i);
70      P(i-a+1,2) = offset_y(i);
71      P(i-a+1,3) = 0;
72      P(i-a+1,4) = 0;
73      P(i-a+1,5) = 0;
74      P(i-a+1,7) = 0;
75  end
76
77  toc
78  end
79
80
81  P_map_comp = vec2mat(P(:,3),sqrt(m));
82
83  P_quarter       = P_map_comp;
84  P1              = flipud(P_quarter);
85  P_right         = [P1;P_quarter];
86  P_left          = fliplr(P_right);
87
88  P_grid          = [P_left, P_right];
89
90  P_grid(:,length(P1)) = [];
91  P_grid(length(P1),:) = [];
92
93  x_max           = data1(end,1);
94  y_max           = data1(end,2);
95  x_step          = x_max/(sqrt(m)-1);
96  y_step          = y_max/(sqrt(m)-1);
```

```
97    offset_x      = [−x_max: x_step : x_max ];
98    offset_y      = [−y_max: y_step : y_max ];

99

100   surf ( offset_x , offset_y , P_grid )

101

102   x_data = [ data1 ( : , 1 );−data1 ( : , 1 ); data1 ( : , 1 );−data1 ( : , 1 ) ];
103   y_data = [ data1 ( : , 2 );−data1 ( : , 2 ); data1 ( : , 2 );−data1 ( : , 2 ) ];

104

105   matA = P_grid ( : ) ;
```

B.2   Simulink power-ouput calculation

```
1     clc ;
2     clear ;

3

4

5     %% COMSOL parameters
6     data1 = xlsread ( 'Lm' , 'Blad1 ' );
7     load ( 'R_analytical ' )

8

9     offset_x      = data1 ( : , 1 ) ;
10    offset_y      = data1 ( : , 2 ) ;
11    Lm_dat        = data1 ( : , 4 ) ;
12    m             = length ( data1 ) ;

13

14    %% Typical measurement
15    t         = 0.025;
16    N         = 12;
17    fs        = 20e3 ;
18    omega     = 2∗pi∗fs ;
19    Lp        = 109.8e−6−Lm_dat ( 1 ) ;
20    Ls        = 95.6e−6−Lm_dat ( 1 ) ;
21    Cp        = 1/((Lp+Lm_dat ( 1 ))∗omega^2) ;
22    Cs        = 1/((Ls+Lm_dat ( 1 ))∗omega^2) ;

23

24    Ip               = 40;
25    required_eff     = 0.9860;
26    R1               = 0.0344;
27    R2               = 0.0485;
28    R1_cap           = 1e−6;
29    R2_cap           = 1e−6;
30    R_core           = 1e−6;
31    %% Power matrix
32    P = zeros (m, 7 ) ;

33

34    %% SIMULATION

35

36    a = 1;
37    b = m;

38

39     for i = a : b
40     tic
41    Lm            = abs (Lm_dat ( i )) ;
42    R_o           = R( i , 1 ) ;
43        if R_o ==0
44            P( i , 1 ) = offset_x ( i ) ;
45            P( i , 2 ) = offset_y ( i ) ;
46            P( i , 3 ) = 0;
```

```matlab
47            P(i,4) = 0;
48            P(i,5) = 0;
49            P(i,6) = 0;
50            P(i,7) = 0;
51            P(i,8) = 0;
52             continue
53        end

54
55 % R_l            = ((pi^2)/8)*R_o-0.05;
56 for R_l = 3.1:0.1:4.1

57
58 Vdc = 501;
59 sim('circuit_simulation');
60 I_1           = max(Ip_measured)/sqrt(2);
61 I_2           = max(Is_measured)/sqrt(2);

62

63
64 while I_1 > 41 || I_2 > 84
65      Vdc = Vdc - 100;
66 sim('circuit_simulation');
67 I_1           = max(Ip_measured)/sqrt(2);
68 I_2           = max(Is_measured)/sqrt(2);
69 end

70
71 while I_1 < 41 && I_2 < 84
72      Vdc = Vdc + 50;
73 sim('circuit_simulation');
74 I_1           = max(Ip_measured)/sqrt(2);
75 I_2           = max(Is_measured)/sqrt(2);
76 end

77
78 while I_1 > 41 || I_2 > 84
79      Vdc = Vdc - 10;
80 sim('circuit_simulation');
81 I_1           = max(Ip_measured)/sqrt(2);
82 I_2           = max(Is_measured)/sqrt(2);
83 end

84
85 while I_1 < 41 && I_2 < 84
86      Vdc = Vdc + 5;
87 sim('circuit_simulation');
88 I_1           = max(Ip_measured)/sqrt(2);
89 I_2           = max(Is_measured)/sqrt(2);
90 end

91
92 while I_1 > 41 || I_2 > 84
93      Vdc = Vdc - 1;
94 sim('circuit_simulation');
95 I_1           = max(Ip_measured)/sqrt(2);
96 I_2           = max(Is_measured)/sqrt(2);
97 end

98
99 P(i,1) = offset_x(i);
100 P(i,2) = offset_y(i);
101 if P(i,3)< max(Power)
102 P(i,3) = max(Power);
103 end
104 P(i,4) = I_1;
```

```matlab
105     P( i , 5 )  =  I_2 ;
106     P( i , 6 )  =  ( I_2^2*R_l )/( I_1^2*(R1+R1_cap) + I_2^2*(R2+R2_cap+R_l ) ) ;
107     P( i , 7 )  =  R_l ;
108     P( i , 8 )  =  Vdc ;
109     end
110     toc
111     end
112
113
114
115     P_map_comp  =  vec2mat( P( : , 3 ) , sqrt (m) ) ;
```

Appendix C

System simulation

C.1 Track modeling by combining quikest sections

```matlab
1  clear all
2  close all
3  clc
4  load('Vx_onderdelen.mat')
5
6  Vx_start.Time = Vx_start.Time - Vx_start.Time(1);
7  Vx_midden.Time = Vx_midden.Time - Vx_midden.Time(1);
8  Vx_bocht_4.Time = Vx_bocht_4.Time - Vx_bocht_4.Time(1);
9  Vx_stop.Time = Vx_stop.Time - Vx_stop.Time(1);
10
11 Vx = Vx_start;
12
13 while Vx.Time(end) <= 15*60
14     Vx_midden.Time = Vx_midden.Time - Vx_midden.Time(1) + Vx.Time(end)
           + 0.001;
15     Vx = append(Vx,Vx_midden);
16     Vx_bocht_4.Time = Vx_bocht_4.Time - Vx_bocht_4.Time(1) + Vx.Time(
           end) + 0.001;
17     Vx = append(Vx,Vx_bocht_4);
18 end
19
20     Vx_midden.Time = Vx_midden.Time - Vx_midden.Time(1) + Vx.Time(end)
           + 0.001;
21     Vx = append(Vx,Vx_midden);
22     Vx_stop.Time = Vx_stop.Time + Vx.Time(end) + 0.001;
23     Vx = append(Vx,Vx_stop);
24
25
26 hold on
27 plot(Vx)
28 xlabel('time [s]')
29 ylabel('speed [m/s]')
30 hold off
```